CHARACTERIZATION OF TWO-PHOTON EXCITATION: COHERENT CONTROL AND NONLINEAR PROPAGATION IN TRANSAPARENT MEDIA

A Dissertation

by

MILAN PRASAD POUDEL

Submitted to the Office of Graduate Studies of
Texas A&M University
in partial fulfillment of the requirements for the degree of

DOCTOR OF PHILOSOPHY

August 2009

Major Subject: Applied Physics

CHARACTERIZATION OF TWO-PHOTON EXCITATION: COHERENT CONTROL AND NONLINEAR PROPAGATION IN TRANSAPARENT MEDIA

A Dissertation

by

MILAN PRASAD POUDEL

Submitted to the Office of Graduate Studies of
Texas A&M University
in partial fulfillment of the requirements for the degree of

DOCTOR OF PHILOSOPHY

Approved by:

Chair of Committee,	Hans A. Schuessler
Committee Members,	George Kattawar
	Winfried Teizer
	Alvin T. Yeh
Head of Department,	Edward S. Fry

August 2009

Major Subject: Applied Physics

ABSTRACT

Characterization of Two-Photon Excitation: Coherent Control and Nonlinear Propagation in Transparent Media. (August 2009)

Milan Prasad Poudel, B.S., Tribhuvan University

M.S., Diplom, University of Hannover

Chair of Advisory Committee: Dr. Hans A Schuessler

Coherent control of laser induced processes is based on the quantum interference among multiple excitation pathways. Progress in the field has been fueled by advances in pulse shaping techniques, allowing modulation of phase and amplitude across the bandwidth of ultra short pulses. This dissertation makes use of coherent control technique for the optimization of two-photon fluorescence (TPF) and its applications in selective excitation for biomedical imaging. Different physical processes, e.g. TPF, second harmonic generation (SHG) and their ratios (e.g. TPF/SHG) were optimized by using feedback control pulse shaping technique with an evolutionary algorithm. Various nonlinear effects, e.g. filamentation, intensity clamping and white light generation were studied using two-photon fluorescence and Z-scan technique with different dyes and biomarkers. Simultaneous measurements of different nonlinear effects were performed. Novel methods were proposed and implemented to obtain two-photon excitation characteristics in intensity-resolved manner. Understanding of these nonlinear effects can give new solution to the issues of spatial resolution and molecular contrast for cellular and tissue imaging.

DEDICATION

This dissertation is dedicated to my wife Pabitra and daughter Keran.

ACKNOWLEDGEMENTS

First of all, I would like to thank my advisor Dr. Hans A Schuessler for his advice, guidance and support during this research work. I would also like to thanks my committee members, Dr George Kattawar, Dr Winfried Teizer, Dr Alvin T Yeh and Dr George R Welch, for their guidance and support throughout the course of this research. I am thankful to Dr. Alexander Kolomenskii for all his help during my years here.

I would also like to thank Dr. Marcus Motzkus and Dr. Michael Sattchel from Max Planck Institute for Qantum Optics, Germany for their help in implementing the evolutionary algorithm. My thanks to Dr Gehard Paulus for letting me use some of his instruments. I would also like to thank the Dr Alvin Yeh group, biomedical engineering, TAMU, for providing me the biomarkers and other dyes used in this research work.

I would also like to express my appreciation to all of the wonderful people who have worked in this lab over the years: Dr James Strohaber, Dr Jinhai Chen, Dr Serguei Jerebtsov, Nathan Hart, Feng Zhu, Kete Perkins and Fransico Pham. It has been a pleasure to share the lab with you.

Finally, I would like to thank my family members for their continuing support during this work, especially my wife, Pabita, daughter, Keran, my parents, my brothers, Sagar and Indra, and my sisters Roja and Maiya.

TABLE OF CONTENTS

Page

CHAPTER Page

LIST OF FIGURES

FIGURE Page

FIGURE Page

FIGURE Page

FIGURE Page

LIST OF TABLES

CHAPTER I

INTRODUCTION

Since the invention of the laser in the early 60's scientists have used laser light to solve problems in virtually every scientific discipline. For example, one of the first applications was that scientists looked upon the interaction of matter with laser radiation as a way to manipulate suitable chemical reactions to a desired outcome [1]. Early work ignored a significant aspect of molecules they sought to control; molecules are quantum mechanical systems and their normal modes are described by motions that interfere. Shaped light fields can coherently control this interference and thereby control the final state of the system. This approach has been aptly named "coherent control".

Coherent quantum control refers an active intervention in a system's dynamics to maximize the probability that the system evolves toward a desired target state. For example, quantum control might be used to redirect a chemical reaction along a specific pathway. In addition to producing the desired evolution, control of quantum systems promises to provide a refined means for learning about the behavior of the system themselves.

When a control is applied to a system, the original Hamiltonian H and its associated quantum dynamics via $ih\frac{\partial|\phi(t)\rangle}{\partial t} = H|\phi(t)\rangle$ are altered. The new Hamiltonian $H'(t) = H + V(t)$ then includes the control interaction, $V(t)$, that is

---

This dissertation follows the style of Physical Review Letters.

the product of an applied optical field and the electric dipole operators, which redirects the dynamics to the new evolving system state $\left|\Psi'(t)\right\rangle$. In a coherently control experiment, one typically has a specific target for a specific operator O, but a control free system may not meet that desired objective. The goal of the control is to direct the new expectation value $\left\langle\Psi(t)\right|O\left|\Psi(t)\right\rangle$ with the control present toward the desired target [2].

Coherent quantum control technique has been used to influence the outcome of a quantum-mechanical interaction. The coherence properties of the laser field are exploited to achieve constructive interference for a predefined target wave function. The interference depends on the spectral phase distribution of the incident beam. As this phase distribution can be tuned, the outcome of the interaction can in principle be controlled. The laser pulse tailored to drive a system from an initial to the target state as a perturbation in complex cases such as biomolecules, not be exactly determined by a quantum-mechanical calculation, since usually even the Hamiltonian of the system is unknown. A practical alternative is to determine the required shape of the laser field in a feedback-controlled regulation loop which uses a signal derived from the experiment as feedback**.** The loop is repeated until the desired outcome is achieved

Adaptive femtosecond coherent control has proven to be an efficient tool for optimization of different physical processes [3-5]. In this approach active feedback is used to iteratively optimize a molecular process by shaping the phases of the femtosecond laser pulses. Since its introduction by Rabitz et al. [6], there has been a rapid growth of experimental studies with this technique for solving optimization

problems of complex systems. By now, it is widely used in different processes, including for example adaptive pulse compression in a dispersive medium [5], molecular electronic population transfer [7], higher harmonic generation [8], two-photon absorption [9], and energy conversion in light harvesting molecules [10]. Control of laser matter interaction could revolutionize biomedical applications. These methods have recently found application in nonlinear microscopy too, where shaping of the spectral phase has been used to enhance image contrast in coherent anti-stokes Raman scattering microscopy [11]. Similarly, for example coherent control could enhance methods such as two-photon imaging, which has provided higher resolution, lower background scattering, better sample penetration and reduced phototoxicity [12]

Two-photon fluorescence microscopy is a relatively novel imaging technique in biomedical fields. It relies on the quasi-simultaneous absorption of two or more photons (of either the same or different energy) by a molecule. During the absorption process, an electron of the molecule is transferred to an excited-state molecular orbital. The molecule (i.e. the fluorophore) in the excited state has a high probability to emit a photon during relaxation to the ground state. Due to radiationless relaxation in vibrational levels, the energy of the emitted photon is lower compared to the sum of the energy of the absorbed photons. High spatial resolution is made possible by the quadratic dependence on the laser intensity-the fluorescence is generated almost entirely in the laser's vocal volume. Advancement on short pulses has made easier to achieve high peak power with relatively low tissue damage from low average power dissipation.

Light matter interaction is governed by two competing processes: (i) the driving of both the amplitude and phase of the excited quantum system through the direct interaction with the applied oscillating electric field, and (ii) the loss of coherence through dephasing processes due to interaction of a system with in environment. When you excite the system with an ultra short pulse, dephasing processes are too slow to play and you access the coherent regime. In this case system excitation depends on the exact amplitude and phase of the exciting pulse thus providing a new degree of freedom for nonlinear microscopy. New contrasts can be designed depending on the exact shape of the optical pulse which can preferentially excite specific chemical species [13].

The aim of the research work is to contribute to efficient imaging of biomedical species by optimizing fluorescence after two-photon excitation of dyes used as markers in tissue and others. Two-photon microcopy has gotten more attention because it provides higher resolution and better sample penetration than the traditional techniques.

In this dissertation, we utilized coherent control techniques through pulse shaping to optimize two-photon fluorescence with the ultimate goal of using in selective excitation of fluorophore or fluorescent proteins under the influence of a broadband femtosecond laser source. Phase-modulated femtosecond pulses can selectively excite one type of probe molecule, leaving the others in their ground state [14]. Selectivity, in multi-photon excitation can be achieved by using a pulse shaper (e.g. Dazzler) which allows fast switching between appropriate pulse shapes [15]. Selective excitation allows the characterization of a molecular interaction (e.g. protein & protein) which has

significant impact in biomedical optics. For example selective two-photon excitation would be desirable for distinguishing healthy from cancerous tissue based on their chemical property.

Along with optimizing the TPF signal [16, 17] or carrying out the selective excitation, it is also important to understand how the nonlinear propagation of the ultra short pulse through the dispersive media (e.g. water) affects out results. Some of these nonlinear effects can be used to get higher contrast. Therefore, we have made a detailed study of nonlinear effects on different dyes and bio markers i.e. Coumarin-30, Texas-Red and Melanin.

By using shaped pulses and two-photon fluorescence along with a Z-scan technique [18], we have studied different kinds of nonlinear effects, i.e. self-focusing, white light continuum generation, filamentation, intensity clamping [19], saturation and optical breakdown. Furthermore, simultaneous measurements in pairs out of three processes: two-photon fluorescence, transmission and white light continuum generation were performed to better understand the interplay of these phenomena. The effect of linear chirp on a two-photon fluorescence signal during a Z-scan was also investigated. Here, it is important to note that some of these nonlinear effects (e.g self phase modulation, two-photon absorption) also named as "nonlinear signatures" have evolved as versatile solutions to the issues of spatial resolution and molecular contrast for cellular and tissue imaging [17].

To generate differently shaped pulses, different kinds of pulse shaping technique were implemented [15]. We have designed a novel modification of a 4f pulse

shaper. Instead of the traditional scheme with symmetric beam paths before and after the gratings and the spatial light modulator (SLM), we employed a scheme in folded geometry with an end mirror immediately after the modulator. This setup is intrinsically highly symmetric and can be readily aligned. By using pulse shaping techniques in combination with an evolutionary algorithm [15], we have optimized different nonlinear processes. Initially we optimized second harmonic generation to check the reliability of the algorithm and adaptive control system. Then we optimized two-photon fluorescence of organic dyes and biomarkers. Ratios between these two processes were also optimized. In addition to that, novel methods were proposed and implemented to obtain the two-photon excitation characteristics in an intensity-resolved manner [20, 21].

1.1 Organization of Dissertation

Chapter II: This chapter describes the details of femtosecond laser systems and the pulse shaping techniques used in the experiments.

Chapter III: The first part of this chapter describes the basis of the nonlinear propagation in transparent media. Various non-linear effects were studied using two-photon fluorescence and Z-scan techniques. The second part describes the limitation on two-photon characterization and methods to overcome this limitation. Several methods were proposed and implemented to obtain two-photon characteristics in an intensity-resolved manner.

Chapter IV: This chapter provides the details of the evolutionary algorithm that we have used for our coherent control system. This evolutionary algorithm was implemented in LabView programming and the performance of this algorithm was checked using a known outcome. It was later applied to optimize the real physical processes with unknown characteristics.

Chapter V: This chapter describes the details of optimization of two-photon fluorescence and the ratio between the two physical processes. At the end we have discussed the possibility of using such a coherent control optimization technique for selective excitation using broadband femtosecond laser light.

Chapter VI: This chapter gives the summary of the research work carried.

CHAPTER II

SHAPING OF FEMTOSECOND LASER PULSES

This chapter has the following structure: first the basic aspects of the femtosecond laser pulse generation and the description of the two femtosecond laser systems used in the experiments is described followed by a discussion of pulse measurement techniques. The last part of the chapter describes the pulse shaping techniques and generation of different kinds of pulses.

2.1. Mode-Locking

Mode-locking is a technique in optics by which a laser can be made to produce pulses of light of extremely short duration. In a narrow-bandwidth laser usually only one cavity mode is selected for CW operation but an ultrafast laser supports many longitudinal modes. In the free running regime all the modes oscillate inside the cavity with random phases. For pulsed laser operation the phases of all the oscillating modes need to be phase locked or mode-locked. The mode-locking will result in a periodic constructive interference of the locked modes, yielding at the output of the laser a train of short and intense laser pulses. Methods for producing mode-locking in a laser may be classified as either active or passive. Active methods typically involve using an external signal to induce a modulation of the intra-cavity light. Passive methods do not use an external signal, but rely on placing some element into the laser cavity which causes self-

modulation of the light. The widely used technique for a Ti:Sapphire laser is the Kerr-lens mode-locking [22, 23]. This is a technique of passive mode locking and is based on the nonlinear Kerr-lens effect. The Kerr effect can be described as modification of the refractive index in response to electric field. This technique is also used in our KML (Kapteyn-Murnane Labs) oscillator.

Consider an intense laser beam with Gaussian intensity profile incident on a nonlinear medium (Fig. 2.1). In a strong laser field the index of refraction of the

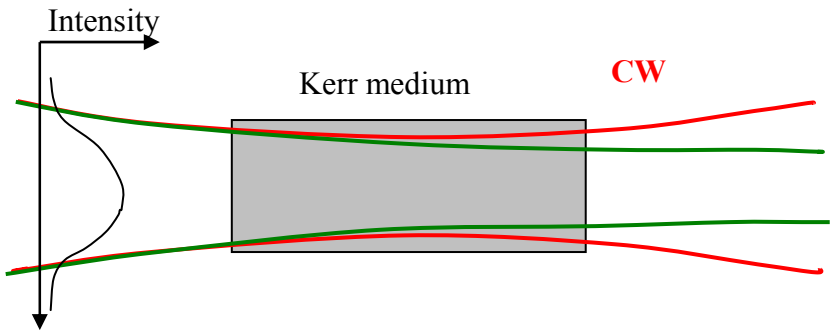

Fig. 2.1. Effect of the Kerr self-lensing on a pulsed (green), and cw (red) laser beams of the same average power propagating in a nonlinear Kerr medium. The pulsed laser light has higher intensity and correspondingly stronger self-lensing effect than in the CW beam .

medium is directly proportional to the field intensity I, and can be written in the form

$$n(r) = n_o + n_2 I(r)$$

where $n(r)$ is the overall refractive index, *no* is the linear refractive index of the material medium and n_2 is the nonlinear refractive index. For positive values of n_2 the refractive

index is the maximum at the center of the beam and gradually decreases to the edge. This change in refractive index will result in focusing of the laser beam as it propagates through the nonlinear material. When laser intensity becomes higher, the self-lensing effect becomes stronger. The focusing of the beam inside the material will continue until it is balanced by the linear diffraction. To efficiently utilize the Kerr-lensing effect, the cavity modes are focused inside the Ti:Sapphire crystal. If the cavity is optimized for the presence of the Kerr-lens, then pulsed operation of the laser will be favored over quasi-CW operation [23].

2.2 Chirped Pulse Amplification (CPA)

Increasing laser peak power and intensity has been one of the most important problems for laser science since invention of a laser. Remarkable progress in development of high power femtosecond pulses and their applications has been achieved since introduction of chirped pulse amplification (CPA) in mid 1980s.

The output of a typical Ti:Sapphire femtosecond oscillator is a train of pulses with a few hundreds mill watts with a repetition rate of about 100 MHz and a pulse energy of about several nano joules. To obtain pulses in the higher energy range, the output of the oscillator needs to be amplified. One of the main problems in producing short and high energy optical pulses is that their high intensity $\geq 10^{11}$ (W/cm^2) can easily exceed the damage threshold of Ti:Sapphire crystal, 10^{10} W/cm^2 [24, 25]. To avoid the

damage of the crystal, the peak intensity needs to be reduced. This is achieved by using the Chirped Pulse Amplification (CPA) technique.

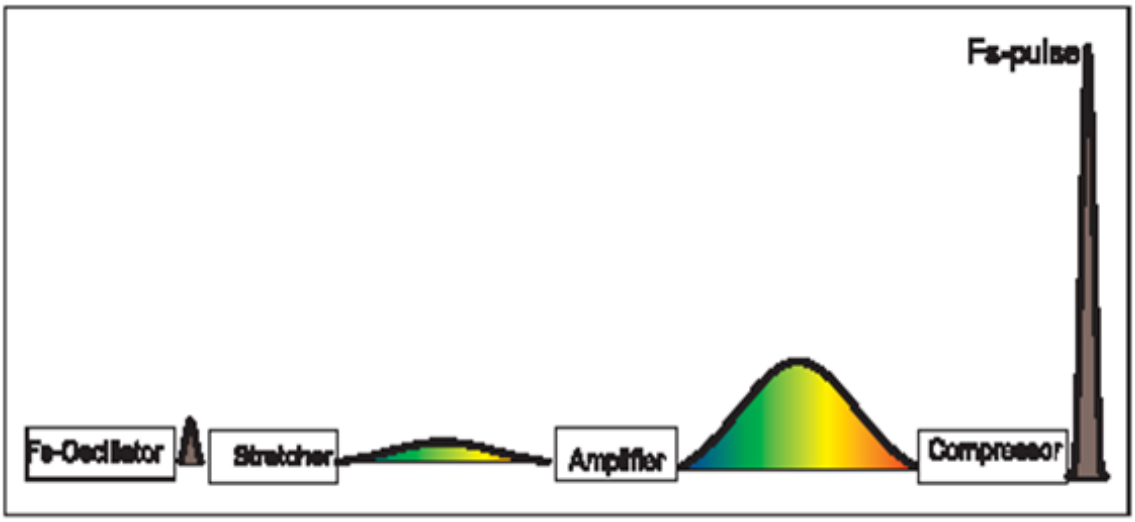

Fig. 2.2. Chirped Pulse Amplification (CPA)

The principle of this technique is illustrated in Fig. 2.2. First, the pulse from the oscillator is temporally stretched inside a stretcher by separating in time its

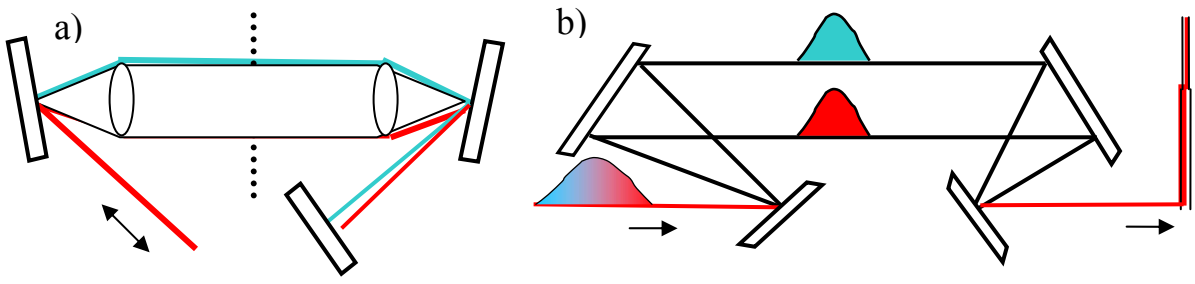

Fig. 2.3. Schematic of the (a) grating stretcher and (b) grating compressor

frequency components. Then this pulse is directed into the amplifier regenerative cavity, where it travels back and forth several times, and is amplified each time.

Finally, at the compressor, the amplified pulse is recompressed by assembling its spectral components back together in a grating or prism compressor. Such a technique allows one to produce short pulses with a high intensity.

A typical stretcher is a combination of gratings and lenses (or mirrors), arranged in such a way that it has a positive group velocity dispersion (GVD) (Fig. 2.3a). The spectral components with shorter wavelengths (blue), travel longer optical path than the spectral components with longer wavelengths (red). This results in spreading of the spectral components in time in a pre-determined manner. In a typical CPA system, the seed pulses are stretched by a factor of 10^2 -10^4. To compensate a positive GVD introduced to the laser pulse in the stretcher and the amplifier cavity, a grating compressor with a negative GVD is used. In a compressor, the spectral components with longer wavelengths travel longer optical distances than the spectral components with shorter wavelengths (Fig. 2.3b). It should be noted that the amplified pulse is always longer than the seed pulse, because in the amplifier cavity the optical pulse acquire also high order phase distortions that cannot be completely compensated by the compressor. Also during the amplification process, the spectral width of the laser pulse is reduced due to gain narrowing [24]. After the stretcher, the seed pulses are amplified by using the regenerative or multipass amplification technique. The research works performed in this dissertation uses both regenerative and multipass amplifiers.

2.3 Laser Systems

The present thesis used two different femtolaser systems. The many cycles laser system by Spectra Physics with a pulse length about 50 fs is described first followed by a few cycle laser system by Femtolasers with a pulse length of about 7 fs. We know that one optical cycle at 800 nm is about 2.5 fs. It follows than a 7 fs pulse consists less than 3 optical cycles.

2.3.1 The KML Oscillator

The source of the femtosecond pulses in our Spitfire laser system (Spectra Physics) is a Kerr-lens mode-locked Ti:Sapphire oscillator (Kapteyn-Murnane Labs). The outline of the oscillator is shown in Fig. 2.4. Ti:Sapphire crystal is used as active medium, which is cut at the Brewster angle to minimize the losses. The oscillator is pumped by 5.5 W power at a wavelength of 532 nm from the output of a diode-pumped intracavity-doubled Nd:YAG laser (Spectra Physics, Millennia). The pump beam is focused inside the crystal collinearly with the laser axis.

To achieve the Kerr-lens effect two concave mirrors are placed forming a telescope with the crystal in the focal plane. A combination of two prisms is used to compensate for the dispersion introduced in the crystal. The output of the oscillator is a train of pulses at a repetition rate of 87 MHz, pulse energy of about 5 nJ, and a pulse duration of about 35 fs and the average power is 500 mW. The central wavelength of the oscillator can be tuned in the range 780-835 nm.

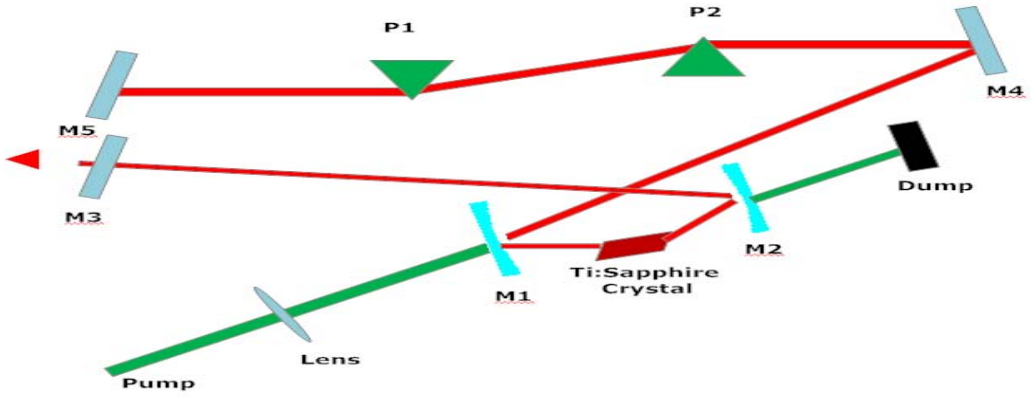

Fig. 2.4. The outline of the KML Ti:Sapphire femtosecond oscillator. M1, M2, M3, M4, M5 are the cavity mirrors, where M3 is also the output coupler. The group velocity dispersion experienced by the laser pulse traveling inside the crystal is compensated by a pair of prisms P1 and P2.

2.3.2 The CE Phase-Stabilized Ti-Sapphire Oscillator

The other Ti:sapphire oscillator (Rainbow laser from Femtolasers) used on this research work is based on prismless oscillator described in [26]. It generates pulses with a spectrum that extends from 660 to 980 nm at -10 dB below its maximum (Fig. 2.5).

Ultra-broadband chirped mirrors are used for dispersion control both inside and outside the cavity and exhibit tailored dispersion over the range of 620–1000 nm. This oscillator is pumped by 6 W Verdi laser (Coherent Inc). The average output power of the oscillator is 340 mW at 5.0 W pump power and 78 MHz repetition rate. The energy per pulse is about 4 nJ.

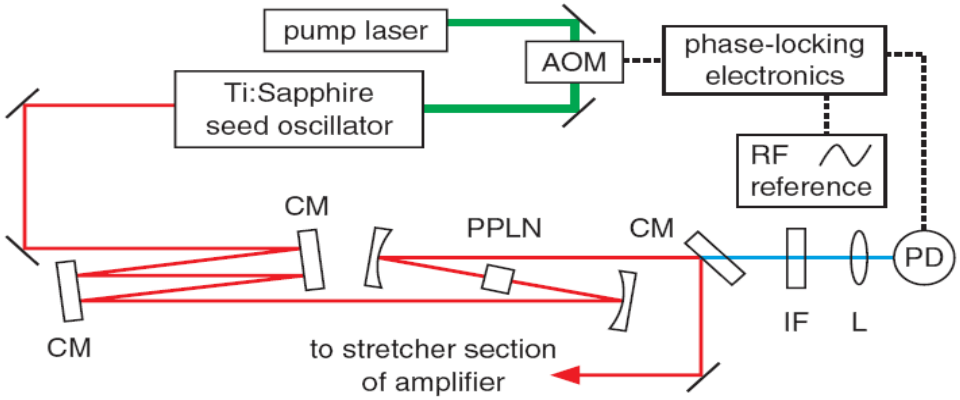

Fig. 2.5. Sketch of CEP phase stabilized laser oscillator system [26].

By tightly focusing few-cycle pulses from a the Ti:sapphire oscillator into a highly nonlinear magnesium oxide-doped periodically poled lithium niobate (PPMgO:LN) crystal, self-phase modulation (SPM) and difference-frequency generation (DFG) occur simultaneously.

In the region of spectral overlap of difference frequency generation and self phase modulation (Fig. 2.6), an interferometric beat signal can be detected. Due to the absence of walk-off effects and improved spatial overlap, the nonlinear interaction between the two waves in the crystal is enhanced, making the beat signal strong enough for reliable CE-phase locking [26].

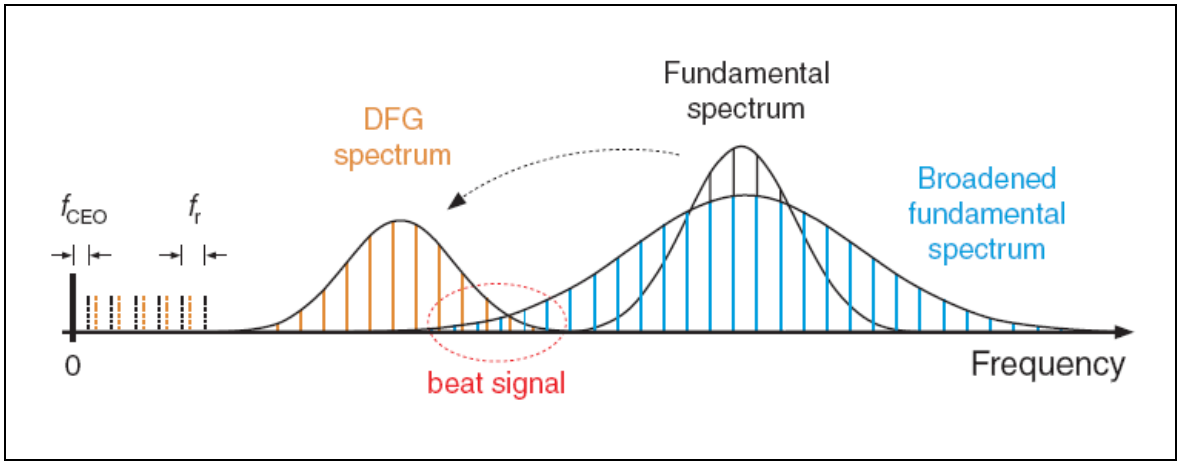

Fig. 2.6. Principle of f_{CEO} detection [26].

Fig 2.7 shows the beat signal obtained from the femtolaser Rainbow Oscillator.

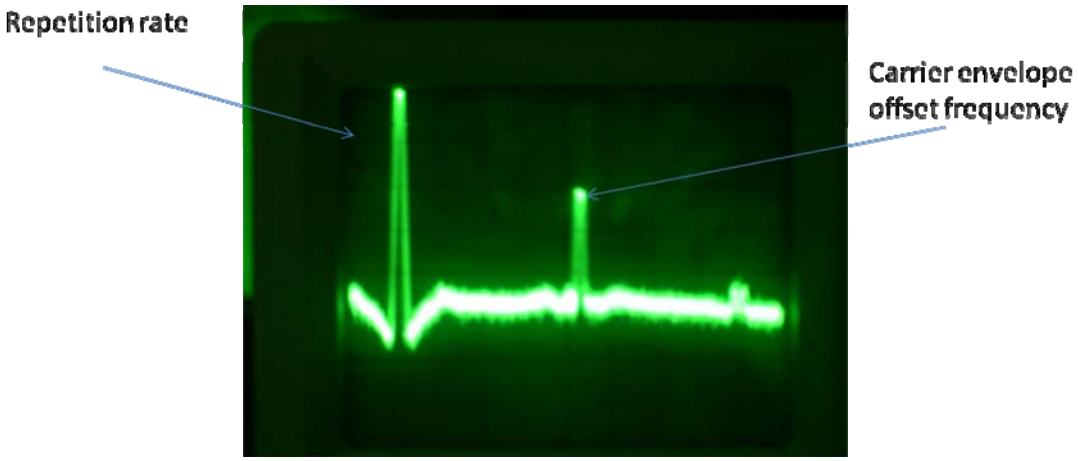

Fig. 2.7. Beat signal from the Rainbow oscillator (35 dB)

2.3.3 Regenerative Amplifier

The regenerative amplification technique is the most used technique to amplify the fs pulses. Our Spitfire amplifier (Spectra Physics) employs this technique to amplify the seed pulses. The principle of regenerative amplification is illustrated in Fig. 2.8. The repetition rate of a typical oscillator is about a 80 MHz and generate thousands of pulses. But an amplifier is pumped by a laser source with a repetition rate of several kHz, which means that only a small part of all pulses in the output train of the oscillator will be picked out and amplified. A selected seed pulse is let inside the cavity at the time when the pump pulse has just passed through the crystal. The pulse is kept inside the cavity until the gain is saturated, and after that it is let out of the cavity. For this purpose a fast optical switch with a response time in the nanosecond range is needed [24]. For linearly polarized light a combination of a Pockels cell and a broadband polarization analyzer can be used. The working principle of a Pockels cell is based on the electro-optic effect, i.e. a change of the refractive index of the material

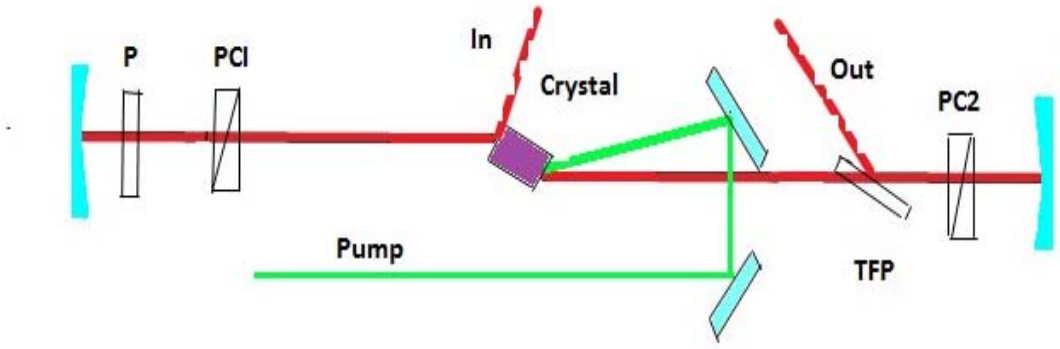

Fig. 2.8. Regenerative Cavity [23].

under application of an electric field. A birefringent crystal can act as a quarter-wave plate or as a half-wave plate, depending on the applied voltage.

Our laser amplifier system consists of three main parts: stretcher, regenerative cavity, and compressor. The seed pulses first are expanded in time in a grating stretcher. The amplifier is pumped by a Q-Switched Nd:YAG laser (Spectra-Physics, Merlin) at a repetition rate of 1kHz with output power of 10 W. A photodiode (PD) is placed behind one of the cavity mirrors so the buildup trace can be monitored on an oscilloscope. The output of the amplifier is a train of pulses with a repetition rate of 1 KHz, pulse energy 0.8 μJ, and pulse duration of 50 fs.

2.3.4 Multipass Amplifier

Our new Femtolaser amplifier uses a multipass amplification technique. In a multipass amplifier, beam passes through the gain medium multiple times without the use of the cavity. The particular geometry for accomplishing this can differ from system to system [26, 27]. In a multipass amplifier, since the optical path is not a resonator, the amplified stimulated emission can be suppressed to a greater degree than in a regenerative amplifier.

The sketch of our multipass amplifier is shown in Fig. 2.9. After the oscillator a Dazzler acousto-optical filter (Fastlite) was used to condition the spectrum of the seed pulse. Then the seed beam passes through the multipass amplifier. In the first two paths it is amplified by about 70 times and after the fourth pass the amplification is

around 5000 times. After the fourth pass, a single pulse is selected using Pockel's cell and a rotatable quarter wave plate. Consequently, the pulse is amplified again during the pass from five to nine and then it goes though a prism compressor. After the

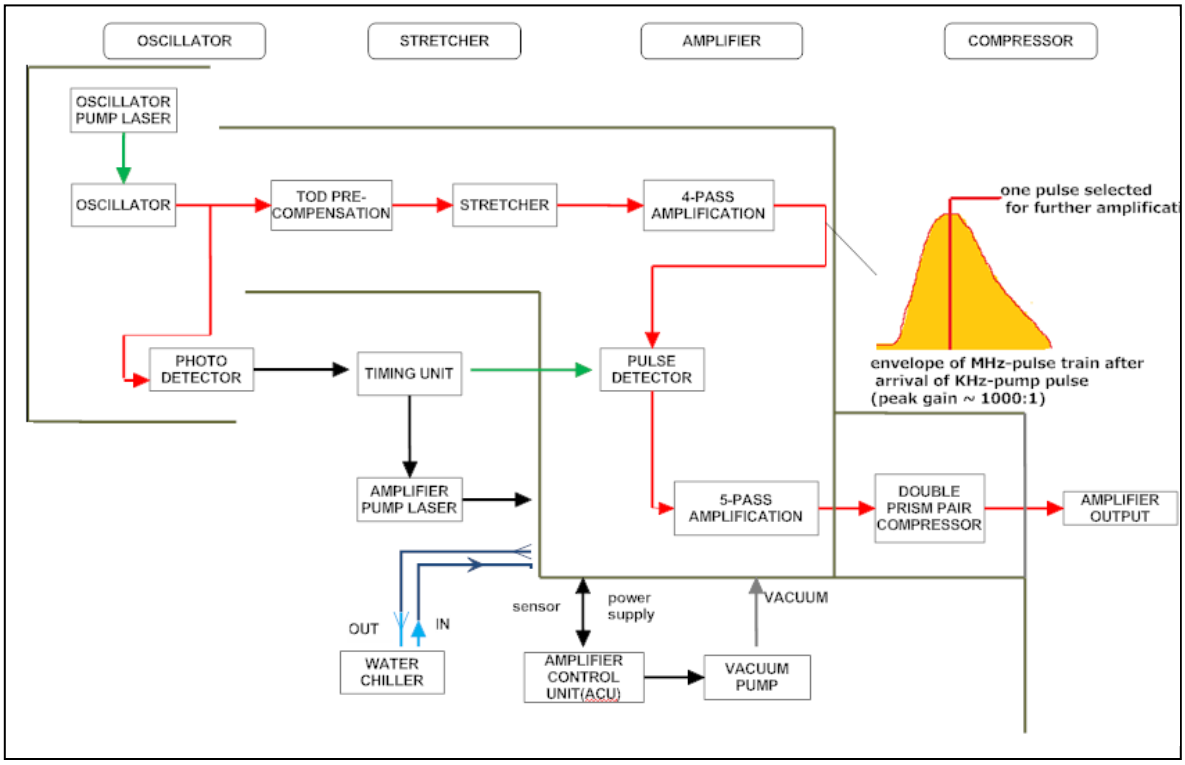

Fig. 2.9. Sketch of a CEP phase stabilized Femtolaser multipass amplifier .

compressor, the output pulse has a duration around 30 fs and an output average power is about 4.5 W with energy per pulse is 1 mJ.

An f-2f interferometer set up with a feedback controlling loop was used to stabilize the CEP phase [27]. Fig. 2.10 shows the carrier-envelope phase when the stabilization system is "on" (phase locked)

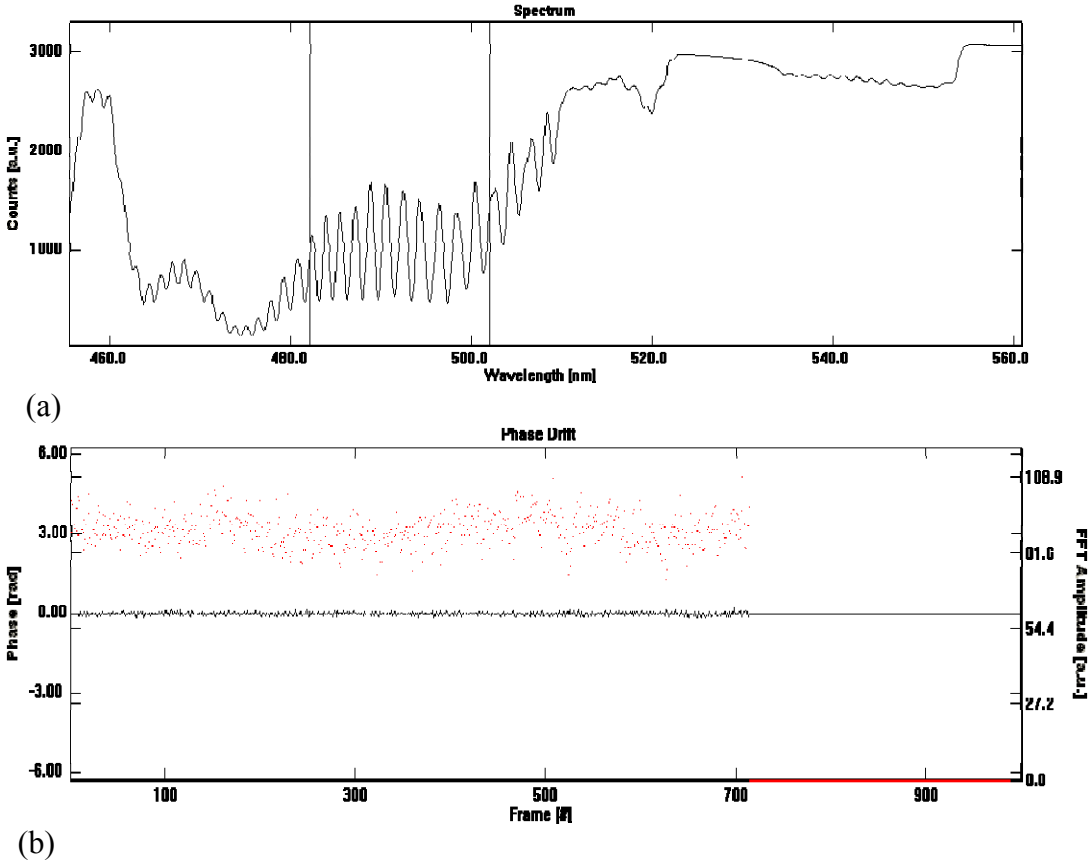

Fig. 2.10 Carrier Envelope Phase (CEP) stabilization when CEP phase stabilization system is "on". (a) Interferometric signal , (b) stabilized absolute phase

To get even shorter pulses, the pulses from the amplifier of 30 fs duration were sent through a hollow fiber using a one meter focal length lens. The hollow fiber was placed inside the neon gas chamber. The output power from the fiber is about 2 W and the pulse duration after compression with a set of chirped mirrors is about 7 fs.

2.4 Pulse Measurements

2.4.1 Auto-Correlation

The most broadly used technique for measuring femtosecond laser pulses is the second-order autocorrelation method, which was first demonstrated in 1966 by Maier and co-workers [28]. This method takes advantage of the second harmonic generation in nonlinear crystals.

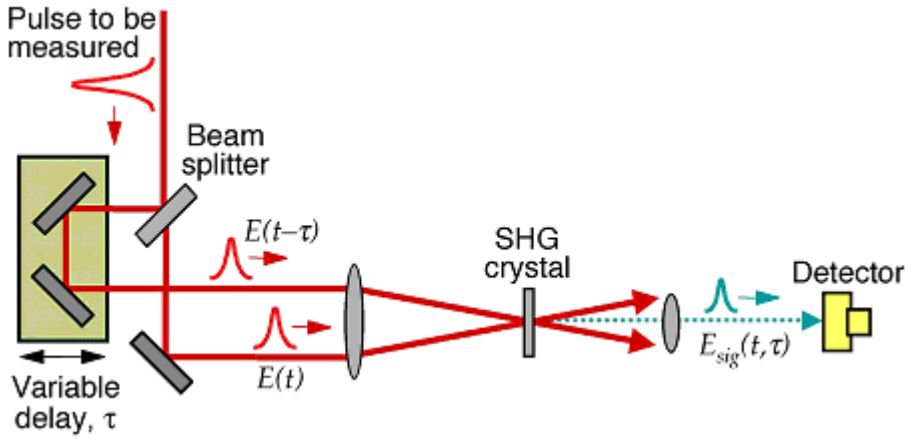

Fig. 2.11. Autocorrelation set-up of an intensity autocorrelator with second harmonic generation [29]

In Fig. 2.11 the basic principle of a SHG autocorrelation method is displayed. The incident laser pulse is split into two by using a 50/50 beam-splitter. As in a Michelson interferometer, the two pulses are reflected in each arm and subsequently focused onto a frequency-doubling crystal (BBO). The resulting auto-correlation trace is

detected by a photo-multiplier as a function of the time delay between the two pulses. The SHG crystals can be type I or type II phase matching, and the two pulses can recombine collinearly or non-collinearly in the frequency doubling crystal.

If the two fields are of intensity I(t-τ) and I(t), the auto-correlation function $A_{ac}(\tau)$ of the two pulses can be written as

$$A_{ac}(\tau) = \int I(t)I(t-\tau)dt \tag{2.1}$$

The auto-correlation function is always symmetric in time. But, it gives very little information about the shape of the pulse, since an intensity of symmetric and asymmetric pulse shapes can have similar auto-correlation functions. The most widely used procedure to determine the pulse duration is to "assume" a pulse shape (usually

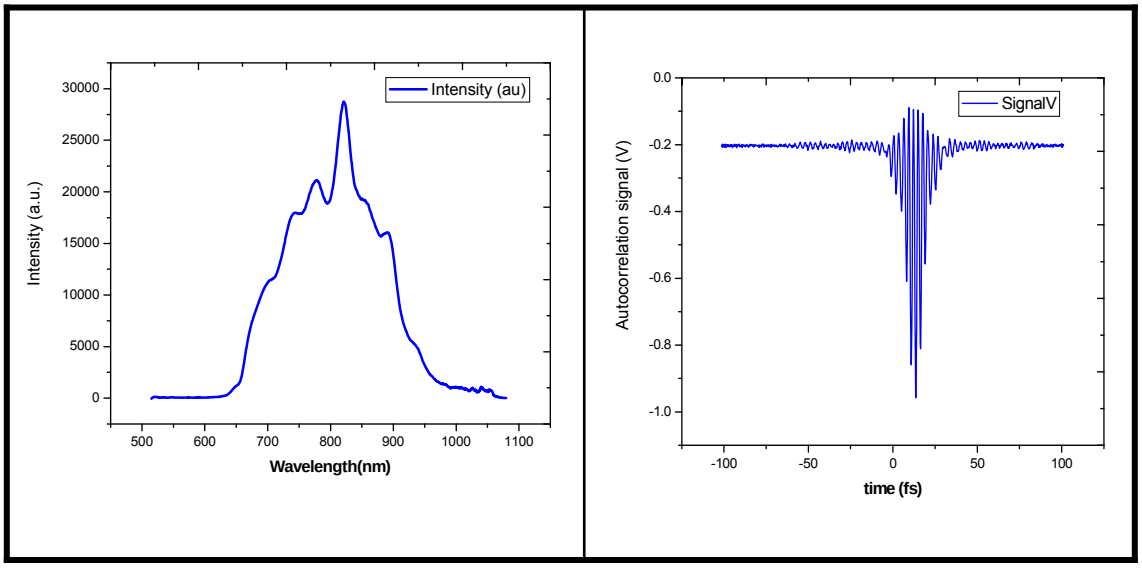

Fig. 2.12 Measured autocorrelation trace from rainbow oscillator (a) spectrum (b) autocorrelation trace (inverted).

$sech^2$ or a Gaussian shape, for chirp-free and linear chirped pulses) and to calculate the pulse duration from the known ratio between the FWHM of the auto-correlation and of the pulse [23]. Thus the auto-correlation function depends on the assumed shape of the pulse. Fig. 2.12 shows the autocorrelation measurement of rainbow oscillator from femtolaser autocorrelator. The measured pulse duration is 6.5 fs.

2.4.2 Frequency Resolved Optical Gating (FROG)/ GRENOUILLE

Frequency resolved optical gating (FROG) is a technique that characterizes pulses in the temporal domain. Since its introduction about a decade ago, FROG has evolved as a powerful technique for measuring femtosecond laser pulses [29, 30]**.** The

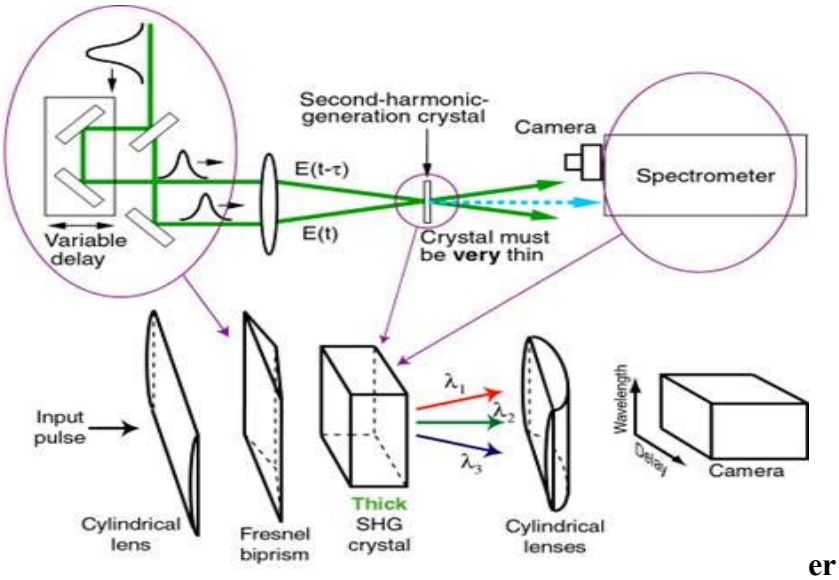

er

Fig. 2.13. GRENOUILLE, a kind of second harmonic generation FROG [30]

FROG set up is just an auto-correlation set up plus a spectrometer, which can char acterize the shape and phase of the pulse. Recently, FROG device was modified by Trebino et al. by replacing the beam splitter, delay line, and beam combining optics with a Fresnel biprism and a thick crystal that plays the role of a spectrometer. Such a device was called GRENOUILLE, and it uses two cylindrical lenses as shown in Fig. 2.13. The first cylindrical lens must focus the beam into the thick crystal tightly enough to yield a range of crystal incidence (and hence exit) angles large enough to include the entire spectrum of the pulse. After the crystal, a cylindrical lens then maps the crystal exit angle onto position at the CCD camera, with wavelength a near-linear function of (vertical) position.

2.5 Pulse Shaping

2.5.1 Shaped Femtosecond Laser Pulses

The available electronics today is too slow for the modulation of a laser pulse in the femtosecond time domain. Thus, for shaping femtosecond pulses it is required to modulate the amplitude and the phase of the laser radiation in the frequency domain. The frequency and time representation of a femtosecond laser pulse can be related by the Fourier transform. Now, the complex spectral amplitude $E(\omega)$ can be written by using Fourier transform [8, 23].

$$E(\omega) = \int_{-\infty}^{+\infty} E(t) e^{-i\omega t} dt \tag{2.2}$$

where $E(t)$ is the electric field in the time domain which can be written by using the inverse Fourier transform as

$$E(t) = \int_{-\infty}^{+\infty} E(\omega) e^{-i\omega t} d\omega \tag{2.3}$$

The complex quantity $E(\omega)$ has nonzero values for both positive and negative frequencies.

2.5.2 Phase Modulation in the Temporal Domain

In temporal domain the electric field $E^{+}(t)$ can be separated in

$$E^{+}(t) = A(t) e^{-i\Theta(t)} \tag{2.4}$$

where $A(t)$ is the temporal amplitude and $\Theta(t)$ is the temporal phase factor. For few optical cycle pulses, phase factor $\Theta(t)$ can be written as a function of phase $\varphi(t)$ and central frequency ω_0,

$$E(t) = A(t) e^{-i\varphi(t)} e^{i\omega_o t} \tag{2.5}$$

The time derivative of the phase factor $\Theta(t)$ gives the instantaneous frequency as a function of time

$$\frac{d\Theta(t)}{dt} = \omega(t) = \omega_0 - \frac{d\varphi(t)}{dt} \tag{2.6}$$

Developing the phase $\varphi(t)$ around t_0 in Taylor series gives a closer look at the chirp in time domain

$$\varphi(t) = \varphi(t_0) + \left.\frac{d\varphi(t)}{dt}\right|_{t_0} (t - t_0) + \frac{1}{2}\left.\frac{d^2\varphi(t)}{dt^2}\right|_{t_0} (t - t_0)^2 + ... \qquad (2.7)$$

where $\varphi(t)$ represents the constant phase of the electric field which determines the relative position of the fast oscillations of the electric field with respect to the pulse envelope. The linear variation of the phase in time $\varphi(t)$ is described by the term $\left.\frac{d\varphi(t)}{dt}\right|_{t_0}$, which gives the shift of the carrier frequency ω_0. For a transform-limited pulse the temporal phase depends linearly with time: $\varphi(t) = \varphi(t_0) + \left.\frac{d\varphi(t)}{dt}\right|_{t_0}$. The quadratic term $\left.\frac{d^2\varphi(t)}{dt^2}\right|_{t_0}$ gives the linear chirp, i.e. the linear variation of the instantaneous frequency with time. For $\left.\frac{d^3\varphi(t)}{dt^3}\right|_{t_0}$ and higher orders, the terms give the quadratic and higher order chirps.

An example of nonlinear phase modulation in temporal domain of an unchirped femtosecond pulse is the self-phase modulation (SPM).

2.5.3 Phase Modulation in the Spectral Domain

The most common example of a spectral phase modulation is the dispersion in a transparent material (e.g. optical glass), which has a time independent refractive index $n(\omega)$. This phenomenon does not change the pulse spectrum. The phase term

$$\Psi(\omega) = \frac{2\pi}{\lambda_0} n(\omega) l \tag{2.8}$$

is responsible for modulation of the electric field $E^+(t)$ where l is the thickness of the optical medium. After propagating through such a medium, the frequency components within the pulse will disperse and travel with different time delays towards each other. This phenomenon is called Group Velocity Dispersion (GVD).

Hence it is of an advantage to Fourier transform the pulse in the frequency domain, to calculate the phase for each of its frequency components and then to perform an inverse Fourier transform back in the time domain. The Taylor expansion of $\Psi(\omega)$ around the central frequency ω_0 is written as follows

$$\Psi(\omega) = \Psi(\omega_0) + \left.\frac{d\Psi(\omega)}{d\omega}\right|_{\omega_0} (\omega - \omega_0) + \frac{1}{2}\left.\frac{d^2\Psi(\omega)}{d\omega^2}\right|_{\omega_0} (\omega - \omega_0)^2 + \ldots \tag{2.9}$$

The first term is a constant and determines the relative temporal phase of the pulse. The change of the linear coefficient $\left.\frac{d\Psi(\omega)}{d\omega}\right|_{\omega_0}$ results (after a Fourier transform) in a temporal domain in a shift on the time axis and gives the pulse time delay. The coefficient

$\left.\frac{d^2\Psi(\omega)}{d\omega^2}\right|_{\omega_0}$ gives the linear spectral chirp. In general, a spectral chirp of $(n-1)^{th}$ order is given by $\left.\frac{d^n\Psi(\omega)}{d\omega^n}\right|_{\omega_0}$.

Since shaping of the femtosecond pulses with a liquid crystal modulator takes place in the frequency domain, a short introduction is given in the next paragraph.

$$E_{in}(\omega) = S(\omega)e^{-i\varphi(\omega)} \tag{2.10}$$

where $S(\omega) = \frac{1}{\sqrt{2\pi}}\sqrt{I(\omega)}$ is calculated from the measured spectrum $I(\omega)$. The notation $E_{in}(\omega)$ was used because the input laser pulse is to be shaped after passing through the modulation filter. The modulation filter is described by the complex function

$$H(\omega) = A(\omega)e^{-i\Psi(\omega)} \tag{2.11}$$

where $A(\omega)$ represents the amplitude filter. The phase factor $\Psi(\omega)$ is responsible for the phase delay of every frequency component, and it has the form like in equation (2.10). After passing through the modulating optical element, the output electric field has the form [23, 31]

$$E^+_{out}(\omega) = H(\omega)E^+_{in}(\omega) = A(\omega)e^{-i\Psi(\omega)}E^+_{in}(\omega) \tag{2.12}$$

By inserting equation (2.9) in (2.12) and performing a Fourier transform one can obtain the shape of the output electric field after passing through the modulator.

2.5.4 Pulse Shaper

2.5.4.1 Liquid Crystal -Spatial Light Modulator (LC- SLM)

Because of their anisotropic nature, liquid crystals can be arranged to serve as wave retarders or polarization rotators. In the presence of an electric field, the molecular orientation is modified, so that its effect on a polarized light is altered.

The liquid crystal spatial light modulator (SLM-640, Jenoptik) that we used has 640 pixels with active area of 63.7 mm x 7 mm separated by gaps with width of 0.12 mm. The nematic liquid crystal is driven by a 0-8 V RMS voltage with frequency 4 KHz. The transmission for wavelength range (430nm-800nm) is >75%. The maximum phase shift at 430 nm is 7π and at 1500 nm is 2π. The damage threshold as given by the datasheet is 300GW/cm^2 at 800nm, 45 fs and repetition rate of 1 kHz.

The LC SLM is controlled by a controller board which can be connected to a PC via the RS 232 interface. The modulator can be controlled by simple terminal program including LabView or other programming language with RS-232 functions.

The retardation of LC-SLM was measured with a simple set up. A He-Ne laser was used as a light source. Two linear polarizing plates were set up with the transmission axis perpendicular to each other with an angle of 45 deg. to the vertical axis of the liquid crystal spatial light modulator array. Two lenses are used to focus the beam

into one stripe. This is necessary to get the phase retardation of only one stripe of the LC cell.

The light emerging from the array was focused onto a standard photo diode .The transmission was recorded in dependence of the pixel voltage (0-8) V in 4096 steps. The transmission curve is shown in Fig. 2.14.

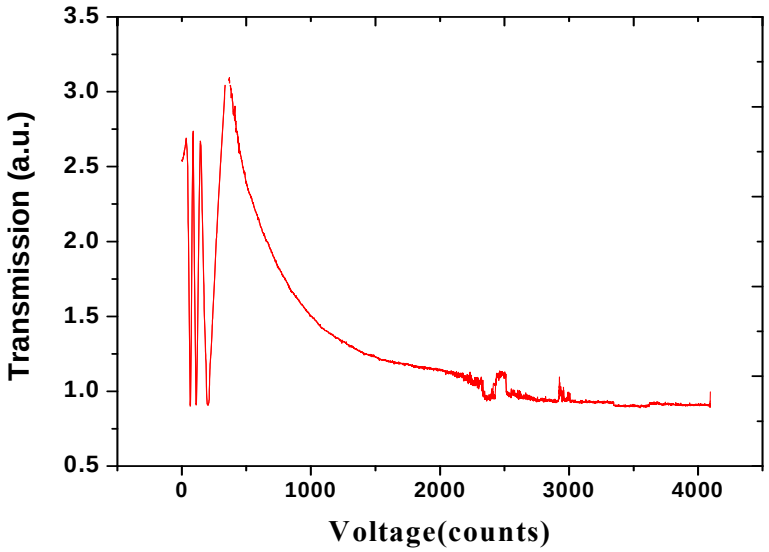

Fig. 2.14. Measured transmission signal with crossed polarizer. Spikes seen are from the noise.

The dependence for the reconstruction of the retardation from the measured transmission function is given by

$$\Gamma(U) = 2\sin^{-1}\left(\frac{T}{U}\right) \tag{2.13}$$

where U is a function of the voltage and T is the Transmission.

To account for the π periodicity the retardation function, $\Gamma(U)$ has to be unwrapped by adding multiples of π. Fig. 2.15. shows the typical characteristic of the phase modulation of the SLM-640.

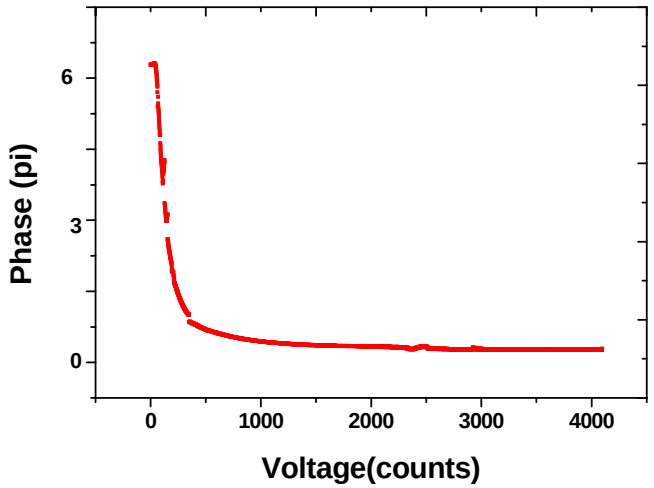

Fig. 2.15. Typical measured phase modulation dependence.

2.5.4.2 4f-Setup

The standard 4f-setup utilized for linear pulse shaping originated from the "zero dispersion compressor" setup [9]. It dissolves a broadband input pulse and separates the frequency components in a Fourier plane which lies in between two gratings and two lenses that are arranged symmetrically with distances of exactly the

focal length f of the lenses. Within this Fourier plane, a femtosecond laser pulse can be manipulated in various ways and by various devices, for example static phase masks or acousto-optical modulators [23].

We have designed a novel modification of pulse a shaper. Instead of the traditional scheme with symmetric beam paths before and after the gratings and the modulator, we employed a scheme in folded geometry with an end mirror immediately after the spatial light modulator (SLM) as shown in Fig. 2.16. This setup is intrinsically highly symmetric and can be readily aligned.

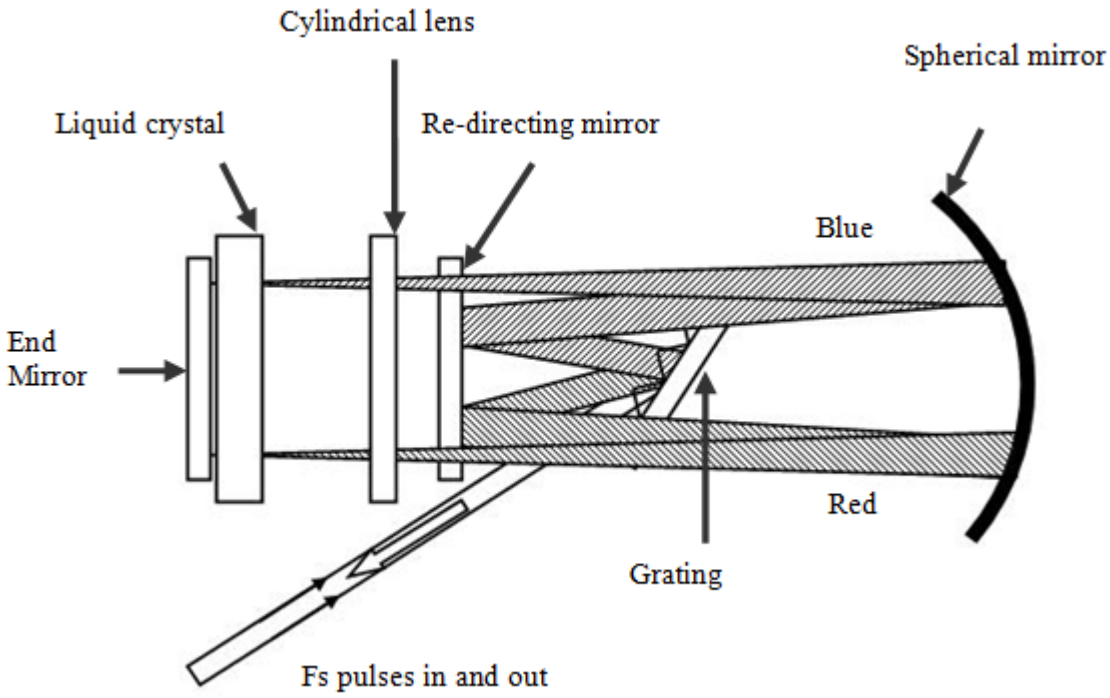

Fig. 2.16. Schematic diagram of folded 4f set-up (3-D arrangement seen from above).

An additional advantage is that it produces twice the phase shift of an unfolded set-up due to double passage through the modulator. A 1200 grooves/mm grating and a cylindrical lens with a focal length of 100 mm were used for spectrally dispersing (input) and re-collimating (output) of the laser pulses. A laser pulse with a spatially dispersed spectrum passed the liquid crystal (LC) matrix with 640 pixels in the spatial light modulator (SLM-640, JenOptik). The control of the laser pulse shape was achieved by applying a specific voltage to each pixel of the LC matrix and, in this way modulating the phases of the spectral components. After reflection on the end mirror, the pulse was re-assembled by propagating back, and its output direction was slightly shifted relative to the input pulse.

2.5.4.3 Acousto Optical Programmable Filter [Dazzler]

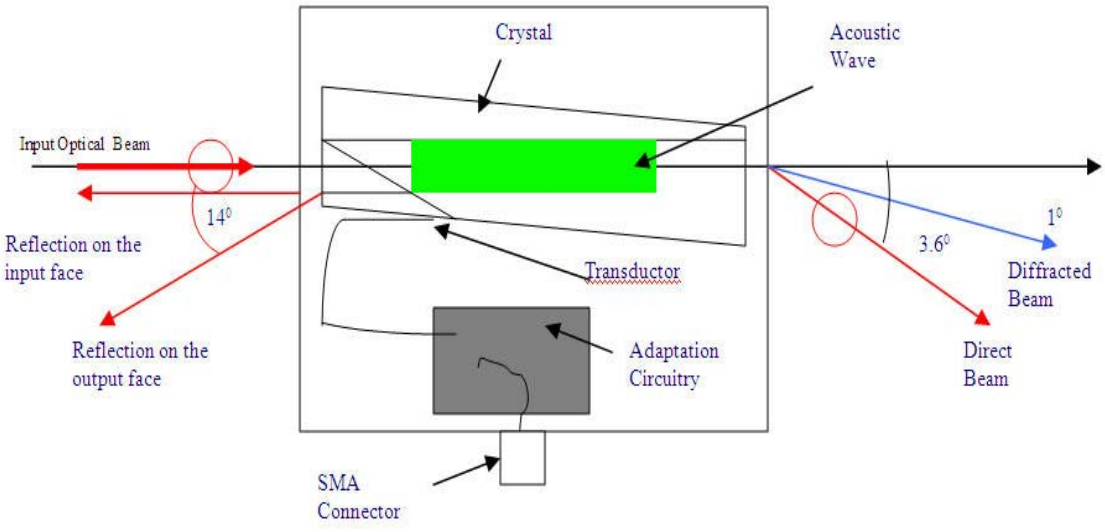

Fig 2.17 Dazzler (top view), laser pulse propagation from left to right [32]

Dazzler is an acousto-optic programmable filter. This system allows programming the shapes of ultrafast laser pulses by changing the spectral amplitudes and phases, providing delays of a few picoseconds. Fig 2.17 shows the sketch of the Dazzler.

The heart of the system is an acousto-optic programmable dispersive filter (AOPDF), which performs a convolution between the amplitude of the input optical signal $E_{int}(t)$ and a programmable acoustic signal $S\left(\frac{t}{\alpha}\right)$, proportional to the electric signal $S(t)$, applied to the piezoelectric transducer of the device.

$$E_{out}(t) = E_{in}(t) \times S\left(\frac{t}{\alpha}\right) \tag{2.14}$$

In the frequency domain, this convolution relation can be written

$$E_{out}(\omega) = E_{in}(\omega) S(\alpha\omega) \tag{2.15}$$

α being a scalar factor equal to the ratio of the speed of light c times the index difference Δn between the ordinary and extraordinary waves taken on the propagation axis chosen in the crystal. This method works without the zero dispersion stretcher and hence without spatio-temporal pulse distortions.

The extra phase delay seen by each wavelength depends on how far into the crystal the acoustic wave takes on that wavelength and the ordinary and extraordinary refractive indices. The crystal works as a set of acoustic gratings.

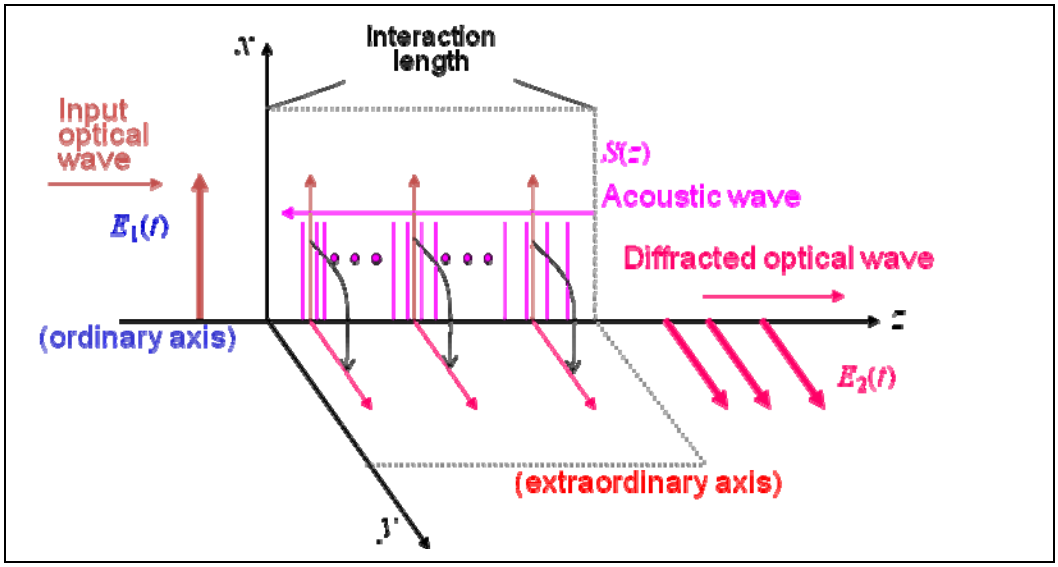

Fig. 2.18. Dazzler:-Interaction of optical wave with acoustic signal [32].

The strength of the acoustic wave at each wavelength determines the amplitude of the output wave at that wavelength. Fig 2.18 shows how optical wave interact with acoustic wave on Dazzler setup.

2.6 Properties of Laser Pulses Propagating in a Dispersive Medium

When a short pulse travels through a dispersive medium, the frequency components are experiencing various time delays. When a Gaussian laser pulse travels through a dense dispersive medium the center of the pulse is typically delayed more compared to a pulse travelling in the air. This is usually called group delay. Secondly,

dispersive media (like glass or water) impose a positive frequency sweep or "chirp" on the pulse meaning that blue components are delayed with respect to the red.

Consider an optical pulse with carrier frequency ω_0 and a complex Gaussian envelope can be written [33]

$$E(t) = \exp(-at^2)\exp\, j(\omega_0 t + bt^2) \tag{2.16}$$

The instantaneous intensity $I(t)$ associated with the pulse is

$$I(t) = \left|E(t)\right|^2 = \exp(-2at^2) = \exp[-(4\ln 2)(\frac{t}{\tau_p})^2] \tag{2.17}$$

where τ_p is the pulse width and related to a by

$$\tau_p = \sqrt{\frac{2\ln 2}{a}} \tag{2.18}$$

Now if we consider an initially unchirped pulse with $b_0 = 0$. Its Gaussian pulse parameter after propagating a distance l_m through a dispersive medium becomes

$$a(l) = \frac{a_0}{1 + (2\varphi" l_m)^2 a_0{}^2} \tag{2.19}$$

Now

$$\tau_p{}^2(l_m) = \frac{2\ln 2}{a(z)} = \tau_{p0}{}^2 + \left(\frac{(4\ln 2)\varphi" l_m}{\tau_{p0}{}^2}\right) \tag{2.20}$$

The group delay dispersion (φ") due to material length (l_m) is related to the refractive index of the material, n(λ) at the central wavelength, λ_o through its second derivative with respect to wavelength.

$$\varphi_m'' = \frac{\lambda_0^3 l_m}{2\pi c^2} \frac{d^2 n(\lambda)}{d\lambda^2} \tag{2.21}$$

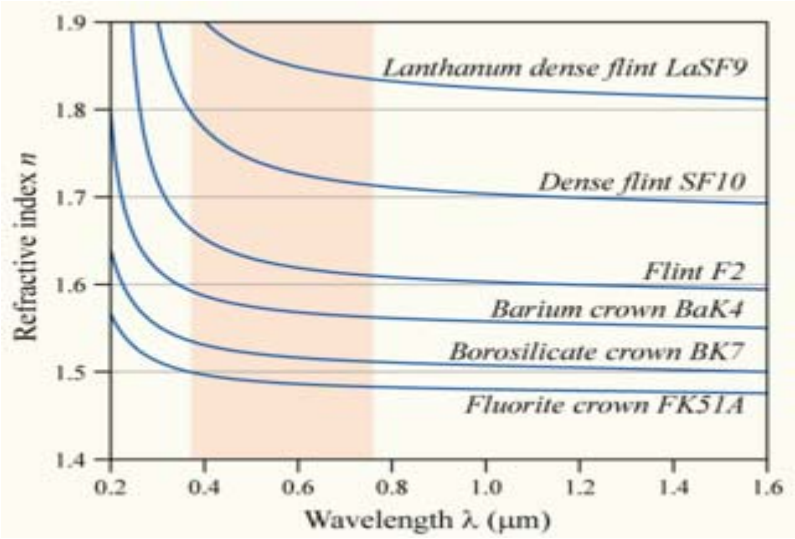

Fig 2.19 Refractive index versus wavelength data for some common glasses [34].

Fig 2.19 shows the plot between refractive index versus wavelength for different kinds of glasses. These data are fitted to Sellmeier's equations, which are then used to take the numerical derivatives for use in subsequent calculations.

CHAPTER III

TWO-PHOTON FLUORESCENCE and NONLINEAR PROPERTIES OF THE EXCITATION AND PROPAGATION OF OPTICA PULSES

The interaction of femtosecond laser pulses with transparent materials attracted recently considerable interest because of its importance in different areas of physics, biology and medicine [35-37]. At high laser intensity several nonlinear effects can develop such as self-phase modulation[35], self-focusing [36], filamentation [37] and continuum generation [38-41]. In this research work, the two-photon fluorescence (TPF) technique [42, 43] was applied to visualize these nonlinear effects.

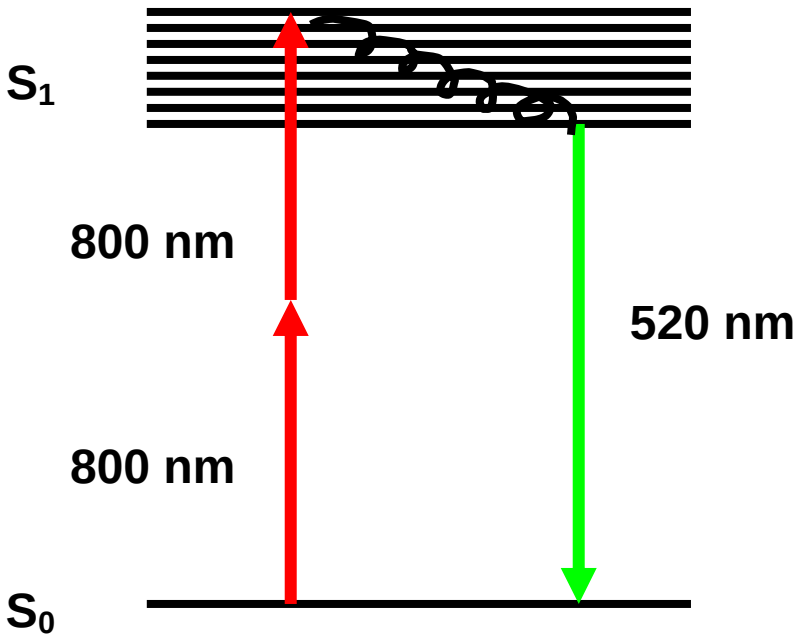

Fig. 3.1. Two-photon fluorescence = single fluorescence after two-photon excitation

It is pointed out that the term two-photon fluorescence is used for shortness employed through out this dissertation. It means that actually single photon fluorescence after two-photon excitation. The process is schematically depicted as shown in Fig. 3.1.

We have performed a systematic study of the power and intensity dependences of the two-photon fluorescence of methanol solutions of Coumarin-30 and other dyes under action of 50 femtosecond laser pulses, using Z-scan technique [18]. Various competing nonlinear processes, including self-focusing, ionization, self-phase modulation, continuum generation and the saturation effect were studied. Filamentation and intensity clamping effects were visible to the eye, when observing the two-photon fluorescence. Simultaneous measurements in pairs out of three processes: two-photon fluorescence, transmission and white light continuum generation were performed to better understand the interplay of these phenomena. The effect of a linear chirp on the two-photon fluorescence signal during a Z-scan was also investigated.

The second part of the chapter describes the different methods of finding the two-photon probability and saturation intensity.

3.1 Nonlinear Optical Propagation

This chapter describes the source of nonlinear polarization and effects associated with this type of propagation for e.g. self-phase modulation, continuum generation etc.

3.1.1 Nonlinear Refractive Index

The wave equation for the electric field of the electromagnetic wave is given by [23, 44]

$$\nabla \times \nabla \times E + \frac{\partial^2}{c^2 \partial t^2} E = -\frac{\partial^2}{\varepsilon_o c^2 \partial t^2} P \tag{3.1}$$

where E is the electric field, P is the polarization, c is the speed of the light in vacuum, ε_o is the permittivity of free space. In linear propagation, when laser intensity is low the polarization can be defined as

$$P = \in_o \chi^{(1)} E \tag{3.2}$$

where P is the polarization and $\chi^{(1)}$ is the linear susceptibility. The susceptibility is a scalar quantity for an isotropic medium so the equation (3.1) can be written as

$$\nabla^2 E + \frac{{n_0}^2 \partial^2}{c^2 \partial t^2} E = 0 \tag{3.3}$$

where n_0 is the refractive index and is given by

$$n_0 = \sqrt{1 + \chi^{(1)}} \tag{3.4}$$

When the laser intensity is high, the linear propagation in equation (3.2) is no longer valid. The nonlinear dependence of the polarization on the applied electric field can be expressed as

$$P = \in_0 [\chi^{(1)} E + \chi^{(2)} E^2 + \chi^{(3)} E^3 + ...] \tag{3.5}$$

$$= [P^{(1)} + P^{(2)} + P^{(3)} + ...] \tag{3.6}$$

where χ^n is the n^{th} order nonlinear susceptibility and $P^{(n)}$ is the n^{th} order nonlinear polarization. For example, for the second order polarization, we could have two driving fields, E_1 at frequency ω_1 and E_2 at frequency ω_2. If the medium is isotropic then the nonlinear polarization can be described by the several of these ways.

$$P^{(1)}(2\omega_1) \sim \chi^{(2)} E_1^{\,2} \tag{3.7}$$

$$P^{(2)}(2\omega_2) \sim \chi^{(2)} E_2^{\,2} \tag{3.8}$$

$$P^{(2)}(2\omega_1 + \omega_2) \sim 2\chi^{(2)} E_1 E_2 \tag{3.9}$$

The first two terms describe the second harmonic generation and the third term describes sum frequency generation. For moderate laser intensities in centro-symmetric media we may terminate expansion after the third order non-linear polarization. When the material is isotropic, P and E are parallel and therefore represented by scalars and the refractive index depends on frequency. The third order nonlinear polarization is given by [44]

$$P = \in_0 [\chi^{(1)} + \frac{3\chi^{(3)} \mid E \mid^2}{4}]E \tag{3.10}$$

$$n = \sqrt{1 + \chi^{(1)} + \frac{3}{4}\chi^{(3)} \mid E \mid^2} \tag{3.11}$$

If we take the nonlinear term to be small compared to the linear susceptibility and expressing the electric field strength in terms of the laser intensity I then, we have

$$n = n_0 + n_2 I \tag{3.12}$$

where the laser intensity I can be written as

$$I = \frac{1}{2} \in_0 cn_0 \mid E \mid^2 \tag{3.13}$$

and nonlinear refractive index, n_2 can be expressed as

$$n_2 = \frac{3\chi^3}{4 \in_0 cn_0{}^2} \tag{3.14}$$

This effect is known as the optical Kerr effect. It is self-induced effect in which the phase velocity of the wave depends on the wave's own intensity.

3.1.2 Self-phase Modulation

Self-phase modulation is the change in phase of an optical pulse due to the nonlinearity of the refractive index of the material medium. As a result of the optical Kerr effect an optical wave traveling in a third order nonlinear medium undergoes self-phase modulation.

In self-phase modulation the temporal dependence of the intensity profile leads to a temporal dependence in the refractive index which in turn produces a time dependent phase shift of the pulse. The propagation of the ultrafast pulses in a nonlinear medium is given by

$$E(t,x) = E_0 e^{(i\omega_0 t - kx)} \tag{3.15}$$

where k is given by

$$k = \frac{\omega_0}{c} n(t) \tag{3.16}$$

The instantaneous frequency $\omega(t)$ is given by

$$\omega(t) = \frac{\partial \phi(t)}{(\partial(t))} = \omega_0 - \frac{\omega_0}{c} \frac{\partial n(t)}{\partial t} x \tag{3.17}$$

and the frequency variation as

$$\Delta\omega(t) = \omega(t) - \omega_0 = \frac{-\omega_0 n_2}{2c} x \frac{\partial I(t)}{\partial t} \tag{3.18}$$

In the self- phase modulation process, when the nonlinear refractive n_2 is positive, new low frequencies are created in the leading edge of the pulse envelope and new high frequencies are created in the trailing edge.

3.1.3 Self-focusing

Self-focusing results from wave-front distortion inflicted on the beam by nonlinear polarization while propagating through a nonlinear medium. It is the spatial analogue of self-phase modulation. Although the refractive index variation depends on the laser intensity, the strength of the self-focusing depends mainly on the peak power of the laser pulse. Besides that temporal dispersion and self-phase modulation can interact strongly with self-phase modulation**.** An especially interesting case occurs when the self-focusing action and the diffraction action on the input beam balance each other. The beam should propagate in the medium over a long distance without any change in its beam diameter. This effect is known as self-trapping. In practice, however, self-trapping power losses due to absorption or scattering can upset the balance between self-focusing and diffraction that cause the beam to diffract [39].

The early theory based on the paraxial wave equation predicts the catastrophic collapse of self focusing beam in Kerr media [45]. Feit and Fleck [46] pointed out this unphysical collapse is due to invalidity of the paraxial wave equation in the neighborhood of a self focusing. They applied a non paraxial algorithm for a scalar wave equation to describe self-focusing of the beam and their results showed that self-focusing is non-catrospic. Recently by using a nonlinear Helmholz equation Brauch et. al [47] has shown numerical evidence that non paraxibility and back scattering can arrest the collapse. In this research work, we assume that our beam waist is much bigger than the wavelength and our power (low power) is slightly greater than the critical power, so

we made the theoretical calculation by using the nonlinear wave equation. The relation between the focal distance Z_f and applied power P as given by Boyd [39]

$$Z_f = \frac{2n_0}{0.61}\frac{\omega_0^2}{\lambda}\sqrt{\frac{P_{cr}}{P}} \tag{3.19}$$

where n_0 is the refractive index of the bulk of the material, ω_0 is the beam radius, λ is the wavelength and P_{cr} is the critical power at which the beam would propagate in a self-trapped mode. The critical power P_{cr} can be written as

$$P_{cr} = \frac{(1.22)^2 \lambda^2 c}{128 n_2} \tag{3.20}$$

where n_2 is the nonlinear refractive index and c is the velocity of light. The critical power can be defined as the power required by the beam to overcome the diffraction action. For the methanol ($n_2 = 2\text{x}10^{-16}$ cm^2/W) [48] at the wavelength of 800 nm, the critical power is found to be 1.5 MW.

3.1.4 Continuum Generation

When a high intensity laser passes through the material, the laser pulse self focuses first forms a filament and white light is emitted from all positions of the filament in the forward direction. The super continuum has a divergence as good as that of the input laser pulse [49]. The studies of continuum generation in noble gases with weakly focused femtosecond pulses have lead to the suggestion that self-focusing plays a critical role in the process as well [50]. The continuum generation is a universal phenomenon in

all transparent optical media and is mainly due to self-phase modulation (SPM) [51]. The development of very powerful femtosecond laser pulses even allow the generation of such a continuum without focusing by a lens. The generation of the broad anti-Stokes part of the CG is due to the SPM of the self focused pulse in the self-created plasma. The narrow Stokes broadening is due to SPM in the neutral Kerr medium which also contributes to a narrow part of the anti-Stokes side. A recent study shows that the threshold for continuum generation coincides with the threshold for catastrophic self-focusing [49].

3.1.5 Optical Breakdown

When laser intensity is in the range of 10^{11} W/cm^2 to 10^{12} W/cm^2 , the transparent material is ionized by multi-photon absorption and a plasma with a high temperature of several thousands Kelvin is formed [35]. This process is called optical breakdown. The physical processes associated with this process are plasma formation, shock wave generation and cavity formation. Plasma formation begins during the laser pulse and the ionized state last for several nanoseconds after the laser action**.**

3.1.6 Two-photon Processes

The phenomenon was originally predicted by Maria Goeppert-Mayer in 1931 [52]. It is a third-order nonlinear optical process. Two-photon absorption (TPA) is the simultaneous absorption of two photons of identical or different frequencies in order

to excite a molecule from one state (usually ground state) to a higher energy electronic state. The energy difference between the involved lower and upper states of the molecule is equal to the sum of the energies of the two photons. Two-photon absorption is many orders of magnitude weaker than one photon absorption .The probability of a molecule to absorb two photons simultaneously is proportional to the square of the intensity of the input beam [53]. The compression of the pulse and the simultaneous increase of the intensity lead to an increase the intensity of TPF [54, 55].

The intensity of two-photon fluorescence signal can be written as

$$I_{\mathrm{TPF}} = \frac{I}{1+\beta cxI} \tag{3.21}$$

where x is the path length or cross section, c is the concentration and the I is the initial light intensity. Equation (3.22) can be written as

$$I_{\mathrm{TPF}} = \frac{I}{1+\alpha I} \tag{3.22}$$

where $\alpha = \beta cx$,

The laser beam intensity is

$$I = I_0 \frac{w_0^2}{w^2} e^{-2r^2/w^2} \tag{3.23}$$

inserting equation 3.24 into equation 3.23 gives

$$I_{\mathrm{TPF}} = I_0 \frac{w_0^2}{w^2} \frac{e^{-2r^2/w^2}}{1+\alpha I_0 \frac{w_0^2}{w^2} e^{-2r^2/w^2}} \tag{3.24}$$

Let's consider $\gamma = I_0 \frac{w_0^2}{w^2}$ and let $\delta = 2 / w^2$ so that

$$I_{\text{TPF}} = \gamma \frac{e^{-\delta r^2}}{1 + \alpha\gamma e^{-\delta r^2}}$$

We want to integrate over the area of the beam. The TPF signal is therefore

$$S_{\text{TPF}} = \gamma \int_0^\infty \frac{e^{-\delta r^2}}{1 + \alpha\gamma e^{-\delta r^2}} r dr d\theta \tag{3.25}$$

Let $\xi = r^2$ so that $d\xi = 2rdr$

$$S_{\text{TPF}} = \frac{\gamma}{2} \int_0^\infty \frac{e^{-\delta\xi}}{1 + \alpha\gamma e^{-\delta\xi}} d\xi d\theta$$

Now, let $\eta = 1 + \alpha\gamma e^{-\delta\xi}$ so that $d\eta = -\delta\alpha\gamma e^{-\delta\xi} d\xi$ which gives $-\frac{1}{\delta\alpha\gamma} d\eta = e^{-\delta\xi} d\xi$. Our integral becomes

$$S_{\text{TPF}} = -\frac{1}{2\delta\alpha} \int_0^\infty \frac{1}{\eta} d\eta d\theta$$

$$S_{\text{TPF}} = -\frac{1}{2\delta\alpha} \int_0^\infty \frac{1}{\eta} d\eta d\theta \tag{3.26}$$

the angular integration

$$S_{\text{TPF}} = -\frac{\pi}{\delta\alpha} \int_0^\infty \frac{1}{\eta} d\eta \tag{3.27}$$

the η integral

$$S_{\text{TPF}} = -\frac{\pi}{\delta\alpha} \ln|\eta| \Big|_{r=0}^{r=\infty} \tag{3.28}$$

(3.28)

substituting back to r

$$S_{\text{TPF}} = -\frac{\pi}{\delta\alpha} \ln\left|1 + \alpha\gamma e^{-\delta r^2}\right| \Big|_{r=0}^{r=\infty}$$

$$S_{\mathrm{TPF}} = \frac{\pi}{\delta\alpha}\left(-\ln|1| + \ln|1+\alpha\gamma|\right) \tag{3.29}$$

putting back in for α, δ and γ, we get

$$S_{\mathrm{TPF}} = -\frac{\pi w^2}{2\beta c x}\left(\ln|1| - \ln\left|1 + I_0\beta c x\frac{w_0^2}{w^2}\right|\right) \tag{3.30}$$

Two-photon fluorescence intensity given by equation (3.20) has Lorentzian profile as shown in Fig. 3.2

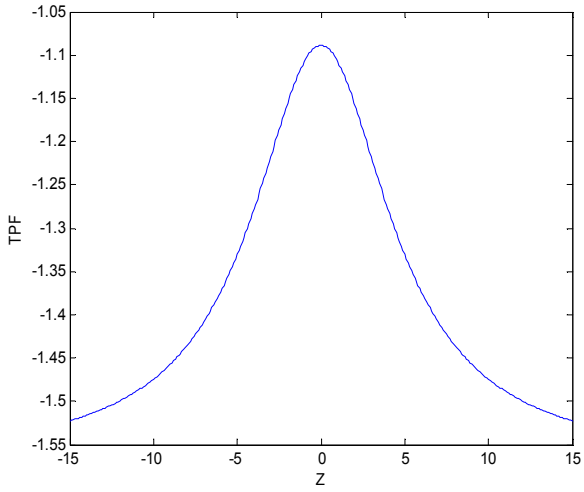

Fig 3.2 Two-photon fluorescence signal (This result is based on the above model)

3.2 Study of Nonlinear Effects Using Two-photon Fluorescence and Z-scan

In the conventional Z-scan method [18, 56], the sample under investigation is moved through the focus of the laser beam and the nonlinear effects such as two-photon absorption, self-phase modulation are conveniently studied by measuring the

corresponding changes in shape and transmission of the laser beam [43]. In particular the two-photon fluorescence when combined with the Z-scan technique proved to be an efficient tool for studying nonlinear dynamics of ultra-short laser pulses. We used a combination of several detection techniques to reveal the interplay of the nonlinear processes in TPF, continuum generation and the transmission signal.

The experimental setup is shown in Fig. 3.3. The 15 fs laser pulses produced by the Menlo system oscillator (Femtolaser) are sent to an acousto optical modulator (Dazzler, Fastlite). After that it is sent to the regenerative amplifier (Spitfire, Spectra Physics) which produces 45 fs pulses. The pulse duration was measured using a GRENOUILLE [28]. The initial laser beam was split into two parts. One sub-beam was focused by using a achromatic lens with 12.5 cm focal length**,** on a quartz cuvette with 1 mm optical path length containing a 1mM solution of Coumarin-30, and the emitted two-photon fluorescence signal was optically filtered and detected by a photo-diode. The other sub-beam was focused on a BBO crystal to produce the second harmonic radiation, which was filtered and detected also by a photo-diode. A mechanical chopper with 500 Hz modulation frequency synchronized the laser pulse repetition rate of 1 kHz, so that the pulses were alternatively transmitted and blocked. The signal was detected with a lock-in amplifier referenced to the chopper, thus allowing the implementation of narrow band detection and a reduction of background noise by background subtraction and integration

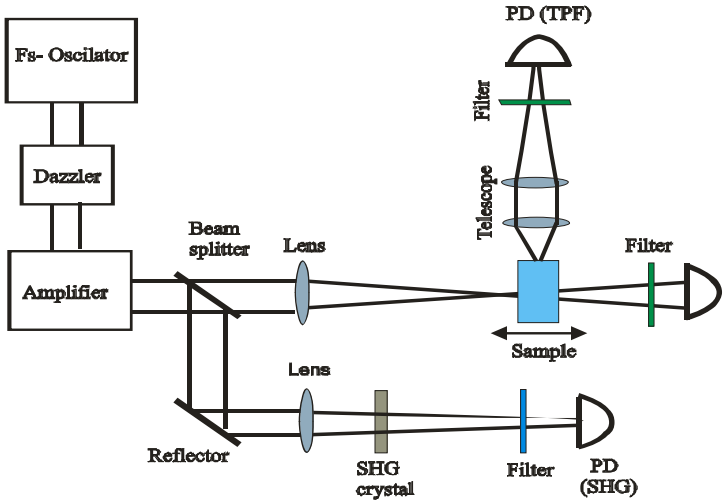

Fig. 3.3 Experimental setup

Coumarin-30 dye with a concentration of 1mM was used as a sample. In the Z-scan technique, the distance between the sample and the lens position is changed and in this way the intensity of the laser beam also changes. In our set-up the cuvette with the sample was fixed and lens position was varied using a translation stage controlled by a stepping-motor (Mike controller). The Z position was varied from -12.1 mm to + 12.1 mm where Z is measured from the focus of the lens and minus sign corresponds to the position of the sample closer to the lens and the focal distance.

3.2.1. Results

In order to check whether the detected signal is caused by two-photon excitation, the fluorescence signals (green around 520 nm) from two different kinds of

detectors (photodiode and ocean optics spectrometer) were registered when laser power at a fixed Z position (Z = -10 mm and -3 mm) was varied. Fig. 3.4 (a) and 3.4 (b) show the relation between fluorescence intensity and applied power at a fixed Z. In figure 3.4(a), which corresponds to Z = -10 mm and a relatively low intensity, the dashed curve line is a quadratic fit and a good approximation to the experimental data of this curve , confirms that the detected signal is indeed a two-photon process. Fig. 3.4(b) which corresponds to relatively higher intensity shows the appearance of a saturation effect when the input laser power is high enough at Z = -3 mm position.

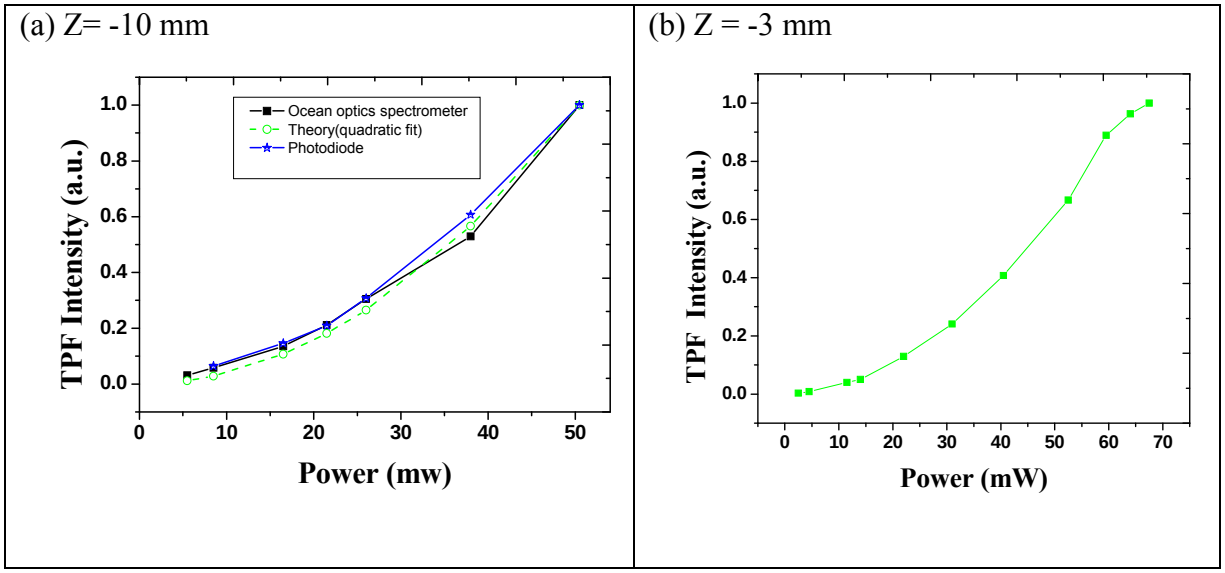

Fig.3.4 Two-photon fluorescence versus laser power at different Z (a) Z = -10 mm (lower intensity) and (b) Z = -3 mm (higher intensity)

This graph indicates that the TPF signal is quadratically dependent on the input laser intensity for Z = -10 mm and there is saturation effect for Z = -3 mm

3.2.2 Power Dependence

By varying the applied laser power, a systematic study was performed. According to the applied laser power, the different manifestation of the nonlinear processes corresponds to three regions as follows:

A. Low Input Power Region: the average laser power is less than 0.5 mW**.**

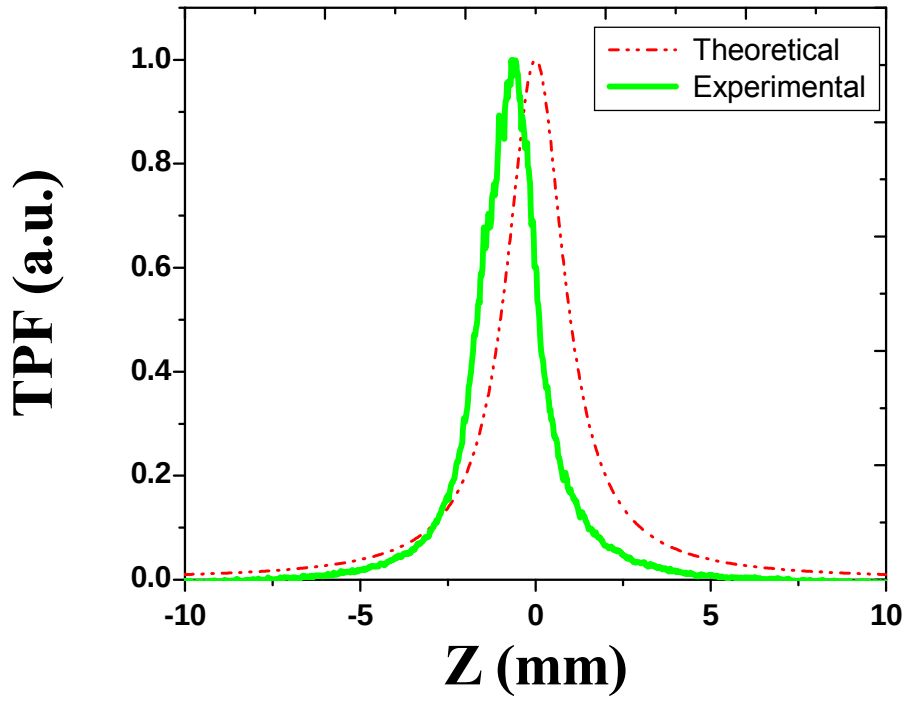

Fig. 3.5. Two-photon fluorescence at P = 320 μW. A small displacement of the TPF maximum from the focal point is due to the onset of self-focusing

Fig. 3.5 shows that the TPF signal during Z-scan at lower laser power. The solid line is measured TPF signal and the dot line is from theoretical calculation for the Gaussian beam taking beam radius of 8 μm. The shift due to self-focusing was found to be 0.6 mm for peak power 320 μW. The peak of the calculated TPF signal is exactly at the Z = 0, whereas the measured one is shifted towards the laser direction. This is due to the self-focusing effect. By varying laser power, a change of the focal position due to the self-focusing effect can be observed. This change can be calculated by using equation (3.19) & (3.20). We calculated the critical power for the self-focusing using equation (3.20) and was found for methanol to be 1.5 MW. For the initial average power of 0.3 mW, the peak power is around 6 MW; therefore the influence of self-focusing is already significant at this power level.

B. Intermediate Region: laser power region between 0.5 and 15 mW. Several TPF Z scan measurement were done on this region. Fig. 3.6 (a), (b), and (c) show the dip in the TPF spectrum which is due to the contribution from various nonlinear effects. When the self-focusing overcomes the diffraction effect, it leads to a quick increase of the peak intensity of the laser pulse, which produces the first maximum of the TPF signal. The increase of the laser intensity initially, leads to an increase of the TPF signal due to the rapid grow of the two-photon absorption by the dye molecule. At high laser intensity, the plasma formation overcomes the self-focusing effect and laser pulse starts to defocus, this defocusing and possibly optical breakdown produce the

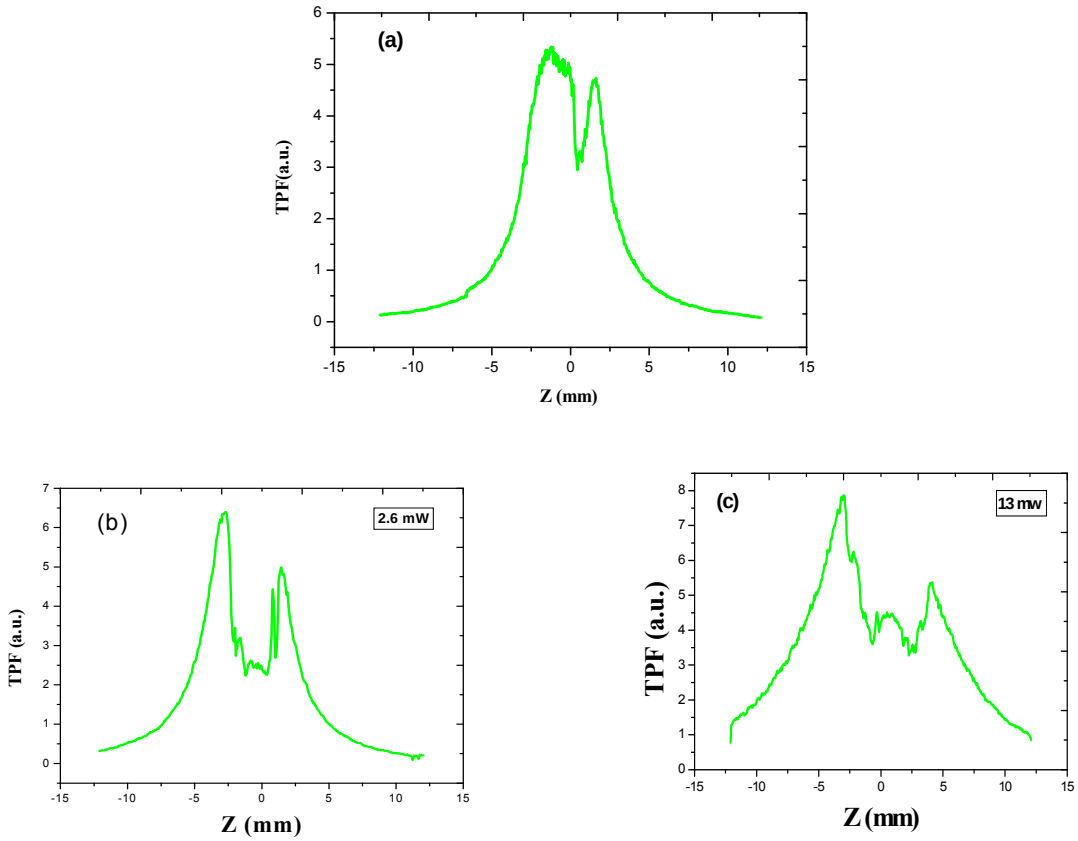

Fig. 3.6. Intensity clamping; drop and increase (a) P=0.65 mW, (b) P = 2.6 mW (c) P = 13 mW.

intensity clamping [19]. The sudden rise of the fluorescence after the geometrical focus is due to the sudden reduction of plasma formation, in the Z range where the intensity clamping was observed. We have also observed a reduction in the white light generation. Fig. 3.6 (b) & (c) also shows that the Z-scan spectrum (the area between two peaks) becomes broader with increasing applied laser power.

c. High Power (Saturation region): High input power region more than 15 mW.

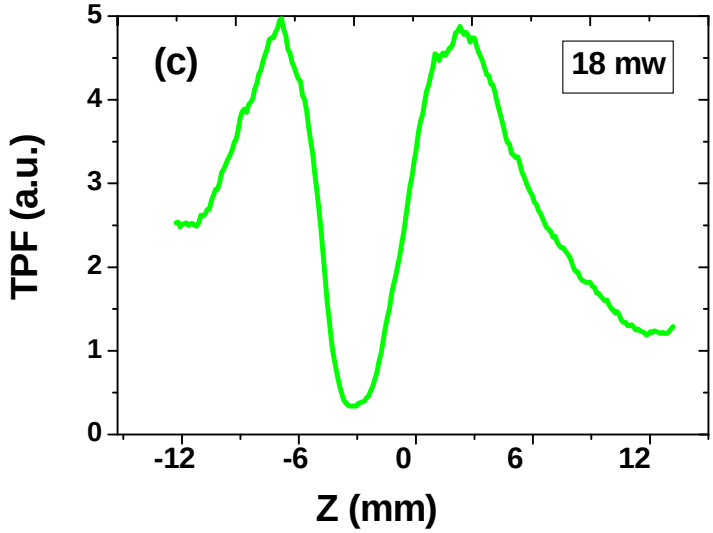

Fig. 3.7 Z-scan measurement of TPF at input power, P = 18 mW.

The results obtained after the saturation is shown in Fig. 3.7, where the filamentation has been broken down and more and more hot electrons are generated through tunnel ionization of the dye molecule near the self-focal zone. The threshold power for saturation effect for Coumarin-30 was found 20 mW which corresponds to the intensity of $8*10^{12}$ W/cm^2. Fig. 3.6 shows that the fluorescence peak before and after the minimum point are at the same height, this happened when saturation effect is dominant than other nonlinear effects.

3.2.3 Simultaneous Measurements of Nonlinear Effects

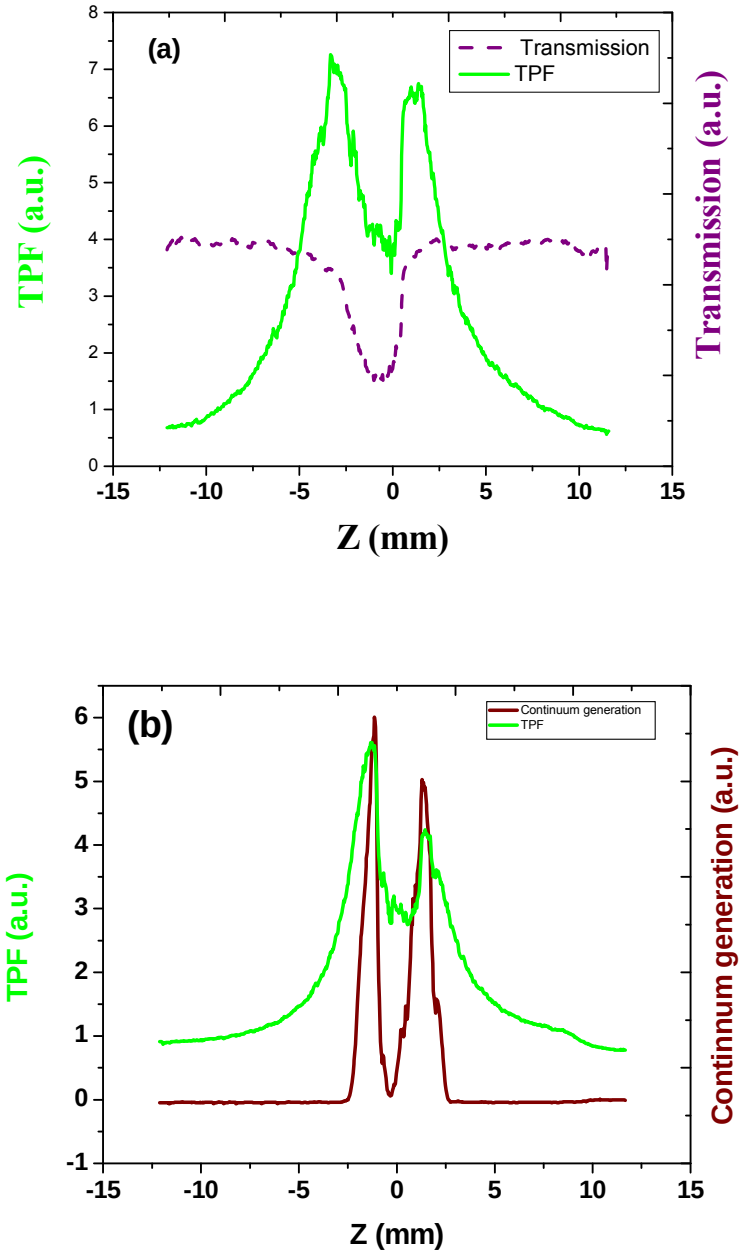

Fig. 3.8. Simultaneous measurements at P = 2 mW: (a) TPF and transmission; (b) TPF and continuum generation.

To measure the TPF and other effects like transmission and continuum generation simultaneously, the cuvette and detector for TPF were set on the same translation stage which was moved by a stepping motor (Mike Controller). Fig. 3.8 (a) shows that the wide dip in the middle part of the two-photon fluorescence Z-scan spectrum and the deep minimum of the transmission Z-scan spectrum are at the same Z position. This shows that the wide deep in the middle part of the TPF signal is due to the ionization of dye molecules from multiphoton and cascade ionization. A filter was used to block the white light and other light less than 750 nm. Fig. 3.8 (b) illustrates the simultaneous measurement of the TPF and continuum generation (CG) signals showing the peaks at the same Z position of the. This is due to the strong self-phase modulation. To filter out the fundamental laser light at 800 nm BG-39 filter was used before the white light continuum generation detector.

In addition, Fig. 3.9 shows the transition measurement of white light of methanol solution of coumarin-30 dye without using any filters when the input power was set at the saturation region (P = 31 mW) measured by the detector of ocean optics, where strongest part is belong to the input laser at 800 nm wave region, the middle part around 750 nm is belongs to white light, the weakest part is around 550 nm come from the fluorescence following two-photon excitation. As this is at the blue part (blue broadening) of input laser, it can identified that it is arise from plasma generated by multi-photon ionization which is in agreement with our analysis of TPF measurement in the saturation region. The asymmetric pulse broadening is due to self steepening processes [43].

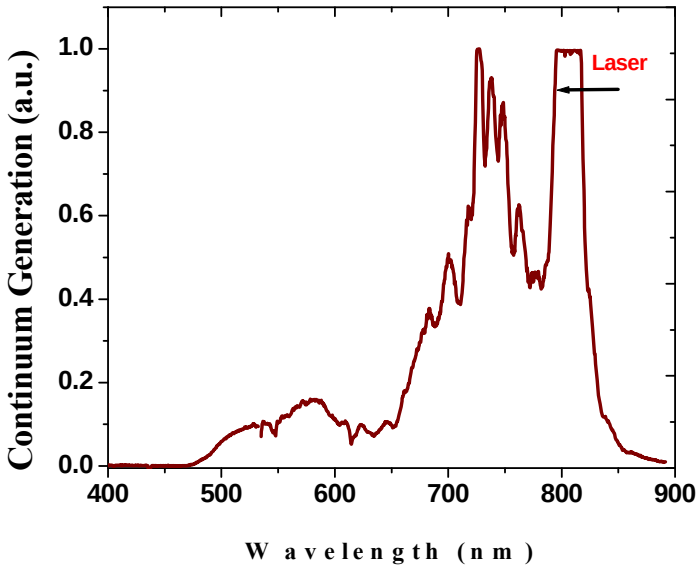

Fig. 3.9. Transition measurement without any filter at P = 31 mW.

3.2.4 Universality

Above Z-scan experiments were repeated for several dyes and biomarkers namely DCM and Melanin. The results obtained were similar to that of Coumarin-30 dye. Fig. 3.10 shows the Z-scan measurement of TPF from DCM dye on 1 mm cuvette with 150 μW.

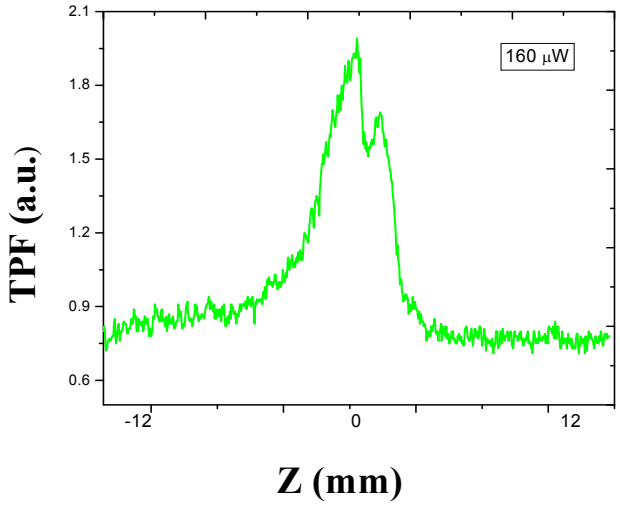

Fig. 3.10. Z-scan measurement of TPF spectra of DCM dye with 160 μW input power.

Similarly, Fig. 3.11 shows Z-scan measurement of TPF of DCM dye on the 1cm cuvette with 10 mW input power.

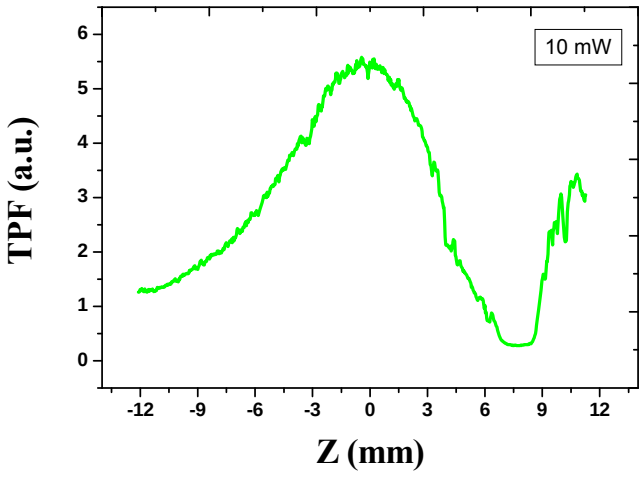

Fig. 3.11. Z-scan measurement of TPF spectra with 10 mW input power with 1cm thick cuvette.

3.2.5 Experiment with Varying Linear Chirp (SOD)

The measurement was performed by implementing a varying linear chirp. One full scale Z-scan spectra with one given chirp has been measured which is shown in Fig. 3.12, where the first, second and third scan were made with -1100 fs^2, 0 fs^2 and 1300 fs^2, respectively.

With negative or positive chirp, the pulse becomes broader with lower peak power than the transform limited pulses having the same energy. So the threshold energy for different nonlinear effect will also increase. At the zero chirp, the competition effect is very strong than both the negative and positive chirp. With negative chirp (-1100 fs^2) it is the weaker than the positive chirp (+ 1300 fs^2) .

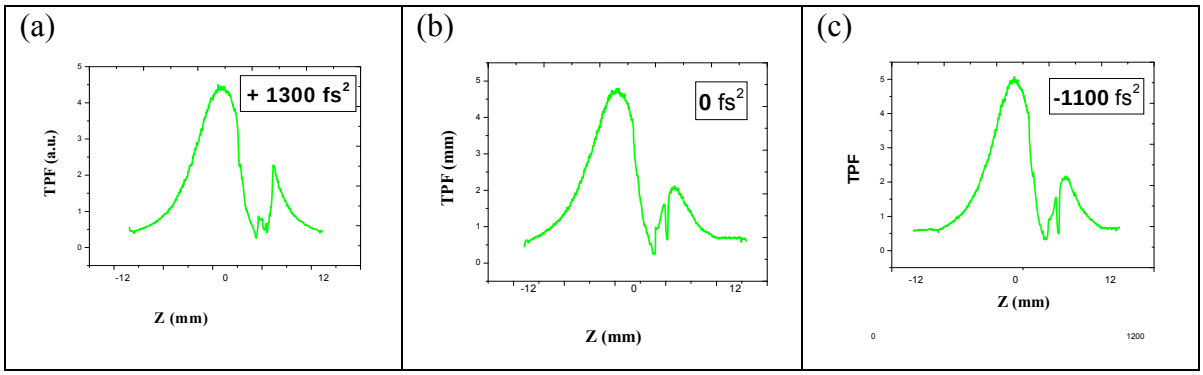

Fig. 3.12. Effect of a linear chirp on the two-photon fluorescence of Coumarin-30 dye.

3.3 Visual Observation of Filamentation

With high input power, filamentation was observed on methanol solution using optical microscope. We found that the numbers of filaments depends on the beam size. Therefore the beam size was changed using an aperture before the focusing lens.

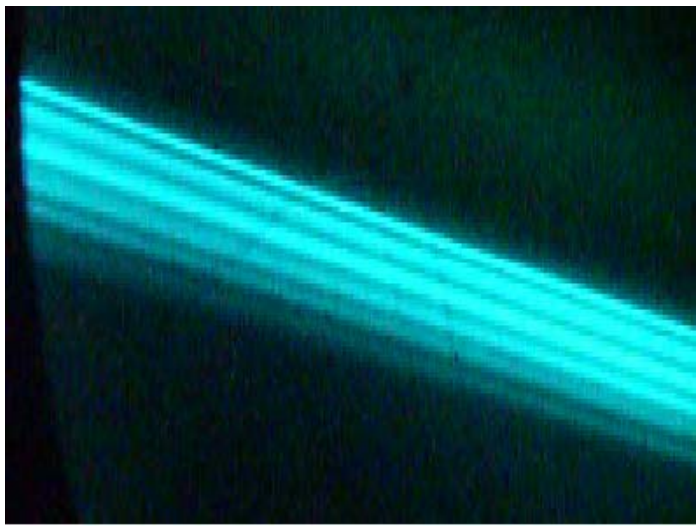

Fig. 3.13. Filamentation in a on methanol solution of Coumarin-30 produced by using a lens of focal length 125 mm at an input power (P) = 45 mW with a cuvette size of 6 cm path length. The laser direction is from left to right

A Microscope (magnification 30 times) was used to visualize these filaments. Fig. 3.13 shows filamentation of laser beam after passing through the methanol solution of Coumarin-30. Table 3.1 shows the relation between aperture size(beam radius) and no of filaments observed. From the data from the table it can be concluded that with large aperture size more no of filaments are visible. These filaments

are due to the splitting of laser beam itself after propagating through the medium. If we consider the Gaussian laser pulse, we know that the intensity are not symmetric everywhere and due to self-focusing effect it start to focus and several filaments were formed. But when aperture size is reduced and intensity profile of the beam looks more symmetric, no of filaments were reduced. Such filaments were also observed when laser pulse propagates through very long cuvette (1 meter).

Table 3.1. Relation between aperture size and number of filaments.

Aperture Size (mm)	Number of Filaments
4.2	3
5.1	4
8.4	7

3.4 Experiments with Jet

Usually a glass cell is used for measurements with the solutions, but for observation of saturation effects and optical breakdown, higher intensities are required and the results can be compromised by such nonlinear effects in glass as self-focusing, self-phase modulation and white light generation. To avoid the influence of glass we performed experiments with a liquid flow jet. Experimental setup using liquid jet is shown in Fig. 3.14.

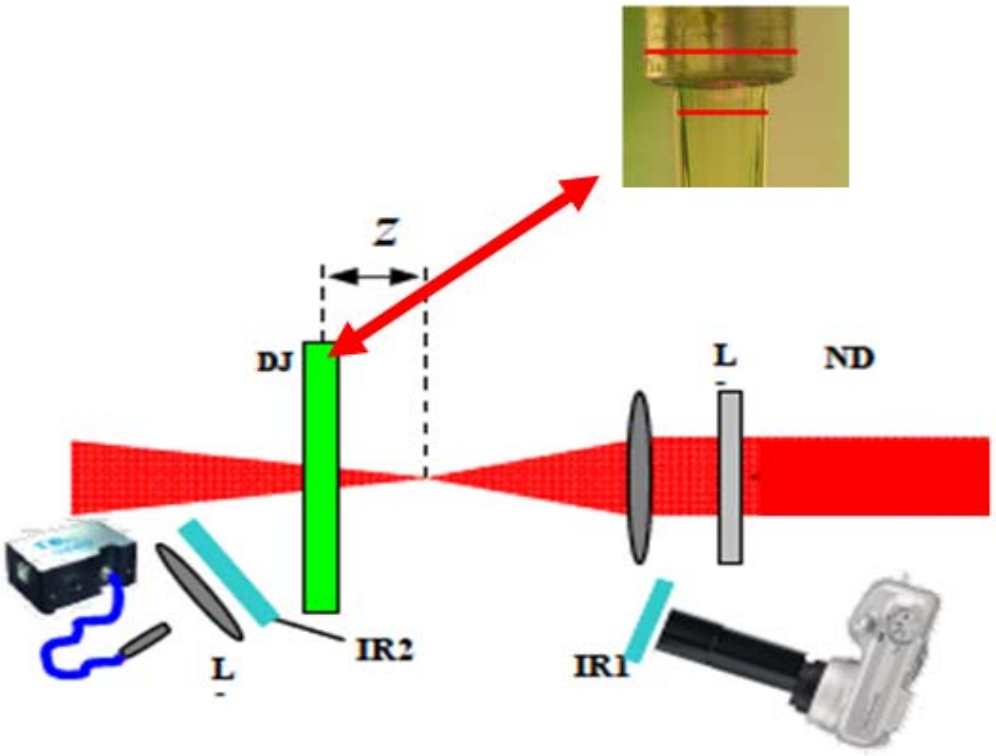

Fig. 3.14. Experimental setup with liquid jet flow.

Different lenses of focal lengths (200, 300, 550 and 850) mm were used to produce the different beam waists. Z-scan measurements were done using each of these lenses and results were compared. The fluorescence was detected using Ocean Optics spectrometer. Fig. 3.15 shows the graph between TPF signal and applied laser power. The laser power was varied from 78 μW to 16 mW by using neutral density filter and the focal length of lens used was 320 mm.

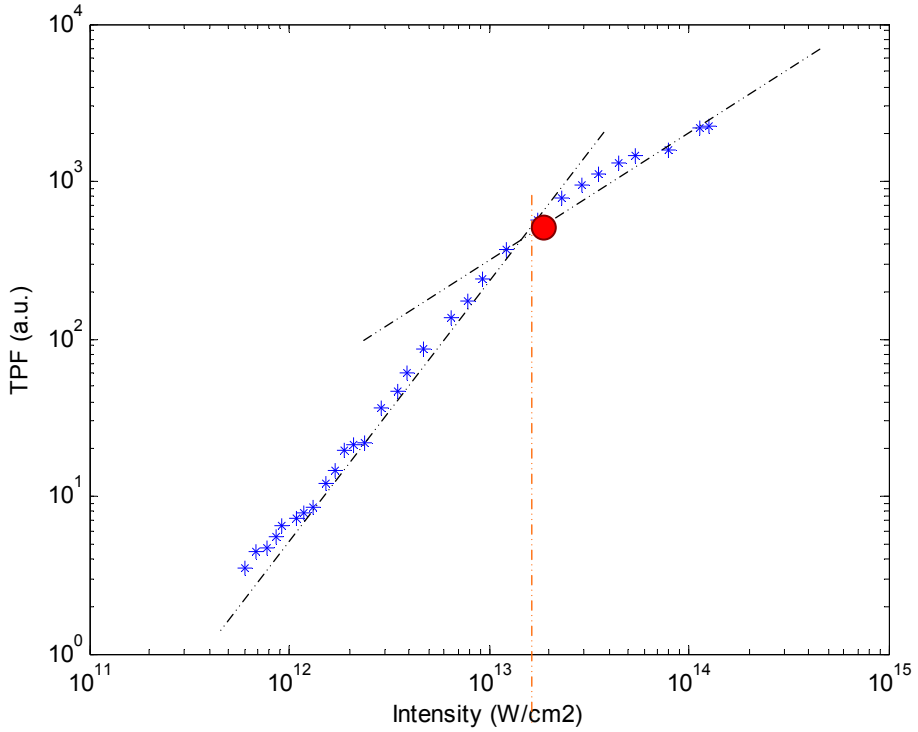

Fig. 3.15. Two-photon fluorescence versus intensity on log-log scale. The red dot is the saturation threshold. Lower part is the graph is slope of 2, which consists with the two-photon process.

The red dot on the graph shows the saturation intensity, which is found to be $2*10^{13}$ W/cm^2. Fig. 3.16 shows the Z-scan measurement using a lens of focal length 320 mm. Each curve shown on the graph was from different power scan ranging from 5 to 60 mW.

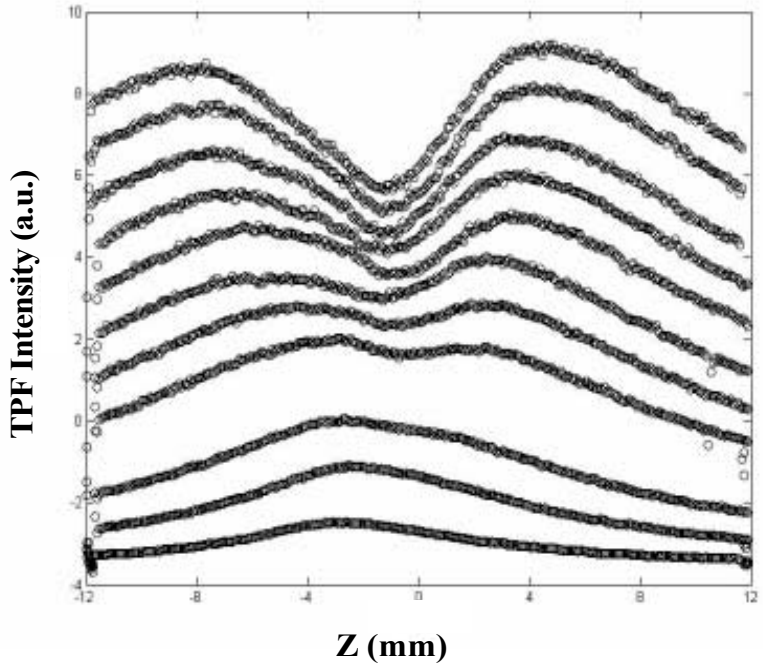

Fig. 3.16. Z-scan measurement of TPF of coumarin-30 dye using a jet with lens of 320 mm focal length and the beam waist is 0.8 mm.

3.5 Two-Photon Probability and Saturation Intensity

The role of two-photon (TP) processes increases with the intensity, since they exhibit quadratic intensity dependence, however after reaching a certain threshold value of the intensity, the further growth of the TP absorption and fluorescence is impeded. A Z-scan technique provides a convenient way to measure intensity dependences of nonlinear optical processes in a broad range. However, the distribution of the laser intensity over the cross section of the laser beam as well as the diffraction

effects make it necessary to develop a procedure for extracting the physical parameters from the measured signals.

Usually, the data obtained for characteristics of the TP processes are averaged, since each laser pulse used in the measurements has spatial and temporal intensity distribution that is not accurately accounted for in the measurements. Obtaining of the intensity-resolved data is important for comparison of the theoretical models of the interaction of optical radiation with molecular systems.

In this research work, several methods to overcome this limitation and to obtain TP characteristics in an intensity-resolved manner are implemented. We studied experimentally two-photon fluorescence in a broad intensity range with the Z-scan method. Also a theoretical model was developed describing the saturation of the TP fluorescence signal in the Z-scan. A procedure is presented to solve the inverse problem of extracting the saturation dependence of the fluorescence on the laser intensity from the observed fluorescence signal. By fitting this model to the experimental data we can determined the TP fluorescence saturation threshold as well as the two-photon fluorescence probability.

We proposed several methods two find the two-photon probability, some of these methods are:

(a) Inversion technique for the Z-scan method to retrieve intensity –resolved data.

(b) Single snap-shot technique for obtaining intensity-resolved data via TPF-intensity mapping.

3.5.1 Inversion Technique for the Z-scan Technique, Removing the Spatial Averaging

It is possible to deconvolve two-photon probability directly from data for experiment in which the detection volume is restricted [20, 21]. This inversion technique is applied to two-photon fluorescence of Coumarin-30 dye.

We would like to find the two-photon probability P (I(r,z)) , related to measurable quantity in the following way

$$Y\left(I_0\right) \propto \iint P\left(I\right) dV(I, I_0) \tag{3.31}$$

where $Y(I_0)$ is the measured two-photon fluorescence and dV is the real space volume. Here, we assume that the Gaussian pulse intensity I is given by

$$I = I_0 \frac{\overline{\omega_0^2}}{\omega^2} e^{-2\frac{\overline{r^2}}{\omega^2}} \tag{3.32}$$

.

It follows,

$$\ln\left|\frac{\overline{I}}{I_0}\frac{\overline{\omega^2}}{\omega_0^2}\right| = 2\frac{\overline{r^2}}{\omega^2} \tag{3.33}$$

$$r^2 = \frac{\overline{\omega^2}}{2} \ln\left|\frac{\overline{I}}{I_0}\frac{\overline{\omega^2}}{\omega_0^2}\right| \tag{3.34}$$

and volume V can be written as $V = \Delta z 2\pi r^2$, where Δz is the sample thickness. Now by using the chain rule we have

$$Y(I_0) \propto \iint P(I) \frac{\partial V}{\partial I} dI \tag{3.35}$$

Here,

$$\frac{\partial V}{\partial I} \propto \frac{1}{I_{0L}(z)} \frac{1}{I} \tag{3.36}$$

where I_{0L} local on axis peak intensity

So by substituting equation (3.36) into equation (3.35) we have

$$Y(I_0) \propto \frac{1}{I_{0L}} \iint P(I) \frac{1}{I} dI \tag{3.37}$$

We want to get $P(I)$ out of the integral, because $P(I)$ is the fundamental quantity. First, we multiply both sides by $I_{0L}(z)$, then take the derivative with respect to the coordinate z, and by applying the Leibnitz rule [57]

$$P(I) \propto \left[\frac{I_{0L}}{dI_{0L} / dz} \right] \frac{d}{dz} \left[I_{0L}(z) Y_{ISS}(z) \right] \tag{3.38}$$

In experiment $Y(I)$ is found by measuring the TPF signal of Coumarin-30 dye using photodiode with a jet at different Z position.

Z-scan measurement, as described earlier in the chapter, is taken using liquid jet of Coumarin-30 dye dissolved in methanol. The jet used is from a commercial dye laser (Spectra Physics-380). Typical flow speed was ~ 10 m/s and the dimension of the jet were 0.5 mm along the laser propagation direction and 3 mm perpendicular to the

propagation direction. The graph shown in Fig. 3.17 is obtained by using lens of focal length of 320 mm. Input power is 26.5 mW and we vary Z with respect to the sample position. The experimental set up is shown in Fig 3.14.

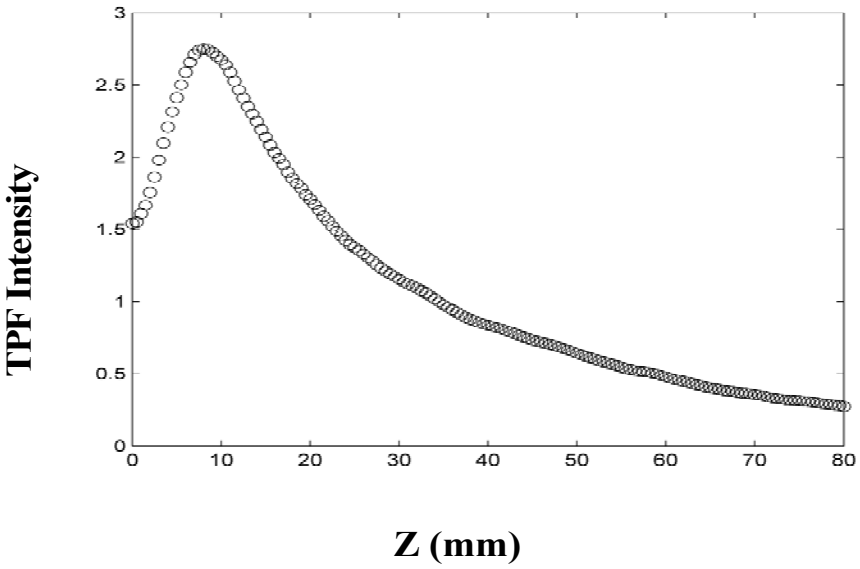

Fig. 3.17. Z-scan measurement of TPF by using a lens of 320 mm focal length and the input laser power of 26.5 mW.

By using equation (3.38) and known beam parameters we can invert the z-scan data from Fig. 3.17 to retrieve the TPF probability curve.

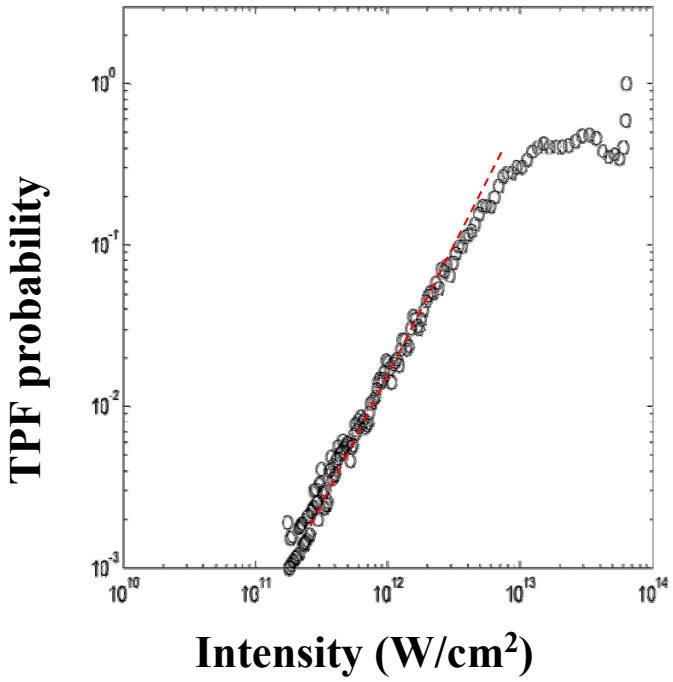

Fig. 3.18. Measurement of the TPF as a function of peak intensity integrated over the full volume of the focus. Red dotted line indicates a slope of two and shows that the measured signal is consistent with two-photon processes.

Fig. 3.18 shows a log-log plot of the deconvoluted dependence of the TPF output on the intensity. From this graph we can get two-photon probability as well as saturation intensity. The saturation intensity is found to be $2^* 10^{13}$ W/cm^2. This value of the saturation intensity threshold is in agreement with the previously obtained result from the intensity-scan (IS) method (see Fig. 3.15). The later is used as a reference for comparison of determined parameters.

Note that the data from the intensity scan (IS) method can also be used to deconvolve the two-photon probability.

3.5.2 Single Snap-Shot (SSS) Determination of the TPF Probability

An alternative method that relies on geometrical comparison of spatial laser profile with images of two-photon fluorescence is introduced. A single image from CCD was used to determine not only the saturation intensity, but also the intensity-dependent TPF probability [58, 59].

To obtain the photographic images of the TPF intensity distribution we used ethylene glycol liquid jet of 0.5 mm thickness, described earlier. This small thickness allows us to neglect the variation in intensity along the z-direction (laser propagation). The lens of focal length of 320 mm is used to focus the laser beam. Input power was varied using a variable neutral density filter and a CCD camera was used to capture the TPF images. Several BG-18 Schott filters were used to remove the IR radiation. The distance between the focal point of the lens and the sample (the jet) is about 2 cm. Knife edge method was used to find the beam radius at the interaction point.

Following assumptions were made

1) The jet thickness is small enough so that the variation of the beam profile along the propagation direction is negligible.

2) The resolution of the images is sufficient allowing transverse variation (intensity gradient, $\Delta r \left.\frac{\partial I}{\partial r}\right|_{\text{ring thickness}} = 0$, over the rings to be neglected. This enables us to approximate the ring thickness by a delta function.

(3) In taking the picture we make sure the CCD camera is not saturated.

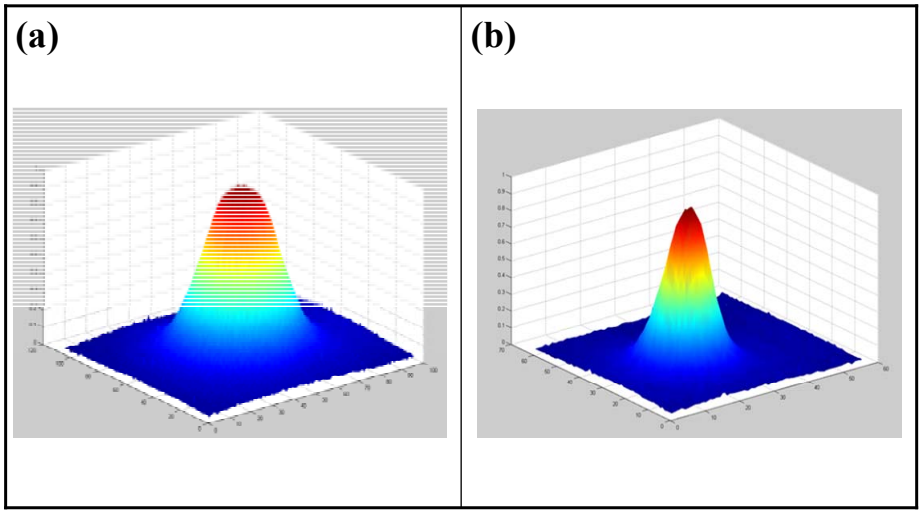

Fig 3.19 Images of the TPF distribution taken by the CCD camera. Input power (a) 2.8 W (b) 0.3 W.

In Fig 3.19 (a) we can see the top is flat compared to fig 3.18 (b). When the dye molecules are saturated the top part in the picture becomes flatter and flatter.

Now, we can write the normalized volume integrated product yield Y as

$$Y = \frac{\int_{\Omega} P(I)dV}{\int_{\Omega} dV} \tag{3.39}$$

The differential volume element chosen to integrate over is,

$$dV = A_0 \frac{\delta(r'-r)}{r'} r'dr'd\theta dz \tag{3.40}$$

Substituting this differential volume element into equation (3.28) and dividing the result by the volume or the ring gives

$$Y = \frac{A_0 \int P(I') \frac{\delta(r'-r)}{r'} r' dr' d\theta dz}{A_0 \int \frac{\delta(r'-r)}{r'} r' dr' d\theta dz} \tag{3.41}$$

If the jet width is smaller than the Rayleigh length, then to a good approximation the intensity becomes independent in z, $I \neq I(z)$.

$$Y = \frac{2\pi \Delta z A_0 \int P(I') \frac{\delta(r'-r)}{r'} r' dr'}{2\pi \Delta z A_0 \int \frac{\delta(r'-r)}{r'} r' dr'} = \frac{2\pi \Delta z A_0 \int P(I') \delta(r'-r) dr'}{2\pi \Delta z A_0 \int \delta(r'-r) dr'} \tag{3.42}$$

It can be shown that $\delta(r'-r) = \delta(I'-I)\frac{\partial I'}{\partial r'}$ where $I \leq I_0$ so that

$$Y = \frac{2\pi \Delta z A_0 \int P(I') \delta(I'-I) dI'}{2\pi \Delta z A_0 \int \delta(I'-I) dI'} \tag{3.43}$$

Evaluating the integral over the delta function gives

$$Y = \frac{2\pi \Delta z A_0 P(I(r))}{2\pi \Delta z A_0} = P(I) \tag{3.44}$$

where I is our measured TPF signal and P is the TPF probability.

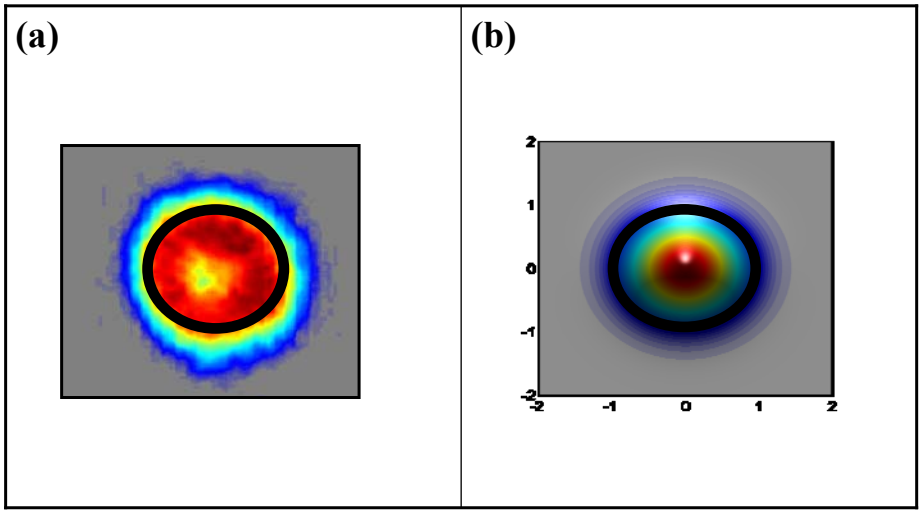

Fig 3.20 (a) Two-photon fluorescence signal from CCD camera (b) theoretically calculated intensity distribution.

Fig 3.20 (a) shows the picture of two-photon fluorescence from CCD camera and (b) shows the intensity distribution. For example black disk of from experimental picture (a) is compared with theoretical one (b) to get intensity resolved two-photon probability

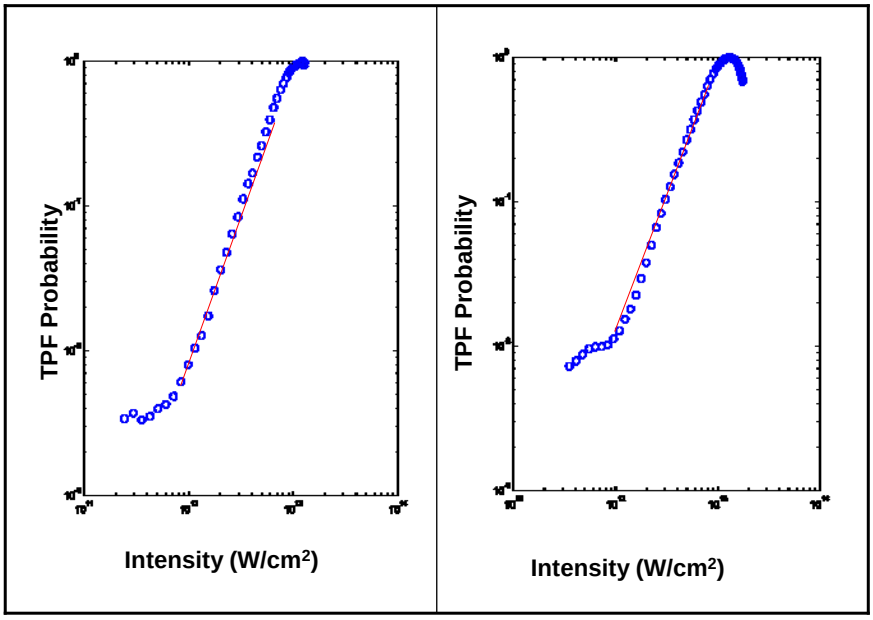

Fig 3.21: Log-Log plot two-photon fluorescence probability versus laser intensity. Results obtained with the input power (a) with 2.3 W (b) with 1.5 W.

Fig 3.21 shows the log-log plot of the two-photon fluorescence probability versus laser intensity. These dependences were obtained taking into account mapping of two-photon fluorescence signal image and the laser intensity profile. Both higher power (a) and lower power (b) measurements give the same probability and saturation intensity.

3.6 Conclusion

A systematic study of the power and intensity dependences of the two-photon fluorescence of methanol solutions of Coumarin-30 dye was performed using the Z-scan technique. Self-focusing, saturation and other nonlinear optical physical processes were

studied by performing simultaneous measurements of TPF and transmission or white light continuum generation. The measurements were performed at the power level well above the critical power for self-focusing effect, which was found to be 1.5 MW for methanol. So, self-focusing effect leads the shift of the focus towards laser direction. When self-focusing effect was balanced by the plasma generation (free electrons), it defocuses the pulse. This defocusing and possible optical breakdown leads to the intensity clamping. At higher laser power the saturation effect was observed. For the white light continuum generation, threshold energy was found to be 1μJ for lens of 125 mm and beam radius 5 mm. With varied laser power the formation of different number of filaments in the laser beam was observed and visualized through the two-photon fluorescence.

We have proposed and implemented different new methods to find the saturation intensity and two-photon probability. These include intensity scanning (IS) by adjusting the input laser power, Z-scan or intensity selective scanning (ISS) and single snap shot technique (SSS), using a digital camera to image the TPF spot on our dye jet.

Table 3.2 Saturation intensity of methanol solution of Coumarin-30 dye.

Methods	ISS	Z-scan	Single Snap Shot (SSS)
Saturation Intensity	$8*10^{12}$ W/cm^2	$2*10^{13}$ W/cm^2	$2*10^{13}$ W/cm^2

Table 3.2. Shows the saturation intensity of coumarin-30 obtained from three different methods. The results obtained were comparable. Additionally, theoretical models were presented that solved the inverse problem needed to obtain TPF probabilities.

To the best of our knowledge, we present the first reported measurements of intensity resolved two photon probabilities.

CHAPTER IV

COHERENT CONTROL WITH AN EVOLUTIONARY ALGORITHM

Optimizing two-photon fluorescence is a process which when being optimized needs to be adapted to the situation at around and at conditions where other nonlinear process should be taken care. Two-photon fluorescence signal can be weak and optimization of it helps to differentiate from other processes and use it for different applications. In medical physics and in particular two-photon microscopy, the optimization of two-photon fluorescence and selective excitation has great applications. For example by using two-photon microscopy and selective excitation technique helps us to detect the cancel cell in the skins without even cutting the skin surface.

The first part of the chapter describes the basis of an evolutionary algorithm, the principle and the main parameters as well as the implementation of the evolutionary algorithm in LabView. The second part of the chapter describes the coherent control set up using the evolutionary algorithm and its performance on different physical problems.

4.1 Principles and Main Parameters of an Evolutionary Algorithm

The evolutionary algorithm bases its optimization on the principle of natural selection. It performs a “survival of the fittest” search keeping the best solutions from

the previous "generation" to sire the next. The evolutionary algorithm provides a simple and robust optimization method.

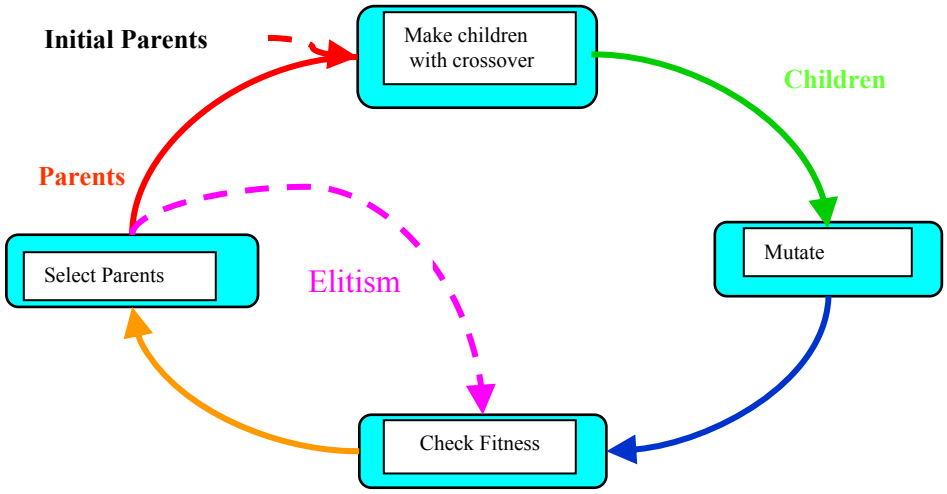

Fig. 4.1. The general scheme of evolutionary algorithm as a flow chart.

Fig. 4.1 shows the flow chart of evolutionary algorithm. The basic idea of an evolutionary algorithm is the attempt to imitate the classical picture of the evolution in a computer code which simulates selection, mutation and recombination within a feedback controlled regulation loop.

Fig. 4.2 shows the pseudo code for an evolutionary algorithm. An initial set of vectors is generated randomly. Each vector represents one search point in parameter space where the objective function is to be sampled. In analogy to evolution in nature, each search point is called an individual; the whole set of candidates is one population. At the onset of each iteration loop, the objective function for each search point in parameter space is determined, either by numerical calculation or experimentally. Each

individual is rated according to its fitness. The Selection procedure determines those vectors which will serve as a basis for next loop iteration

```
Initialization;
Generate initial population (random)
Repeat
Determine fitness of each individual
Select parents;
Generate offspring's by
        Mutation;
        Recombination
        Cloning;
Construct new population;
Repeat until termination condition is satisfied
Dump results
End
```

Fig. 4.2. Pseudo code for an evolutionary algorithm as a flow chart [60, 61].

.

In selecting parents for the next generation the choice is made with a bias towards higher fitness. The parents reproduce by copying with recombination and/or mutation. Recombination acts on the two selected parents (candidates) and results in one or two children (new candidates). There are three type of recombination, we have used in our program.

1 Single-point cross over

2 Two-point cross over

3 Multiple cross over

Mutation acts on one candidate and results in a new candidate. These operators create the offspring (a set of new candidates). These new candidates compete with old candidates for their place in the next generation. It is also possible to carry the best vectors of the old generations over to the new one, which is termed as cloning. This process can be repeated until a candidate with sufficient quality (a solution) is found or a previously defined computational limit is reached.

4.2 Implementation of the Evolutionary Algorithm with LabView

We have implemented this evolutionary strategy in a LabView programming environment into the folded 4f pulse shaper with liquid crystal modulator (LC) in an adaptive feedback system. Our particular strategy uses 48 individuals (each individual is a vector of the LC voltage). These represent one generation. For each generation the fitness value is measured for every setting of the mask. The fittest ones are taken as parents to the next generations. A new generation is built from the previous by mutation which means changing the vector elements by some random value and by recombining pairs of parents i.e. interchanging of their genes, the new generation is built. By successive repetition of this scheme, only these vectors corresponding to the highest fitness value will survive and produce offsprings. The initially generation is randomly chosen. Mutation serves as dominant search operator; therefore the extent of random change of each gene must be intelligently restricted. Excessive mutation will cause no convergence while very small mutation, on the other hand will allow only very

slow convergence. Hence an adaptive control of the mutation rate was implemented to produce a better fitness value.

Fig. 4.3 shows the front panel of the LabView program where the optimization parameters were implemented for the optimization. Each population consists of 48 phase distribution (called individuum, represented by the parameters used), successively adjusted in the convergence procedure. The phase distribution is a Taylor expansion as described earlier in Chapter II, φ(ω) was presented in a polynomial form

$$\Psi(\omega) = \Psi(\omega_0) + \left.\frac{d\Psi(\omega)}{d\omega}\right|_{\omega_0} (\omega - \omega_0) + \frac{1}{2}\left.\frac{d^2\Psi(\omega)}{d\omega^2}\right|_{\omega_0} (\omega - \omega_0)^2 + \ldots$$

where ω_0 is the central frequency, φ_0 and φ_1 determine a phase shift and a temporal shift and φ_k (k = 2-4) represent the second, third and fourth order dispersion coefficients, responsible for a variation of the pulse shape. For our purposes, the first coefficient represents the pixel number of the center of the expansion; the second coefficient represents a linear variation of the phase, and do not affect the pulse (usually set to zero).

These dispersion coefficients were used as control parameters, and their best combination, and therefore the optimal phases of the spectral components, was then sought through the adaptive feedback process based on the evolutionary algorithm. The number of parameters used is determined directly by the limits set in the front panel of the main program as shown in Fig. 4.3. The phase obtained is rescaled between 0.5 pi, the upper limit 2.5 in order to let the SLM work where it has fast response

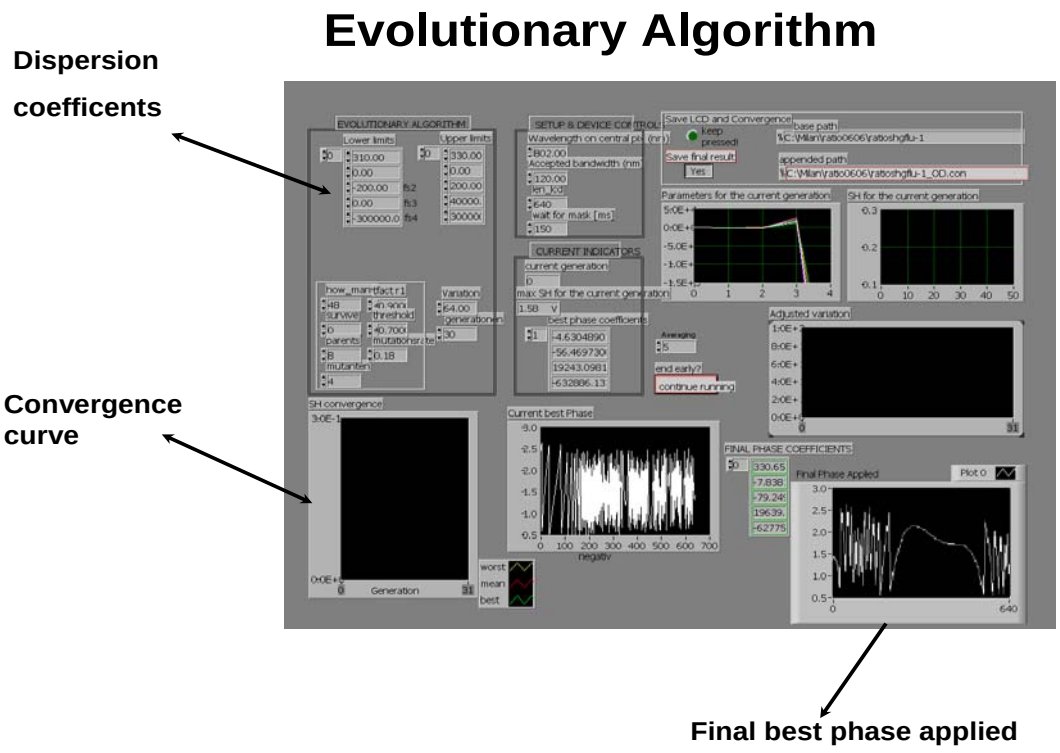

Fig. 4.3. The front panel of LabView program where evolutionary algorithm is implemented.

4.3 Experimental Setup for Coherent Control

Experimental setup for implementing coherent control with evolutionary algorithm is shown in Fig 4.4. The Feedback signal from experimental setup is given to the evolutionary algorithm and the algorithm will decide what voltage it needs to give to liquid crystal modulator so that the signal is maximized. The iteration is repeated till the optimal signal is obtained.

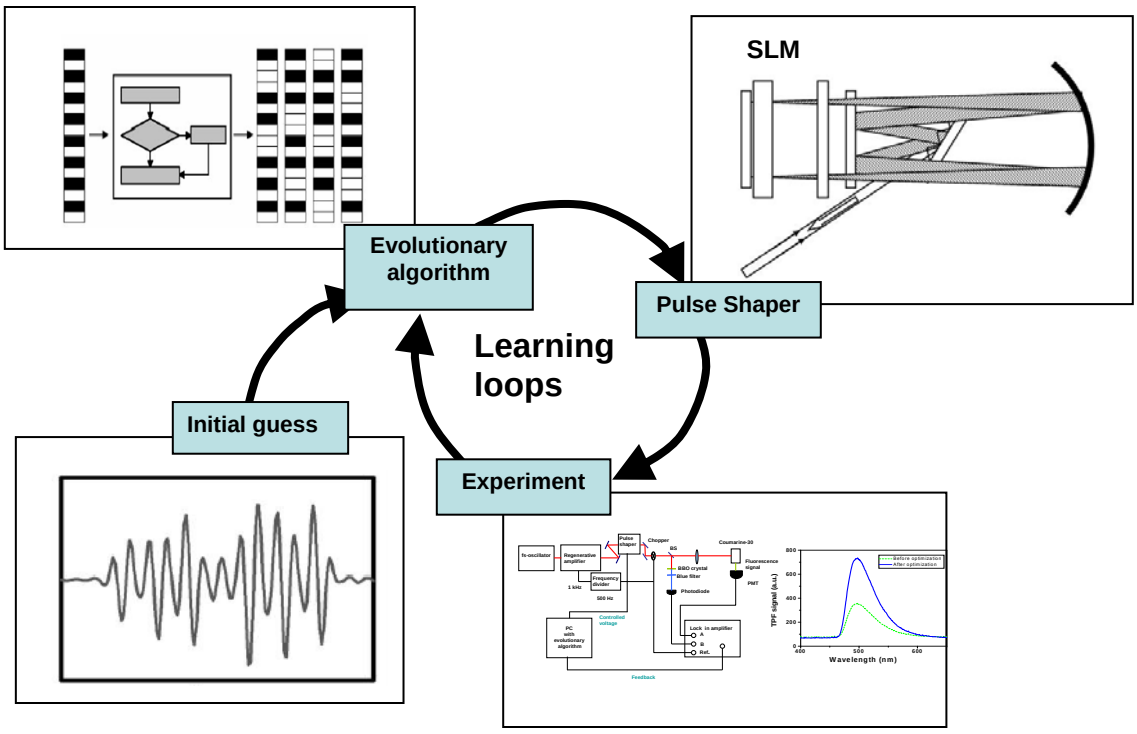

Fig. 4.4 Schematics of coherent control experiment with evolutionary algorithm. A shaped femtosecond pulse excites the sample. A photo-detector detects the effect of particular pulse on the sample. The signal is feedback to the optimization algorithm which proposes new pulse and so forth. An initial guess helps to achieve the convergence.

4.4 Performance of EA in a Feedback Control Setup with Pulse Shaper

Like in others research works [60, 61], in our feedback-controlled pulse shaping, the LC voltages are the optimization variables. This means that the number of the independent variables is fixed to the number of pixels of the liquid crystal modulators, in our case it is 640. We used a mapping between voltages and phases.

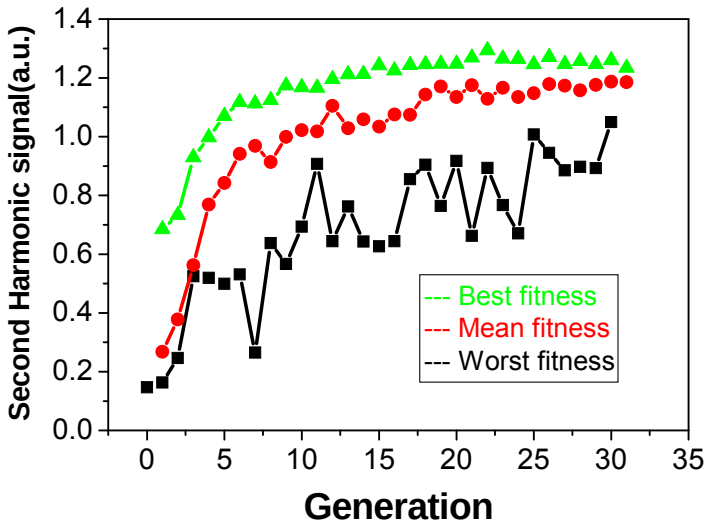

Fig. 4.5. Convergence curve for the optimization of second harmonic generation signal. The best, average and worst values are recorded for each generation.

To test our algorithm we try to optimize the second harmonic generation signal. BBO crystal was used to produce the second harmonic generation. Since it has been proved theoretically that maximum SHG signal is produce when pulse becomes shorter (transform limited). So we use GRENOUILLE to measure the pulse duration. The optimization was run repeatedly for different set of parameters. In each optimization run the best, the worst and the mean SHG values were stored for each pass of the loop. For each new generation SHG signal is increased until the required no of generation and the optimized value of SHG signal is reached. Fig 4.5 shows the convergence curve for the optimization SHG signal. After the optimization we have successfully optimized the SHG.

CHAPTER V

OPTIMIZATION OF THE EXCIATION OF SECOND HARMONIC GENERATION AND TWO-PHOTON FLUORESCENCE

Different physical processes were optimized using adaptive pulse shaping techniques. These include optimization of second harmonic generation, two photon fluorescence and ratios of two different physical processes e.g. ratio between two-photon fluorescence and second harmonic generation, two-photon fluorescence and laser intensity. This chapter describes details and result of such optimization.

5.1 Experiment

The experimental set-up is shown in Fig. 5.1. The femtosecond laser pulse formed by the oscillator and a regenerative amplifier was sent to a liquid crystal pulse shaper, which controlled the phases of the spectral components.

Instead of the traditional pulse shaper scheme with symmetric beam paths before and after the gratings and the modulator, we employed a scheme in folded geometry with an end mirror immediately after the spatial light modulator (SLM) as shown in Fig. 5.1 This set-up is intrinsically highly symmetric and can be readily aligned.

A 1800 grooves/mm grating and a cylindrical lens with a focal length of 100 mm were used for spectrally dispersing (input) and re-collimating (output) of the laser pulses. A laser pulse with a spatially dispersed spectrum passed the liquid crystal (LC)

matrix with 640 pixels in the spatial light modulator (SLM-640, JenOptik). The control of the laser pulse shape was achieved by applying a specific voltage to each pixel of the LC matrix and, in this way changing the phases of the spectral components. After reflection on the end mirror, the pulse was re-assembled by propagating back, and its output direction was slightly shifted relative to the input pulse. Since only the phases of spectral components were modulated in this study, the spectral amplitude and the total pulse energy were unchanged during the optimization process [61-63].

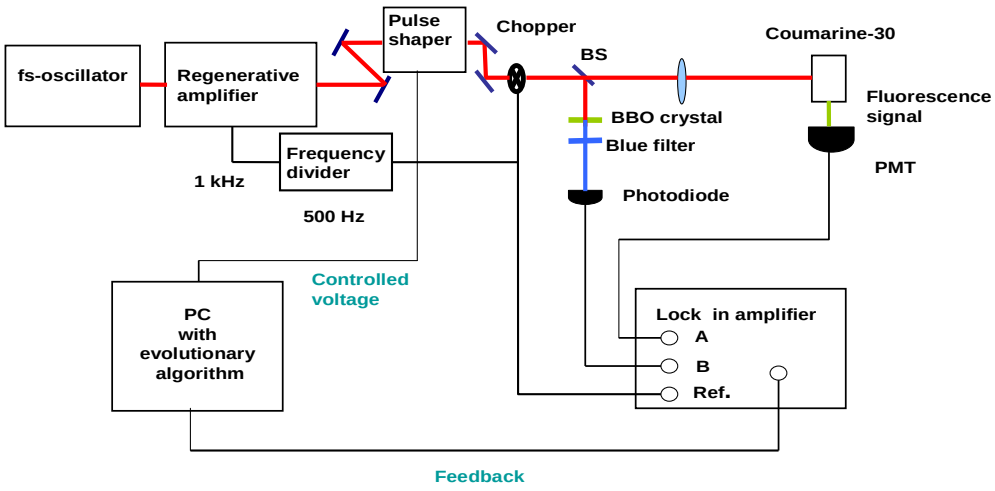

Fig. 5.1. Schematic diagram of the experimental setup.

The output pulse was split by a beam splitter. One sub-beam was focused on a cuvette of 1 cm thickness containing a 1mM solution of Coumarin-30, and the emitted two-photon fluorescence signal was filtered optically and detected by a photo-multiplier

tube (PMT). The other sub-beam was focused on a BBO crystal to produce the second harmonic radiation, which was filtered and detected by a photo-diode. A mechanical chopper with 500 Hz modulation frequency was synchronized with every other pulse of the laser (the laser pulse repetition rate of 1 kHz) so that the pulses were alternatively transmitted and blocked. The signal was detected with a lock-in amplifier referenced to the chopper, thus allowing reducing a background noise and implementing narrow band detection. Fig. 5.2 shows the chemical structure as well as the absorption and emission spectra of Coumarin-30 molecule [64, 65].

(a) (b)

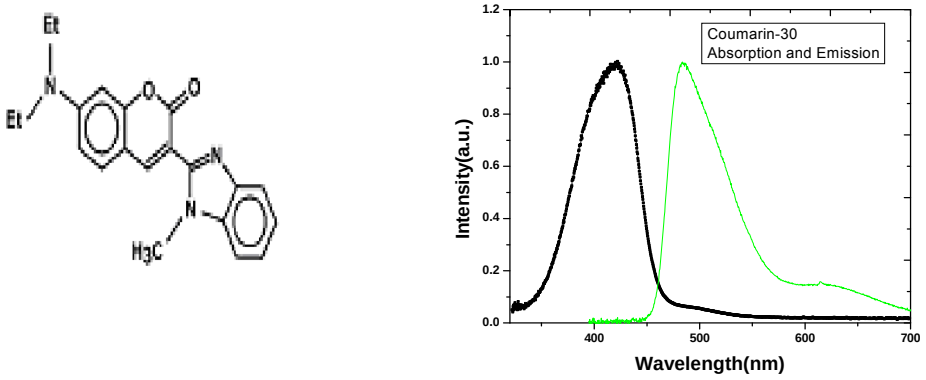

Fig. 5.2. Properties of Coumarin-30: (a) chemical structure and (b) normalized absorption and emission spectra shown by the dashed (black) and solid (green) lines respectively.

The key role in the feedback-control experiment is played by an evolutionary algorithm [60]. In this algorithm, one generation uses 48 individuals

(vectors of voltages on the LC matrix) and the fitness value is measured for every individual. A new generation is built from the previous by combining parents (the fittest individuals), producing mutations (changes of the vector elements by some random value) and crossover (recombination of elements of two vectors) to provide optimal convergence. By successive repetition of this scheme, individuals corresponding to the highest fitness values are selected, and they produce better offspring's for subsequent generations, until the optimum value is reached. Typically, convergence was achieved after 15-20 generations. It strongly depended on the laser output fluctuations which were minimized for the better performance.

5.2. Results

In different optimization runs we maximized the Second Harmonic Generation (SHG), Two-Photon Fluorescence (TPF), the ratio between TPF and SHG (TPF/SHG), the ratio between TPF and the laser power and also [$(TPF)^2$/ SHG]. In addition, we varied the chirp in small steps to clarify its influence on the fluorescence output and also performed the correlation analysis between the TPF and SHG signals.

5.2.1 Optimization of the SHG

In the optimization of the SHG signal, starting from the initial pulse of duration τ = 45 fs, the optimization resulted in a nearly transform limited pulse with a

duration of τ = 33 fs, producing a significant increase in the SHG signal. Fig. 5.3 depicts the spectrally and time resolved images of the pulses before and after the optimization obtained with a GRENOUILLE, a device based on the frequency resolved optical gating technique with second harmonic generation [29].

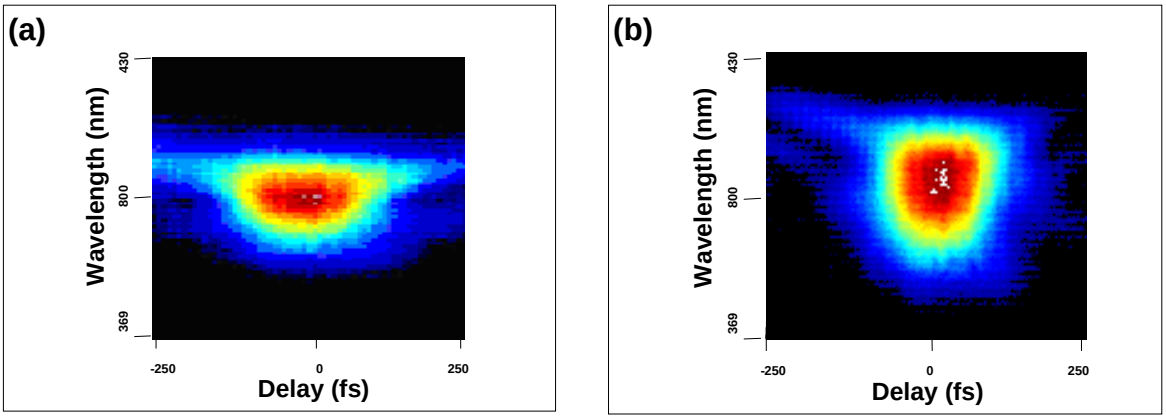

Fig. 5.3. Images of the pulse from the GRENOUILLE (a) before the optimization of the SHG signal, $\tau = 45$ fs and (b) after the optimization, $\tau = 33$ fs.

5.2.2 Optimization of TPF

After successful optimization of second harmonic generation, a real physical problem, two-photon fluorescence (TPF) was chosen for optimization. In the optimization of the TPF the signal increased by two-fold. The convergence curve

obtained from algorithm is shown in Fig 5.4. This shows the evolution of the fitness parameter for optimizing the TPF signal.

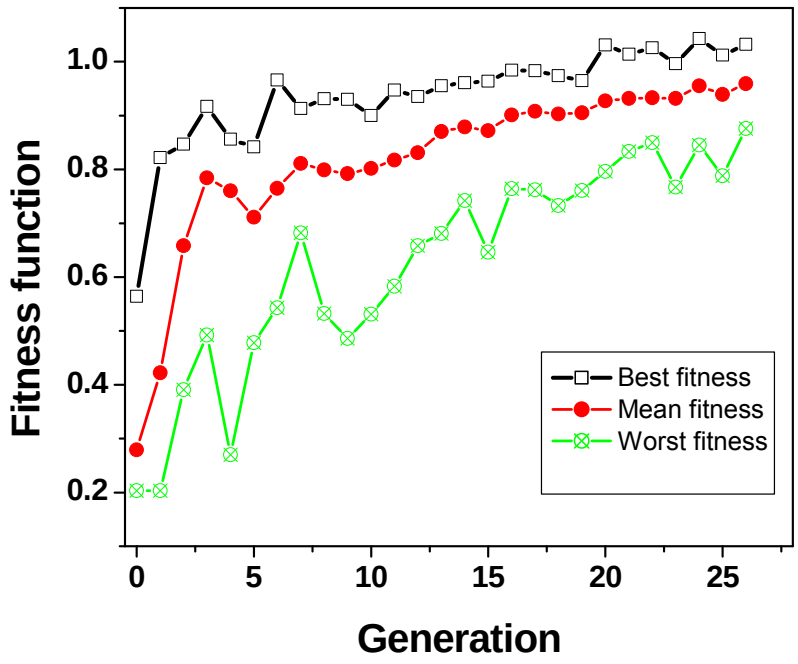

Fig. 5.4 (Color online). Convergence curves for optimization of the TPF signal.

Similarly, Fig. 5.5 shows the best set of spectral phases applied by the algorithm to obtain the optimized signal. The phase obtained (expressed in pi-units) is rescaled in order to let the SLM work in the region where it has a fast response. The lower limit for the phase is 0.5 pi, and the upper limit 2.5 pi.

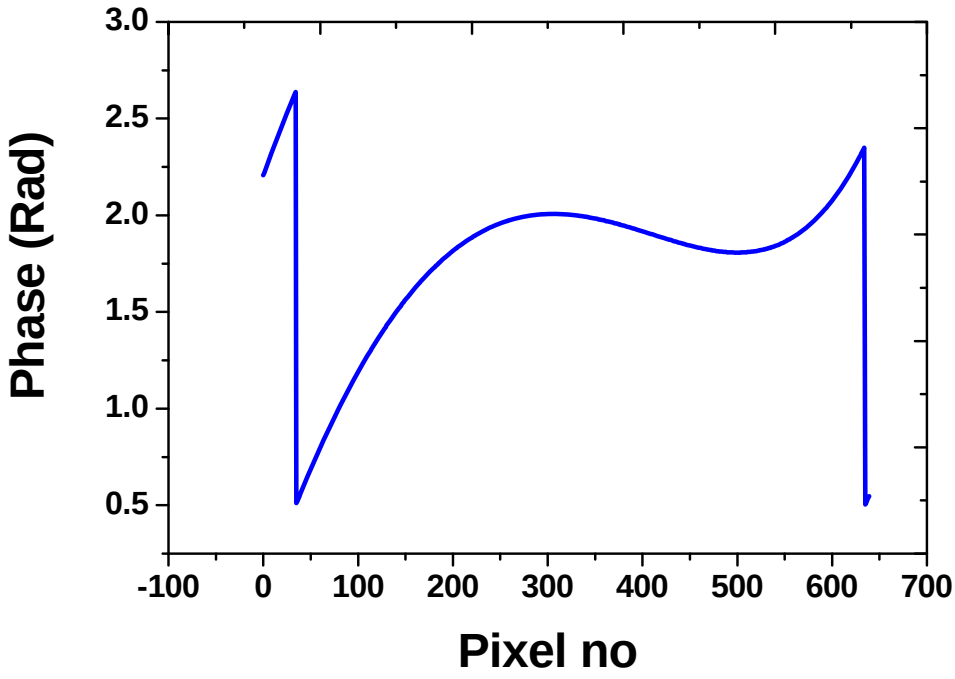

Fig. 5.5. Final best phase applied to SLM (obtained from the algorithm).

Results obtained using Ocean Optics spectrometer is shown in Fig. 5.6. This signal was. The spectrum used for optimization extended from 480 nm to 530 nm at FWHM of the fluorescence signal.

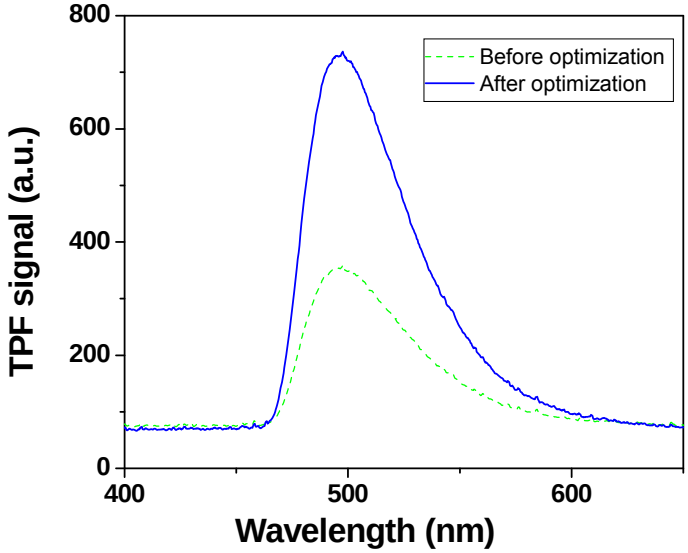

Fig. 5.6. The TPF emission spectra of Coumarin-30: before optimization (dashed line) and after optimization (solid line) obtained from Ocean Optics spectrometer.

During optimization all four dispersion parameters of Equation (2.11) are determined. The magnitude of fluorescence increases quickly in the first few generations and nearly saturates after 10-12 generations. The normalized second, third and fourth order phase dispersion coefficients (φ_2, φ_3 and φ_4) are plotted versus generation number in Fig. 5.7. As this figure shows, all coefficients converge rather quickly. For this particular measurement, the absolute values for the optimized coefficients are φ_2 = 168 fs^2, φ_3 = 12345 fs^3, and φ_4 = 261257 fs^4.

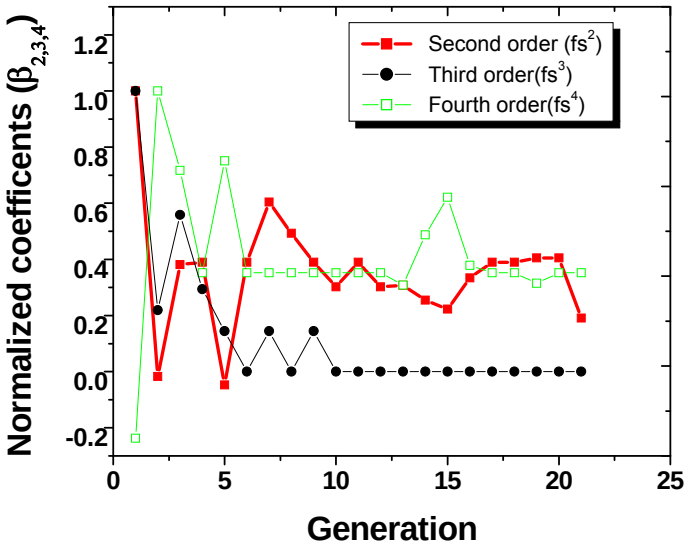

Fig. 5.7. Convergence of the second, third and fourth order dispersion coefficients for the TPF optimization.

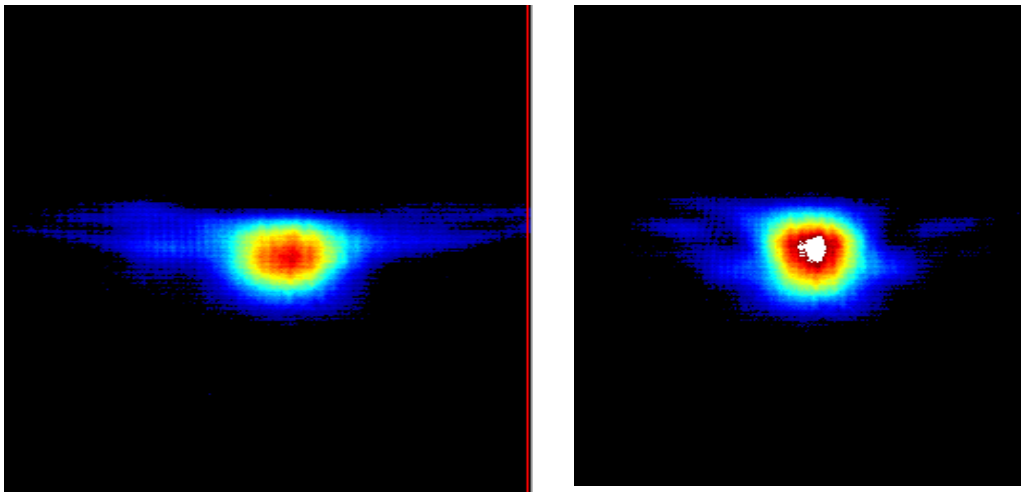

Initial Pulse 42 fs

Final Pulse 35 fs

Fig. 5.8. Images of the pulse from the GRENOUILLE (a) before the optimization of the TPFsignal, $\tau = 42$ fs and (b) after the optimization, $\tau = 35$ fs.

5.2.3 Optimization of the Efficiency

The efficiency is defined as the ratio of the two-photon fluorescence (TPF) to the laser power. It was optimized experimentally as shown in Fig. 5.9 and during this process the fluorescence signal increased, while the reference signal (laser power) stayed nearly the same, experiencing only slight fluctuations.

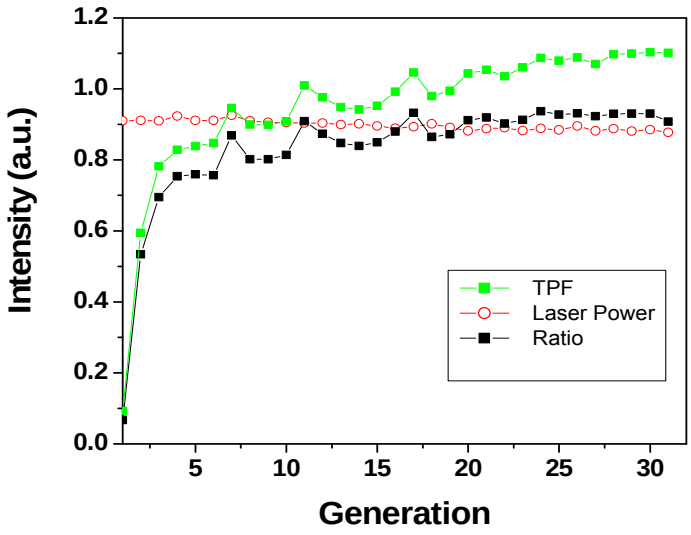

Fig. 5. 9. TPF, laser power and their ratio during efficiency optimization.

5.2.4 Optimization of the [TPF / SHG] Ratio

We performed an optimization with the goal to achieve the maximum of the ratio of the TPF to the SHG. The idea behind this optimization goal is to cancel the dominating effect of the nonlinear excitation because of its presence in both numerator

and denominator of the ratio. The possibility to control the ratio [TPF/SHG] would indicate that the two processes can be distinguished by the adaptive pulse shaping [63].

During this optimization, the signals of both the ratio and the fluorescence were increased, while the SHG signal stayed nearly the same, only slightly decreasing as shown in Fig. 5.10. During this process, the pulse duration changed from 45 fs (initial) to 34 fs (final).

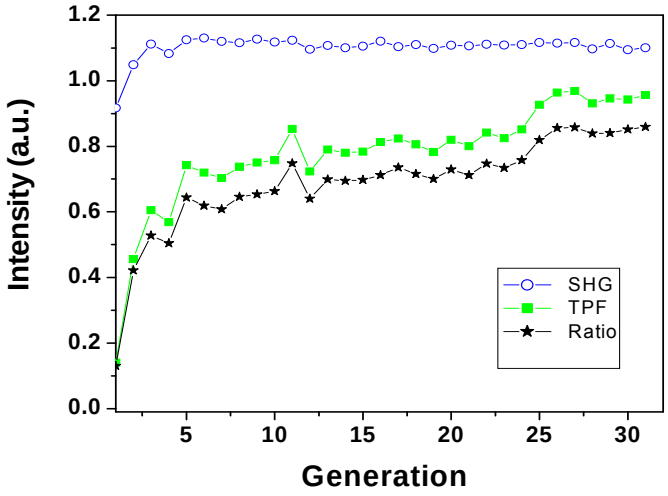

Fig 5.10. Evolution of the TPF, SHG and their ratio during the [TPF/SHG] optimization.

5.2.5 Optimization of the Ratio [$(TPF)^2$/ SHG]

When starting optimization with a pulse that is far from the optimal, both processes of optimization for TPF and SHG follow similar trend of pulse shortening. Under conditions when the noise is high or the signal channels for TPF or SHG are not

ideally linear the optimization of the ratio [(TPF)/ SHG] may still take place but lead to a false optimization solution.

To avoid this problem we performed an optimization with a new goal, namely, the ratio of the square of the fluorescence to the second harmonic signal [$(TPF)^2$/ SHG]. This ratio was optimized successfully, and the process was also accompanied by optimization of the two-photon fluorescence signal as shown in Fig. 5.11, allowing at the same time to discriminate optimal pulses for the TPF and SHG. During this optimization, the signals of both the ratio and the fluorescence were increased while the SHG signal was decreased.

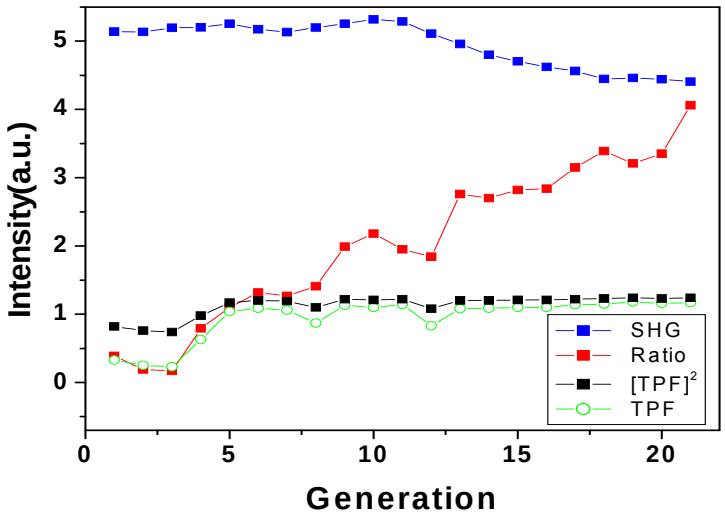

Fig. 5.11. TPF, SHG and their ratio {$(TPF)^2$/ SHG} during ratio optimization.

5.2.6 Fluorescence Optimization via Pre-determined Variation of the Pulse Chirp

In the next study, we varied the chirp to determine its optimal value for the two-photon

fluorescence. We used three different methods to determine the sign of the optimal chirp. In the first approach, we introduced the chirp by using the LC modulator. Initially, the transform -limited pulse was obtained by the optimization of the SHG process, and then the second order dispersion coefficients φ'' was changed in small steps with the calibrated LC modulator. The sketch is shown in Fig. 5.12.

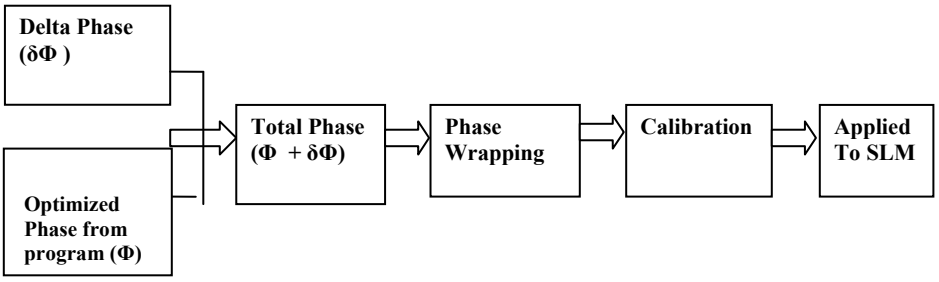

Fig. 5.12. A scheme for introducing chirp with an SLM.

In the second approach to qualitatively check results with the LC modulator, we used SF11 glass of different thicknesses to stepwise vary the chirp. Initially the pulse was optimized with a plate of glass of certain thickness (d = 4mm or d = 6 mm) inserted in the optical path. Then the glass plate was replaced by a thicker plate (positive chirp, mostly second order dispersion was added) or by a thinner plate. This second method was used only as a control measurement. Since the step size of the dispersion change is determined by the variation of the thickness, this second method is less flexible;

The third approach was using Dazzler, which was rather user friendly in the sense that the dispersion coefficients can be set directly on the front panel of the dazzler

software window. The detailed operation of Dazzler was described earlier. As an example a result obtained on DCM dye after varying linear chirp is shown in Fig. 5.13. Second harmonic signal, which is optimized by a transform limited pulse, is used as a reference signal.

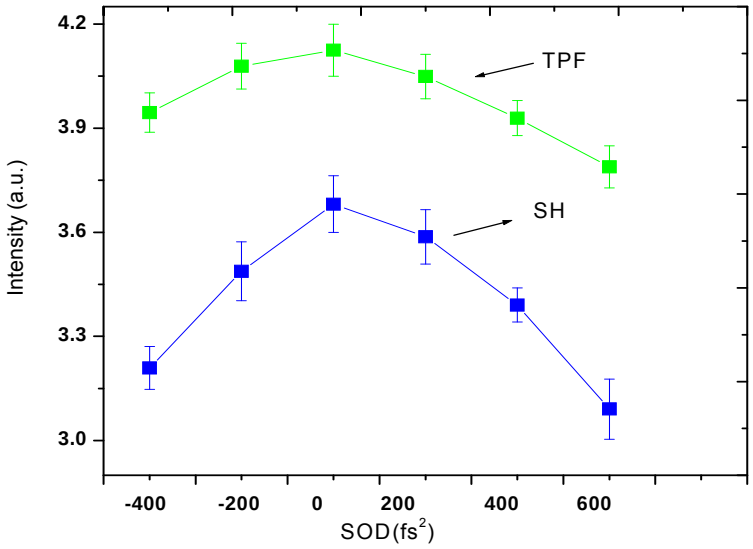

Fig. 5.13. Optimization of TPF of DCM and SH signal (produced in BBO crystal) by varying linear chirp through Dazzler.

It should be noted that we have successfully optimized two-photon fluorescence of other organic dyes, e.g. methanol solution of DCM dye. Similarly experiment is done with melanin and other biomarkers. Another important aspect of the experiment with melanin is that it has intermediate state which has resonant two photon transition, but it was also optimized by transform limited pulse as shown in Fig. 5.14.

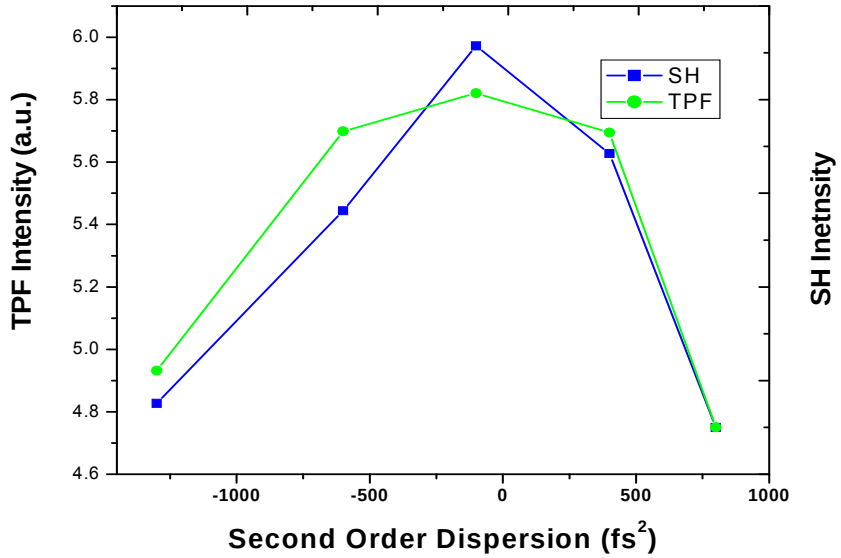

Fig. 5.14. Optimization of TPF of melanin dye and SH signal (produced in BBO crystal) by varying linear chirp through Dazzler.

5.2.7 Selective Excitation

It has been recently demonstrated that phase-modulated femtosecond pulses can selectively excite one type of probe molecule only, leaving the others in their ground state. Selectivity in multi-photon excitation can be achieved by using Dazzler (acousto-optical pulse shaper) which allows fast switching between two appropriate pulse shapes.

Having a pulse shaper for multi-photon microscopy provides the flexibility of selective probe excitation or maximum signal enhancement by controlled modulation of the spectral phase of the femtosecond pulses. Even for fluorescent labels with very similar absorption spectra, pulse shaping has been shown capable of selective excitation

[12, 13]. Thus pulse shaping provides an additional dimension towards improving the selectivity and extending the multiplex capabilities fluorescence microscopy. In this way our future work on selective excitation of different biomarkers is of great importance for two-photon microscopy and for cell imaging [66-69].

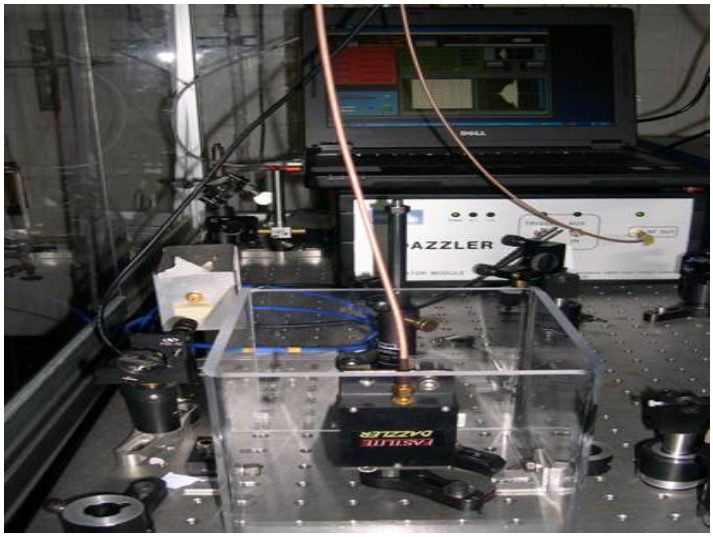

Fig 5.15. Dazzler setup.

Fig 5.15 shows the typical dazzler (programmable acoustic filter) setup for selective excitation measurement. To check the dazzler performance we have varied the linear chirps and measured the pulse duration with GRENOUILLE. Result obtained is shown in Fig. 5.16.

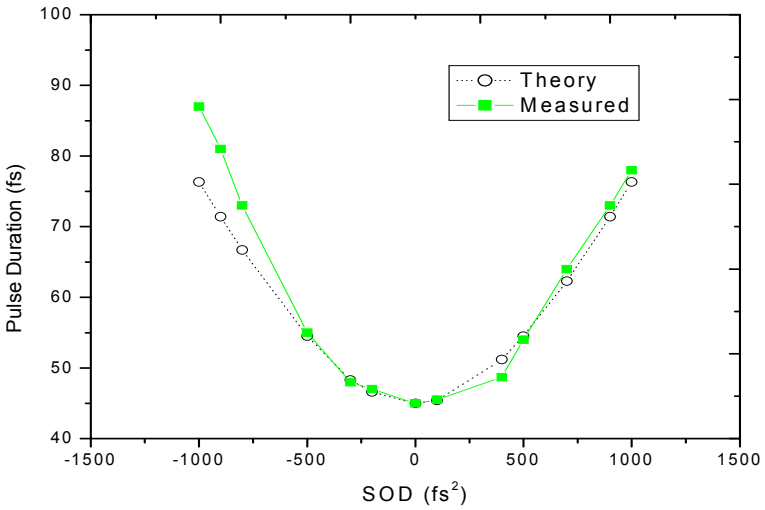

Fig. 5.16. Relationship between pulse duration and the linear chirp.

Now, two-photon power spectra $T(\omega)$ can be written as [66]

$$T(\omega) = \left| \int_0^\infty E(\tfrac{\omega}{2} + \Omega) E(\tfrac{\omega}{2} - \Omega) d\Omega \right|^2 \tag{5.1}$$

where $E(\omega)$ is the electric field and Ω is an iterative variable that ensures integration over all frequency combination. We have calculated how two-photon efficiency depends on the pulse duration and linear chirp [70]. The calculated results is shown in Fig 5.17.

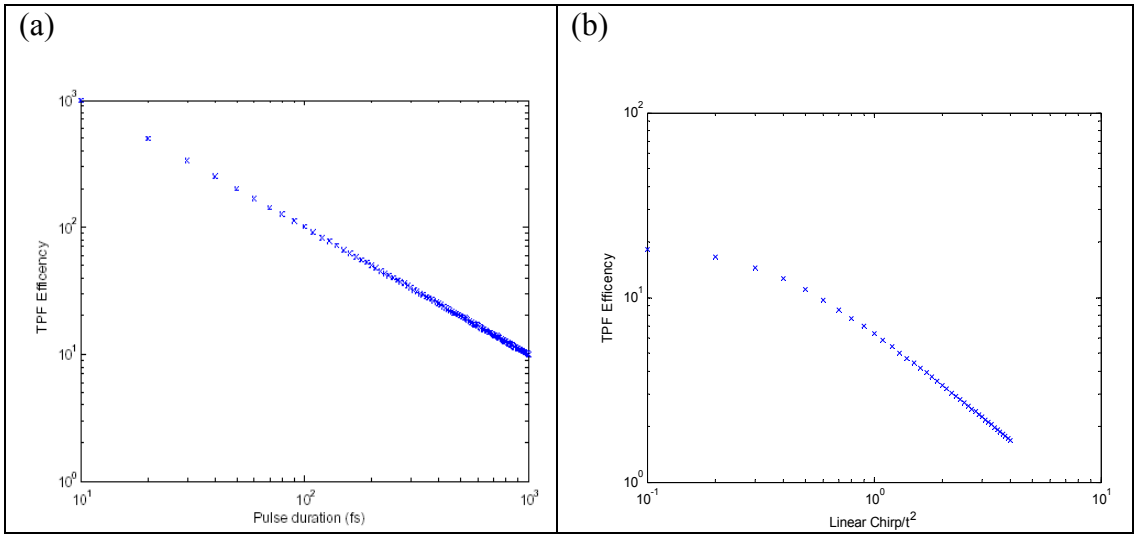

Fig. 5.17. Log-log plot of two-photon fluorescence with (a) pulse duration (b) linear chirp.

We have calculated the two photon power spectra for different combination of the chirps. These calculations suggest that the excitation energy and bandwidth of two-photon power spectra may be manipulated for selective excitation of fluorophores by controlling its spectral phase. Therefore, by using broadband laser (Femtolaser FWHM 160 nm, 7 fs) and a Dazzler we can optimize individual fluorophore from mixtures of biomarkers or fluorescent proteins. In near future, this technique may enable the characterization of molecular (protein-protein) interaction using, for example, FRET [66].

5.3 Measurements of Correlations Between TPF and SHG Signals

We have also investigated the correlation between two-photon fluorescence and second harmonic generation. The normalized correlation function $k_{norm}(\tau)$ is defined as [70]

$$k_{norm}(\tau) = \frac{<\partial I_1(t)\partial I_2(t+\tau)>}{\sqrt{[<\partial I_1^2(t)><\partial I_2^2(t)>]}} \tag{5.2}$$

where $\partial I_1(t) = I_1(t) - < I_1 >$ and $\partial I_2(t+\tau) = I_2(t+\tau) - < I_2 >$ are the variations of the second harmonic and fluorescence signals and < > means averaging, <I> = $t^{-1}\int_0^t Idt$.

In the process shown in Fig. 5.18(a) the SHG signal was optimized, while both the TPF and SHG outputs were measured. The data from Fig. 5.18(a) is divided into two portions: one is the initial stage with the data points in the range (300-900) and the other one (data points 900-1900) is the final stage of the optimization process. We used the second portion for producing the correlation function in Fig. 5.18(b). The correlation function was calculated using MATLAB. During the optimization the pulse shapes were varied resulting in variation of the TPF and SHG signals, which is clearly seen in Fig. 5.18 (a). When the optimization reaches a plateau, these variations correspond to relatively small deviation of the pulse from the optimal one. At these conditions the difference between TPF and SHG in the correlation function becomes

more noticeable. The middle peak (the delay $\tau = 0$) confirms that the two phenomena are highly correlated. However, the maximum value of the correlation function is less than 1 by an amount $\delta = 0.23$, as shown in Fig. 5.18(b). For the portion of the data corresponding to the initial stage of the optimization process (data points 300-900), the deviation $\delta = 0.08$ and is less than for the portion of the data corresponding to the final stage of the optimization. Thus, the maximum of the normalized correlation function has the trend to decrease during the optimization.

To assess the influence of noise on the correlation function we split the beam of the second harmonic into two sub-beams that were directed to the two measuring channels. With the same set up, we obtained the higher values of correlation with $\delta = 0.06$ as shown in Fig. 5.18(c). The noise level of the TPF signal was similar to the noise level of SHG signal. The small reductions of the correlation function for measurements of the same signal (SHG or TPF) in both detection channels compared to the reduction in correlation of the TPF and SHG signals demonstrate that the influence of noise is small.

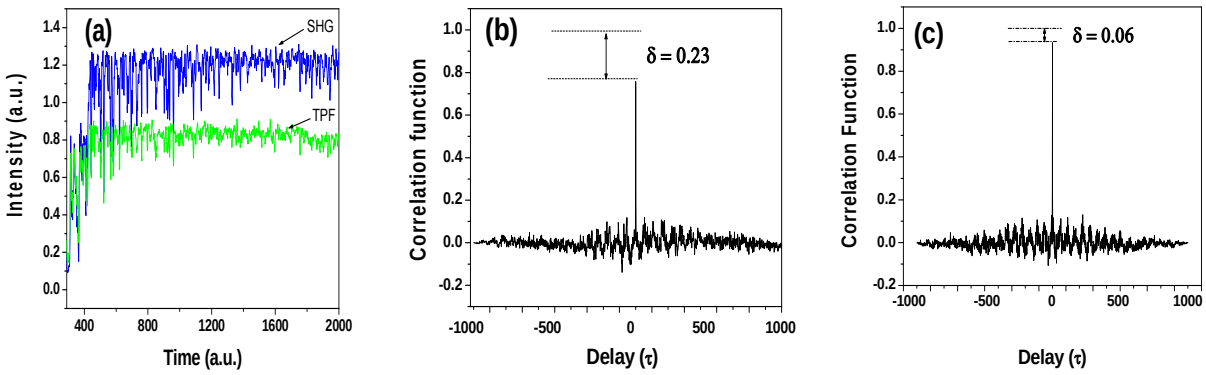

Fig. 5.18. Correlation analysis of the signals: (a) TPF and SHG signals for all individuals (sets of voltages on the LC matrix during the optimization), while SHG is optimized; (b) correlations between TPF and SHG (the deviation of maximum of the correlation function from 1, namely, $\delta = 0.23$ is due to both the different nature of the two processes and the noise); (c) correlation function of the SHG signals measured by two detection channels (in this case the deviation of the maximum from 1 due to noise is $\delta = 0.06$, and it is smaller than in Fig.5.18 (b).

The larger reduction of the correlation between TPF and SHG signals confirms that these two processes are maximized by different pulses. The smaller peaks of the correlation function noticeable in Fig. 5.18 (b, c) correspond to a temporal shift τ required by optimization process for one generation. Since each generation contains also individuals that are relatively far from the optimal one, the correlation of the TPF and SHG responses experience spikes for a delay corresponding to one generation.

5.4 Discussion

By using the feedback control pulse shaping technique, we were able to increase the two-photon fluorescence signals significantly. The optimization of two-photon fluorescence was also investigated previously in other molecular systems [2, 3]. In dye molecules LD690 and LDS750 [7], a positively chirped pulse increased the total amount of the single-photon fluorescence. But in our experiment, we found that a pulse with only relatively small linear chirp (almost transform limited pulse) was more favorable for the enhancement of two-photon fluorescence of the Coumarin-30 dye. Our experiments with different optimization goals demonstrated the possibility to adapt the pulse shape to electronic and vibrational properties of the molecule in such a way that a given ratio of the signals is optimized. By optimizing the ratio (TPF / SHG) we could exclude the intrinsic nonlinear intensity dependence for these two photon processes. Correlation analysis shows that the TPF and SHG signals are highly correlated, because both processes are optimized by short pulses. However, the different nature of these two processes results in slightly different shapes of the optimal pulses and leads to a decrease of correlation with the progress of optimization process. Similarly selective excitation using broadband femtosecond laser pulses has great importance in biomedical imaging.

5.5 Conclusion

In this research work, we designed and implemented a pulse shaper with a folded 4f configuration. We have demonstrated that the two-photon fluorescence can be

increased significantly compared to the transform-limited pulse using a pulse shaping technique with an evolutionary algorithm. With different optimization goals i.e. (TPF/SHG), $[(TPF)^2/ SHG]$, it was possible to remove the trivial intensity dependence. The successful optimization of these ratios shows the effectiveness of the feedback-control pulse shaping for steering the excitation of electronic and vibrational motions of a molecule to achieving the desired goal. The introduction of a new optimization function $[(TPF)^2/ SHG]$ improves the convergence of the optimization process under noisy conditions.

The performed correlation analysis shows that the two phenomena, two-photon fluorescence and second harmonic generation are highly correlated. The correlation is higher during the initial stages of the optimization and decreases, when the pulse approaches to the optimal shape, which is different for each of these processes. These experimental results are of interest for potential applications of coherent control to complex molecular systems as well as in biomedical fluorescence imaging with two-photon excitation.

CHAPTER VI

SUMMARY

Coherent quantum control has attracted interest as a mean to influence the outcome of quantum-mechanical interactions. In principle, the quantum system can be steered towards a desired target by its interaction with ultrafast laser fields. This fascinating possibility of coherent control based on shaping of femtosecond laser pulses to get the desired outcome has get significant attention since its introduction by Rabitz et al in 1992. Adaptive femtosecond coherent control has proven to be an efficient tool for optimization of different physical processes. Coherent control could revolutionizes biomedical field and has been already been used in the optimization of CARS and light harvesting molecules.

In this research work, coherent control technique has been used for the optimization of two-photon fluorescence (TPF) and its applications in selective excitation for biomedical imaging. Two different approaches for pulse shaping techniques have been realized. First one is using liquid crystal modulator (LCD) and another one I using acoustic optical programmable filter (DAZZLER). Among these liquid crystal arrays furnish certain advantages, namely they have good resolution, reasonably high frame rate together with relatively high damage threshold (about 1 MW/cm^2). In this work, we have designed "folded 4f pulse shaper", a novel modification to a traditional 4f pulse shaper. Instead of the traditional scheme with symmetric beam paths before and after the gratings and the modulator, we have employed a scheme in folded geometry with an

end mirror immediately after the spatial light modulator (SLM). This setup is intrinsically highly symmetric and can be readily aligned.

By using pulse shaping techniques in combination with evolutionary algorithm, we have optimized different nonlinear processes. Initially we optimized the processes with known outcome, i.e. optimization of second harmonic generation to check the reliability of the algorithm and adaptive control system. We were able to get the short pulse (nearly transform limited) with significant increase of second harmonic signal. Then we optimized two-photon fluorescence of organic dyes and biomarkers namely Coumarin-30, DCM, Texas Red and melanin. Ratios between two different processes were also optimized. In particular, we performed an optimization with the goal to achieve the maximum of the ratio of the TPF to the SHG. The idea behind this optimization goal is to cancel the dominating effect of the nonlinear excitation because of its presence in both numerator and denominator of the ratio. The possibility to control the ratio [TPF/SHG] indicated that the two processes can be distinguished by the adaptive pulse shaping. Similarly, the ratio of the square of the fluorescence to the second harmonic signal [$(TPF)^2$/ SHG] and the ratio between TPF and laser intensity have been successfully optimized. The successful optimization of these ratios shows the effectiveness of the feedback-control pulse shaping for steering the excitation of electronic and vibrational motions of a molecule to achieving the desired goal. The introduction of a new optimization function [$(TPF)^2$/ SHG] improves the convergence of the optimization process under noisy conditions.

We have performed the correlation analysis of two-photon fluorescence and second harmonic generation. The performed correlation analysis shows that the two phenomena, two-photon fluorescence and second harmonic generation are highly correlated. The correlation is higher during the initial stages of the optimization and decreases, when the pulse approaches to the optimal shape, which is different for each of these processes.

The applications of coherent control to nonlinear microscopy are still at an early stage but are promising tools for providing chemically specific images. These methods will crucially depend on the efficiency of pulse shaping technologies, particularly the ability to switch rapidly between one pulse shapes to another which is a prerequisite for the simultaneous acquisition of complementary images. Selective excitation of different biomarkers by using broadband femtosecond pulse and fast switching pulse shaper got a tremendous interest. Some preliminary research work was done in this regard too.

For centuries, the optical microscope has been the premier tool for quantitative understanding of cellular and tissue structure at the submicron level. However conventional microscopy has some important limitations [71]. Over the last decade the use of nonlinear effect has improved the spatial resolution and molecular contrast. Other nonlinear effects along with the pulse shaping techniques can be used to improve the deeper tissue imaging [72]. So we have studied the details study of these effects.

By using the shaped pulses with two-photon fluorescence and z-scan techniques, we have studied different nonlinear effects, i.e. self-focusing, white light continuum generation, filamenation, intensity clamping saturation and optical breakdown. A systematic study of the power and intensity dependences of the two-photon fluorescence of methanol solutions of Coumarin-30 dye and other dyes were performed using the Z-scan technique. Filamentation process and other nonlinear physical processes were studied by performing simultaneous measurements of TPF and transmission or white light continuum generation. We have calculated the critical power for self-focusing effect, which was found to be 1.5 MW for methanol. The upper limit for the laser power range that we were using exceeded the critical power for methanol. Consequently, we observed that the self-focusing effect leads a shift of the focus towards incoming laser beam. When the self-focusing effect leads to the plasma generation (free electrons), with increasing power it first can balance the focusing and at even higher intensities defocuses the pulse that can lead to the intensity clamping. At high laser powers also the saturation effect in the TPF signal was observed. For the white light generation, threshold energy was found to be 1μJ for the lens of 125 mm focal length with beam radius 5 mm. The nonlinear competition effects were also studied by changing the linear chirp of input pulse. Similar experiments were performed with other dyes e.g. DCM & Melanin.

By employing deconvolution of the data in the imaging of the two-photon fluorescence (TPF) light distribution and also analyzing the data from the Z-scan technique we obtained intensity-resolved values for the TPF saturation threshold. This is

especially important, because usually, the data obtained for characteristics of the two-photon processes are averaged spatially and temporary. This follows from the fact that each laser pulse used in the measurements has both spatial and temporal intensity distributions that must be accurately accounted for in the measurements. Obtaining of the intensity-resolved data is important also for comparing of the theoretical results with experimental ones.

In this work, several methods to obtain two-photon characteristics in intensity-resolved manner are employed. A theoretical model was developed describing the saturation of the two-photon fluorescence during a Z-scan method. A procedure is developed to solve the inverse problem of extracting the saturation dependence of the fluorescence on the laser intensity from the observed fluorescence signal. By fitting this model to the experimental data we determined the TPF saturation threshold and the TPF probabilites of Coumarin-30 dye. This result shows for the first time that Z-scan technique which is mainly used in chemistry and biology to find two-photon absorption coefficient and nonlinear refractive index can be used to find the TPF probabilities and saturation intensity.

Similarly, a new alternative method that relies on geometrical comparison of spatial laser profile with images of two-photon fluorescence is introduced. A single image from CCD was used to determine the saturation status and associated saturation intensity by just mapping TPF with corresponding light intensity distribution. This method gives the most reliable (true) probability for the TPF process. The saturation intensity we have found for Coumarin-30 dye was $2*10^{13}$ W/cm^2.

In the summary, these experimental results are of interest for potential applications of coherent control to complex molecular systems as well as in biomedical fluorescence imaging with two-photon excitation. These studies of different nonlinear effects allow us to understand the relation between these processes and its application in nonlinear microscopy.

REFERENCES

[1] W. S. Warren, H. Rabitz , and M. Dahleh, Science**, 259**, 1581 – 1589 (1993)

[2] I. Walmsley and H. Rabitz, Phy. Today, **8**, 43-49 (2003)

[3] T.Brixner, G, Chemphychem, **4,** 418 (2003)

[4] P. Burmer, M. Shapiro. Sci. Am. **272**, 34 (1995)

[5] I. Pastrik, E.J. Brown, Q. Zhang, M. Dantus, J. Chem. Physics, **108**, 4375 (1998).

[6] R. S. Judson, H. Rabtiz Phys. Rev. Lett. **68**, 1500 (1992)

[7] C. J. Bardeen, V. V. Yakovlev, K. R. Wilson, S. D. Carpenter, P. M Weber, W. S Warren Chem.Phys. Lett. **280**, 151 (1997) .

[8] R. Bartels, S.Backus, E. Zeek, L. Misoguti, P. Vdovin, I. Chistov, M. Murname, H. Kapteyn, Nature **406,** 164 (2000)

[9] D. Meshulach and Y. Silberberg, Nature **396,** 239 (1998)

[10] J. L. Herek, W. Wohleben, R. Cogdell, D. Zeidler, M. Motzkus, Nature **417,** 533 (2002).

[11] D. Yelin, D. Meshulach and Y. Silberberg, Opt. Lett. **23,** 1793 (1998)

[12] I. Pastrick, J. M. Dela Cruz, K. A. Walowicz, V. V. Lozovoy, M. Dantus, Opt Exp. **11**, 1695 (2002)

[13] J. P. Ogilvie, D. Debarred, M. Joffre, Opt. Exp. **14**, 759 (2006)

[14] M. Roth, L. Guyon, J. Roslund, V. Boutou, F. Courvoisier, J. P. Wolf, and H. Rabitz Phys. Rev. Lett. **102,** 253001 (2009)

[15] A. M. Weiner, Rev. Sci. Instrum. **71**, 1929 (2000)

[16] N. Dudovich, B. Dayan, Gallagher and Y. Silberberg, Phys.Rev. Lett. **86,** 1793 (2001)

[17] N. Dudovich, D.Oron, Y. Silberberg , Nature **418**, 512 (2002)

[18] M. Sheik-Bahae, A. A. Said, and E. W. van Stryland, Opt. Lett. **14**, 955–957 (1989).

[19] H. Schroeder, S. L. Chin, Opt. Communications, **11**,1695 (2002)

[20] M.A. Walker, P. Hansch and L.D. Woerkom Phy. Rev. A **57**, R703 (1998)

[21] P. Hansch and L.D. Woerkom , Opt. Lett. **21**, 1286 (1996)

[22] U. Keller, G. W 'tHooft', W. H. Knox, and J. E. Cunningham, Opt. Lett. **16**, 1024 (1991)

[23] J. C. Diels, W Rudolph, *Ultrafast Phenomena* (Academic Press, Burlington, MA, 2006)

[24] S. Jeverstov, Ph.D, Dissertation, (Texas A&M University, College Station, 2007).

[25] F. Gan, *Laser Materials* (World Scientific, Singapore, 1994)

[26] J. Rauschenberger, T. Fuji, 1 M. Hentschel, A. J. Verhoef, T. Udem, C. Gohle, T.W. Hansch, and F. Krausz, Laser Phys. Lett. **3**, 37 (2006)

[27] F. Krausz et al., IEEE J. Quantum Electron. **28**, 2097 (1992)

[28] R. Trebino, *Frequency Resolved Optical Gating* (Kulwar Academic Publishers, Boston, 2002)

[29] R. Trebino, K. W. DeLong, D. N. Fittinghoff, J. N. Sweetser, M. A. Krumbügel, and D. J. Kane, Rev. Sci. Instrum. **68,** 3277-3295 (1997).

[30] Autocorrelator, http://www.swampoptics.com/tutorials_autocorrelation.htm, Accessed 07-12-09

[31] Femtosecond pulse shaping with liquid crystal modulators, http://www.diss.fuberlin.de/diss/servlets/MCRFileNodeServlet/FUDISS_derivate Accessed 07-12-09

[32] F. Verluise, V. Laude, Z. Cheng, Ch. Spielmann, P. Tournois Opt. Lett. **25** (2000)

[33] A. E. Siegman, *Lasers*, (University Science Book , Mill Valley, CA, 1986)

[34] Dispersion, http://en.wikipedia.org/wiki/Dispersion_(optics), Accessed 07-12-09

[35] H.Lubatschowski et. al, *Femtosecond Technology for Technical and Medical Applications* (Springe-Verlag Berlin, Berlin 2005).

[36] M. P. Poudel, Opt.Letters, **34**, 337 (2009)

[37] A. Couairon, A. Mysyrowicz, Physics Reports **441**, 47 (2007)

[38] C. B. Schaffer, N. Nishimura, E. N. Glezer, A. Kim and E Mazur, Opt. Exp. **10**, 196 (2002).

[39] R. W. Boyd, *Nonlinear Optics*, (Academic Press, Burlington, MA, 2003).

[40] Y.R Shen, *Nonlinear Optics*, (Academic Press, Burlington, MA, 2005).

[41] S.L. Chin, S. Petit, F.Borne, K.Miyazaki, Jpn. J. Appl. Phys. **38** (1999)

[42] H. Schroeder, S.L. Chin, Optics Comm. **234**, 399 (2004)

[43] H. Schroeder, S.A. Hosseini, Q. Luo, S.L. Chin, Optics Comm. **266**, 306 (2006)

[44] Chris Schaffer, Ph.D. dissertation, (Harvard University, Cambridge, MA (2001)

[45] J. H. Marburger, Prog. Quantum Electron. **4**, 35 (1975).

[46] M. D. Feit and J. A. Fleck, J. Opt. Soc. Am. B **5**, 633 (1988).

[47] G. Baruch, G. Fibich, and S. Tsynkov, Opt. Express **16**, 13323 (2008).

[48] E. T. J. Nibbering, M. A. Franco, B. S. Prade, G. Grillon, C. Le Blanc and A. Mysyrowicz, Opt. Comm. **119**, 479 (1995)

[49] Rothenberg J E Opt. Lett. **57,** 2268 (1986)

[51] Yang G Y and Shen Y R, Opt Lett. **9,** 510 (1984)

[52] M. Goeppert-Mayer, Ann Phys. **9**, 273 (1931)

[53] D. Yelin, D. Meshulach and Y. Silberberg, Opt. Lett. **23,** 1793 (1998)

[54] I. Otake, S. S. Kano, A. Wada, J. Chem. Phys. **124,** 14501 (2006)

[55] D. Meshulach and Y. Silberberg, Nature **396,** 239 (1998)

[56] J.Wang, M. Sheik-Bahae, A. A. Said, D. J. Hagan, and E.W. Van Stryland, J. Opt. Soc. Am. B. **11**, 1009 (1994)

[57] Kaplan, W. *Advanced Calculus (*Addison-Wesley, Reading, MA 1992)

[58] O. Nalamura, Microscopy Research and Tech. **47**, 165 (1999)

[59] M. Kauert, P.C. Stoller, and M. Frenz and J.Ricka, J. Opt. Exp. **14**, 8434 (2006).

[60] Zeidler, S Frey, K.L. Kompa, M. Motzkus, Phys.Rev. A. **64,** 023420 (2000)

[61] T. Brixner, A.Oehrlein, M.Strehle, G.Gerber, Appl. Phys. B **70,** S119 (2000)

[62] D. Meshulach and Y. Silberberg, Nature **396**, 239 (1998) .

[63] T. Brixner, N.H. Damrauer, B. Kiefer and G. Gerber, J. Chem. Phys. **118** 3692 (2003).

[64] B. Kovac, I. Novak, Spect. Acta, A **58**, 1483 (2002)

[65] S Jerebtsov, A. Kolomenski, M. Poudel, F Zhu, H. Schuessler Jour. of Mod. Opt. **53** 10 (2006)

[66] A. T. Yeh, H. Gibbs, J. J. Hu, A. M. Larson. Tissue Engineering Part B, **14**, (2008)

[67] Milan Poudel, http://absimage.aps.org/image/MWS_DAMOP09-2009-000733.pdf, Accessed 07-12-09

[68] C. Xu, J. Guild, W Denk, W. Webb, Opt Lett. **20**, 2372 (1995)

[69] C. J. Bardeen, V. V. Yakovlev, J. A Squier, K.R. Wilson, S. D. Carpenter and P. M. Weber Jour. Biomed. Opt. **4**, 362 (1999)

[70] M.O. Scully and M. S. Zubairy, *Quantum Optics*, (Cambridge Press, Cambridge 1997)

[71] S.G. Megason and S. E. Fraser, Cell **130** (2007)

[72] W. S.Warren, M. C. Fischer and T. Ye, Laser Focus World **45**, 6 (2009)

VITA

Name: Milan Prasad Poudel

Address: Department of Physics
Texas A& M University
College Station, TX 77843-4242

Email Address: mpoudel@physics.tamu.edu

Education:

B.S. Physics, Tribhuvan University, 1998

Diplom Physics, University of Hannover, 2002

M.S. Physics, University of Hannover, 2002